NASA CONTRACTOR REPORT

NASA CR-1303

CALCULATION OF COMPRESSIBLE TURBULENT BOUNDARY LAYERS WITH PRESSURE GRADIENTS AND HEAT TRANSFER

by Larry L. Lynes, Jack N. Nielsen, and Gary D. Kuhn

Prepared by
NIELSEN ENGINEERING & RESEARCH, INC.
Palo Alto, Calif.
for Ames Research Center

NATIONAL AERONAUTICS AND SPACE ADMINISTRATION • WASHINGTON, D. C. • MARCH 1969

CALCULATION OF COMPRESSIBLE TURBULENT BOUNDARY LAYERS WITH PRESSURE GRADIENTS AND HEAT TRANSFER

By Larry L. Lynes, Jack N. Nielsen, and
Gary D. Kuhn

Issued by Originator as Report NEAR TR 6

Prepared under Contract No. NAS 2-4391 by
NIELSEN ENGINEERING & RESEARCH, INC.
Palo Alto, Calif.

for Ames Research Center

NATIONAL AERONAUTICS AND SPACE ADMINISTRATION

For sale by the Clearinghouse for Federal Scientific and Technical Information
Springfield, Virginia 22151 – CFSTI price $3.00

TABLE OF CONTENTS

LIST OF FIGURES

CALCULATION OF COMPRESSIBLE TURBULENT BOUNDARY LAYERS WITH PRESSURE GRADIENTS AND HEAT TRANSFER

By Larry L. Lynes, Jack N. Nielsen, and Gary D. Kuhn
Nielsen Engineering & Research, Inc.

SUMMARY

The method of integral relations has been applied to the calculation of compressible turbulent boundary-layer characteristics under the action of pressure gradients. In order to solve the problem it was necessary to specify an eddy-viscosity model. An incompressible model, developed on the basis of the law of the wall and the law of the wake, was extended to compressible flow through the use of the Baronti-Libby transformation. A computer program was developed to do the calculations for a class of two-dimensional or axisymmetric configurations from low speeds to hypersonic speeds. The program contains provisions for arbitrary streamwise pressure distributions. The problem of obtaining initial conditions for the program required special attention, and several methods for obtaining initial conditions are presented.

Comparisons were made between predictions and measurements of displacement thickness, momentum thickness, and velocity profiles for two-dimensional configurations from low speeds to hypersonic speeds. Generally, good agreement was obtained between theory and experiment at low speeds except in the region upstream of the separation point. At a separation point a mathematical singularity exists in the analysis. Some work was accomplished toward developing a slightly different formulation designed to go up to and including the separation point.

At hypersonic speeds, comparisons were made between predicted and measured boundary-layer quantities for curved plates and flat plates with and without oblique shock-wave impingement. For the curved plates decisive results were not obtained because of the limited amount of data and because of nonisentropic conditions at the edge of the boundary layer not accounted for in the computer program. For the flat plate without shock impingement the edge conditions were more isentropic than for the curved plate, and better comparison between theory and experiment was obtained. With shock impingement the predicted displacement and momentum thickness differed from the measured values from a negligible precentage to as much as 25

percent. Only fair agreement was obtained between the predicted and experimental velocity profiles after shock impingement.

The computer program has been applied to a hypersonic axisymmetric configuration composed of a hollow cylinder culminating in a compression flare. The shape of the flare was such that large pressure drops occurred across the boundary layer. The predictions are in good agreement with the measured heat-transfer rates and the measured displacement and momentum thicknesses corrected for normal pressure gradients. Comparison has been made between the experimental Mach number profiles and the predicted Mach-number profiles. When the predicted Mach-number profiles were adjusted for normal pressure gradients, the agreement was only fair. A simple method is presented for estimating the magnitude of the normal pressure gradients and of adjusting the displacement and momentum thicknesses predicted by boundary-layer theory for the gradients.

A study has been made of the detailed flow field predicted by the computer program for boundary-layer, shock-wave interaction on a flat plate with a view to developing a model of the interaction based on boundary-layer theory. The purpose of the model is to predict the pressure distribution accompanying the interaction as well as the boundary-layer development downstream of the interaction. The model is an idealized one because boundary-layer theory will not predict the details of the flow in the interaction region where the incident shock penetrates deeply into the layer. An interaction model is suggested together with a free-interaction law for use with the model.

INTRODUCTION

Calculation of turbulent boundary layers under the action of pressure gradients has been of interest for a number of years. Renewed interest in the accurate prediction of turbulent boundary-layer properties at high speeds has arisen in the design of hypersonic inlets, controls, and other external aerodynamic surfaces. In these applications the pressure gradients involved can be very strong. For instance, in the interaction between a shock wave and a boundary layer in a hypersonic inlet a pressure rise of two orders of magnitude can occur over a distance of about 10 boundary-layer thicknesses.

The usual approaches to the calculation of turbulent boundary layers with or without pressure gradients involve the use of an empirical prescription of some gross properties of the boundary layer such as skin friction or shape factor. Typical examples of such methods are contained in references 1 through 8. Recently, two new approaches to turbulent boundary layers have met with significant success in predicting the details of the flow as well as the gross properties. One approach utilizing finite-difference methods is contained in reference 9. The other approach presented in this report is based on the method of integral relations. This method, successfully applied to laminar boundary layers in references 10 through 12, is extended herein to turbulent boundary layers through the use of an eddy-viscosity model.

The work presented in this report was accomplished under a 1-year effort sponsored by Ames Research Laboratory, NASA, Contract No. NAS2-4391. The main effort has been directed toward applying the method of integral relations to two-dimensional and axisymmetric compressible turbulent boundary layers on nonadiabatic bodies. A computer program for making these calculations has been developed. In addition, a portion of the effort has been devoted to the study and development of a method for simultaneous determination of the pressure distribution and the boundary-layer characteristics during a shock-wave, turbulent, boundary-layer interaction. The following sections contain the analyses which lead to a computer program and contain a substantial number of comparisons between prediction and experiment.

An operating manual for the computer program is being issued as a separate document.

SYMBOLS

a	speed of sound
$\bar{c}, c_i$	coefficients used in specifying the velocity profiles, functions of ξ only
c_f	skin-friction coefficient, $\tau_w/(1/2)\rho_e u_e^2$
c_p	specific heat of air at constant pressure
$f_i(\bar{U})$	family of smoothing functions, $(1 - \bar{U})\bar{U}^{(i-1)}$
f_i', f_i''	first and second derivatives of f_i with respect to $\bar{U}$, respectively

$\overline{F}_i$ family of definite integrals defined by equation (87)

F_j family of definite integrals defined by equation (77)

g acceleration of gravity, 32.2 ft/sec^2

$g_i(\overline{c})$ family of definite integrals given by equation (55)

g_i' derivative of g_i with respect to $\overline{c}$

G_i family of definite integrals defined by equation (57)

H total enthalpy of gas, $\int_0^{T_t} c_p \, dT$

J mechanical equivalent of heat, 778 ft-lbs/Btu

k thermal conductivity of air

k_s streamline curvature defined by equation (131)

ℓ reference length in two-dimensional plane

L reference length in axisymmetric plane

m $\left(\frac{\gamma - 1}{2}\right) \frac{u^2}{a^2}$

M local Mach number

n a coordinate normal to a streamline; also an index

p local static pressure

p_{se} local static pressure calculated by shock-expansion theory

p_t local stagnation pressure

p_{t_1} local stagnation pressure for tests of reference 28

p_{t_2} local stagnation pressure behind normal shock

P_i family of definite integrals defined by equation (51)

q_w heat-transfer rate at wall

r local body radius in the axisymmetric plane

RH_i right-hand side of the nonhomogeneous equations for the no-root case

RS_i right-hand side of the nonhomogeneous equations for the root case

R_{ℓ_o} initial Reynolds number, $u_{e_o} \ell / \nu_{e_o}$

R_z Reynolds number based on any arbitrary length z and local edge conditions, $u_e z/\nu_e$

s distance along surface of axisymmetric flare measured from flare-cylinder juncture

S total temperature parameter, $S = (T_t/T_{t_e}) - 1$

St Stanton number defined by equation (128)

S_w value of S at the wall, $S_w = (T_w/T_{t_e}) - 1$

T local absolute temperature

T_t local stagnation temperature

u axial velocity in x,y plane

$u_o(y)$ initial velocity profile at x_o

u_τ friction velocity, $\sqrt{\tau_w/\rho_w}$

U axial velocity in X,Y plane, ua_{e_o}/a_e

$\overline{U}$ U/U_e

v normal velocity in x,y plane

v_t velocity tangent to a streamline

V normal velocity in X,Y plane

$\overline{V}$ normal velocity in ξ,η plane, $\frac{V}{U_e}\sqrt{\frac{U_{e_o}\ell}{\nu_{e_o}}}$

$w(x)$ y-coordinate of solid surface

$\overline{W}$ $\overline{V} + \overline{U}\eta\,\frac{\dot{U}_e}{U_e}$

x,y coordinates of two-dimensional flow in physical plane

x_a, y_a coordinates of physical flow in the axisymmetric plane; x_a lies along centerline of body; for cylinder-flare combinations x_a is in inches measured from start of flare

x_a' axial distance from leading edge of cylinder-flare combination

x_o value of x where computer program is started

X,Y coordinates of the Stewartson transformation;

$$X = \int_o^x \frac{p_e a_e}{p_{e_o} a_{e_o}}\,dx; \qquad Y = \int_{w(x)}^{y} \frac{\rho_e a_e}{\rho_{e_o} a_{e_o}}\,\frac{\rho}{\rho_e}\,dy$$

α_n polynomial coefficients in equation (B-2)

β eddy-viscosity parameter

γ ratio of specific heats

δ boundary-layer thickness

δ^* displacement thickness

δ^*_{in} displacement thickness for an inviscid flow field defined by equation (126)

δ^*_m displacement thickness including any effect of normal pressure gradients, defined by equation (122)

δ^*_{vis} displacement thickness for boundary layer corrected for the effect of normal pressure gradients, $\delta^*_m - \delta^*_{in}$

ϵ absolute eddy viscosity

$\tilde{\zeta}$ Reynolds number based on laminar sublayer thickness, $\tilde{y}\tilde{u}_\tau/\tilde{\nu}$

θ momentum thickness in physical plane

θ_{in} momentum thickness for an inviscid flow field, defined by equation (127)

θ_m momentum thickness including any effect of normal pressure gradients, defined by equation (123)

θ_{vis} momentum thickness for boundary-layer corrected for the effect of normal pressure gradients, $\theta_m - \theta_{in}$

θ^* moment-of-momentum thickness, defined by equation (114)

μ absolute viscosity

ν kinematic viscosity, μ/ρ

ξ_o value of ξ corresponding to x_o

ξ, η coordinates in Dorodnitsyn plane,

$$\xi = \int_o^X \frac{U_e}{U_{e_o}} \frac{dx}{\ell}, \quad \eta = \frac{U_e}{U_{e_o}\ell}\sqrt{\frac{U_{e_o}\ell}{\nu_{e_o}}}\, Y$$

ρ local mass density

σ stream function stretching factor

σ_L laminar Prandtl number

σ_T turbulent Prandtl number

τ shear stress

ϕ body surface angle

ψ boundary-layer mass-flow parameter

$\overline{\psi}$ dimensionless, boundary-layer, mass-flow parameter

Subscripts

a axisymmetric

b predicted by boundary-layer theory

c adjusted for normal pressure gradients

e condition at the boundary-layer edge

m at match point of inner layer and wake

o initial condition at x_o

r reference condition

t stagnation condition

u unsteady turbulent quantity

w condition at the wall

∞ free-stream condition

Superscripts

$\cdot$ indicates differentiation with respect to ξ

$\sim$ indicates quantities in the incompressible turbulent plane

$\perp$ indicates time-averaged mean quantities

$'$ indicates quantities adjusted for normal pressure gradients

THEORY BASED ON THE METHOD OF INTEGRAL RELATIONS

The method of integral relations used herein is due to Dorodnitsyn (ref. 13). Its application to the turbulent case follows very closely that for laminar flow as described in references 10 through 12. In the following derivations the mathematical detail will be abbreviated.

This section is divided into two parts: one presenting the derivation of the ordinary differential equations and the other presents the eddy-viscosity model. The treatment is sufficiently general to accept other eddy-viscosity models. While a particular eddy-viscosity model was used during the course of this investigation, if a different and better

model is developed in the future, it would fit into the framework of the present analysis.

Derivation of the Ordinary Differential Equations

Assumptions.- Certain assumptions have been made during the course of this analysis. These assumptions are:

(1) The governing equations are those for a compressible turbulent boundary layer.

(2) The laminar and turbulent Prandtl numbers are unity.

(3) The air behaves as an ideal gas.

(4) The wall is at a uniform but arbitrary temperature.

(5) Within the range of interest, the molecular viscosity varies linearly with temperature.

(6) The conditions at the outer edge of the boundary layer are governed by isentropic flow relations.

(7) The temperature profile in the boundary layer is given by

$$\frac{T_t}{T_{t_e}} - 1 = S = S_w(1 - \overline{U}) \tag{1}$$

where

$$S_w = \frac{T_w}{T_{t_e}} - 1 \tag{2}$$

(8) It is assumed that the boundary-layer thickness is small compared to the body radius at the time the Mangler transformation is introduced.

Boundary-layer equations for compressible axisymmetric flow and their transformation to two-dimensional flow.- Reference 9 presents the boundary-layer equations for compressible turbulent flow in a convenient form for both axisymmetric and two-dimensional flow. In the following equations all flow properties are time averaged and bars will not be used to designate time averages. For axisymmetric flow the boundary-layer equations are:

Continuity:

$$\frac{\partial}{\partial x_a}(r\rho_a u_a) + \frac{\partial}{\partial y_a}(r\rho_a v_a) = 0 \tag{3}$$

Momentum:

$$\rho_a u_a \frac{\partial u_a}{\partial x_a} + (\rho_a v_a) \frac{\partial u_a}{\partial y_a} = - \frac{dp_a}{dx_a} + \frac{1}{r} \frac{\partial}{\partial y_a}\left(r\mu\beta_a \frac{\partial u_a}{\partial y_a} \right) \tag{4}$$

Energy:

$$\rho_a u_a \frac{\partial H_a}{\partial x_a} + (\rho_a v_a) \frac{\partial H_a}{\partial y_a} = \frac{1}{r} \frac{\partial}{\partial y_a}\left\{ r \left[\frac{\mu}{\sigma_L}\left(1 + \frac{\epsilon_a}{\mu} \frac{\sigma_L}{\sigma_T}\right) \frac{\partial H_a}{\partial y_a} + \mu\left(1 - \frac{1}{\sigma_L}\right) u_a \frac{\partial u_a}{\partial y_a} \right] \right\} \tag{5}$$

It should be noted that $(\rho_a v_a)$ is a single time-averaged quantity defined by

$$(\rho_a v_a) = \overline{\rho_a v_a} = \bar{\rho}_a \bar{v}_a + \overline{\rho_{a_u}' v_{a_u}'} \tag{6}$$

where

$(\rho_a v_a)$ = an inseparable quantity defined by equation (6)

$\bar{\rho}_a$ = time-averaged mean density

$\bar{v}_a$ = time-averaged mean velocity

ρ_{a_u} = fluctuating density component

v_{a_u} = fluctuating velocity component

We now introduce an eddy-viscosity parameter defined by

$$\beta_a = 1 + \frac{\epsilon_a}{\mu} \tag{7}$$

Assuming

$$\sigma_L = \sigma_T = 1 \tag{8}$$

reduces the energy equation to

$$\rho_a u_a \frac{\partial H_a}{\partial x_a} + (\rho_a v_a) \frac{\partial H_a}{\partial y_a} = \frac{1}{r} \frac{\partial}{\partial y_a}\left(r\mu\beta_a \frac{\partial H_a}{\partial y_a} \right) \tag{9}$$

Introducing a total temperature parameter produces the desired form of the energy equation:

$$\rho_a u_a \frac{\partial S_a}{\partial x_a} + (\rho_a v_a) \frac{\partial S_a}{\partial y_a} = \frac{1}{r} \frac{\partial}{\partial y_a} \left(r \mu \beta_a \frac{\partial S_a}{\partial y_a} \right) \tag{10}$$

where

$$S_a = \frac{\left(T_{t_a}\right)}{\left(T_{t_a}\right)_e} - 1 \tag{11}$$

The boundary conditions for this system of equations are:

$$\left.\begin{array}{lll} \text{At} \quad y_a = 0 & & u_a = v_a = 0 \\ \qquad r = r_w & & S_a = S_{a_w} \end{array}\right\} \tag{12}$$

$$\left.\begin{array}{lll} \text{At} \quad y_a = \infty & u_a = u_{a_e}(x) & \dfrac{\partial u_a}{\partial y_a} = 0 \\ & v_a = v_{a_e}(x) & \\ & S_a = 0 & \end{array}\right\} \tag{13}$$

The initial conditions are given as:

$$\left.\begin{array}{lll} \text{At} \quad x = x_o & & u_a = u_{a_o}(y) \\ & & S_a = S_{a_o}(y) \end{array}\right\} \tag{14}$$

At this point it is noted that the present x_a and y_a coordinates are parallel and perpendicular to the main flow, respectively, rather than tangent and normal to the local body surface. This convention implies that the streamwise slopes of the body surface are small compared to unity. It may lead to some loss of accuracy for curved plates at large surface slopes. The convention has the advantage that no ambiguity exists concerning the normal direction at discontinuities in surface slope.

Application of the Mangler transformation will reduce the system of axisymmetric equations to two-dimensional form. The Mangler transformation is:

$$r = r_w = \text{body radius} \tag{15}$$

$$x = \int_0^{x_a} r_w^2 dx_a \tag{16}$$

$$y = \int_{r_w}^{y_a} r_w \, dy_a \tag{17}$$

Under the transformation

$$\left.\begin{aligned} T &= T_a \\ p &= p_a \\ \rho &= \rho_a \\ u &= u_a \\ v &= \frac{v_a}{r} + \frac{u_a}{r_w^2}(y_a - 2r_w)\frac{dr_w}{dx_a} \end{aligned}\right\} \tag{18}$$

and the boundary conditions are:

$$\left.\begin{aligned} &\text{At} \quad y = 0 \qquad u = v = 0 \\ &\qquad\qquad\quad S = S_w \end{aligned}\right\} \tag{19}$$

$$\left.\begin{aligned} &\text{At} \quad y = \infty \qquad u = u_e(x) \qquad \frac{\partial u}{\partial y} = 0 \\ &\qquad\qquad\quad\;\; v = v_e(x) \\ &\qquad\qquad\quad\;\; S = 0 \end{aligned}\right\} \tag{20}$$

The initial conditions are:

$$\left.\begin{aligned} &\text{At} \quad x = x_o \qquad u = u_o(y) \\ &\qquad\qquad\quad S = S_o(y) \end{aligned}\right\} \tag{21}$$

The two-dimensional form of the boundary-layer equations results from the transformation, and these equations are presented in the following section. It is noted that dimensionality has not been preserved under the Mangler transformation.

Boundary-layer equations for compressible two-dimensional flow.- The boundary-layer equations for compressible turbulent boundary layers flowing over two-dimensional nonadiabatic bodies are:

Continuity:

$$\frac{\partial}{\partial x}(\rho u) + \frac{\partial}{\partial y}(\rho v) = 0 \tag{22}$$

Momentum:

$$\rho u \frac{\partial u}{\partial x} + (\rho v) \frac{\partial u}{\partial y} = - \frac{dp}{dx} + \frac{\partial}{\partial y}\left(\mu\beta \frac{\partial u}{\partial y}\right) \tag{23}$$

Energy:

$$\rho u \frac{\partial S}{\partial x} + (\rho v) \frac{\partial S}{\partial y} = \frac{dp}{dx} + \frac{\partial}{\partial y}\left(\mu\beta \frac{\partial S}{\partial y}\right) \tag{24}$$

As with the axisymmetric case, the following definition applies:

$$(\rho v) = \overline{\rho v} = \overline{\rho v} + \overline{\rho_u v_u}$$

The quantity (ρv) cannot be separated.

These equations are the same as in reference 9 except that the enthalpy H has been replaced by S. In the axisymmetric case the Mangler transformation has reduced the axisymmetric equations to the preceding form with the boundary conditions shown previously. The boundary conditions and initial conditions for the two-dimensional equations are the same as those given in equations (19) through (21).

Application of the Stewartson and Dorodnitsyn transformations.- In order to simplify further the equations, two transformations are now applied. The first of these is the Stewartson transformation given by

$$X = \int_0^x \frac{p_e a_e}{p_{e_o} a_{e_o}}\, dx \qquad Y = \int_{w(x)}^{Y} \frac{\rho_e a_e}{\rho_{e_o} a_{e_o}} \frac{\rho}{\rho_e}\, dy \tag{25}$$

and

$$\left.\begin{aligned} u &= \frac{a_e}{a_{e_o}} U \qquad v = \frac{p_e a_e}{p_{e_o} a_{e_o}} \frac{\rho_{e_o}}{\rho} V - \frac{\rho_{e_o}}{\rho} \frac{\partial Y}{\partial X} U \\ S &= S \end{aligned}\right\} \tag{26}$$

The resulting equations are:

Continuity:

$$\frac{\partial U}{\partial X} + \frac{\partial V}{\partial Y} = 0 \tag{27}$$

Momentum:

$$U \frac{\partial U}{\partial X} + V \frac{\partial U}{\partial Y} = (S + 1) U_e \frac{\partial U_e}{\partial X} + \nu_{e_o} \frac{\partial}{\partial Y} \left(\beta \frac{\partial U}{\partial Y} \right) \tag{28}$$

Energy:

$$U \frac{\partial S}{\partial X} + V \frac{\partial S}{\partial Y} = \nu_{e_o} \frac{\partial}{\partial Y} \left(\beta \frac{\partial S}{\partial Y} \right) \tag{29}$$

The assumption that molecular viscosity is a linear function of temperature has been used in the development of these equations. During the derivation β of the physical plane has been carried through a parameter so that

$$\beta(X,Y) = \beta(x,y) \tag{30}$$

Also, under the Dorodnitsyn transformation, we have

$$\beta(\xi,\eta) = \beta(X,Y) \tag{31}$$

The boundary conditions in the Stewartson plane are:

$$\left.\begin{array}{lll} \text{At} \quad y = 0 & U = V = 0 & \\ & S = S_w & \end{array}\right\} \tag{32}$$

$$\left.\begin{array}{lll} \text{At} \quad y = \infty & U = U_e(x) & \dfrac{\partial U}{\partial Y} = 0 \\ & V = V_e(X) = \dfrac{p_{e_o} a_{e_o}}{p_e a_e} \dfrac{\rho_e v_e}{\rho_{e_o}} + \dfrac{p_{e_o}}{p_e} \left(\dfrac{a_{e_o}}{a_e} \right)^2 \dfrac{\partial Y}{\partial X} u_e & \\ & S = 0 & \end{array}\right\} \tag{33}$$

The initial conditions are:

$$\left.\begin{array}{lll} \text{At} \quad X = X_o & U = U_o(Y) & \\ & S = S_o(Y) & \end{array}\right\} \tag{34}$$

The next step in the analysis is to apply the Dorodnitsyn transformation which is given by:

$$\xi = \frac{1}{\ell}\int_0^X \frac{U_e}{U_{e_o}}\,dX \qquad \eta = \frac{U_e}{U_{e_o}\ell}\sqrt{\frac{U_{e_o}\ell}{\nu_{e_o}}}\,Y \tag{35}$$

$$\left.\begin{aligned} \overline{U} &= \frac{U}{U_e} & \overline{V} &= \frac{V}{U_e}\sqrt{\frac{U_{e_o}\ell}{\nu_{e_o}}} \\ \overline{W} &= \overline{V} + \overline{U}\eta\,\frac{\dot{U}_e}{U_e} & S(\xi,\eta) &= S(X,Y) \end{aligned}\right\} \tag{36}$$

Under this transformation the differential equations become:

Continuity:

$$\frac{\partial\overline{U}}{\partial\xi} + \frac{\partial\overline{W}}{\partial\eta} = 0 \tag{37}$$

Momentum:

$$\overline{U}\,\frac{\partial\overline{U}}{\partial\xi} + \overline{W}\,\frac{\partial\overline{U}}{\partial\eta} = \left[(S+1) - \overline{U}^2\right]\frac{\dot{U}_e}{U_e} + \frac{\partial}{\partial\eta}\left(\beta\,\frac{\partial\overline{U}}{\partial\eta}\right) \tag{38}$$

Energy:

$$\overline{U}\,\frac{\partial S}{\partial\xi} + \overline{W}\,\frac{\partial S}{\partial\eta} = \frac{\partial}{\partial\eta}\left(\beta\,\frac{\partial S}{\partial\eta}\right) \tag{39}$$

The boundary conditions are:

$$\left.\begin{aligned} &\text{At}\quad \eta = 0 & \overline{U} &= \overline{V} = \overline{W} = 0 \\ & & S(\xi,0) &= S_w \end{aligned}\right\} \tag{40}$$

$$\left.\begin{aligned} &\text{At}\quad \eta = \infty \qquad \overline{U} = 1 \qquad \frac{\partial\overline{U}}{\partial\eta} = 0 \\ &S = 0 \\ &\overline{V} = \frac{1}{U_e}\sqrt{\frac{U_{e_o}\ell}{\nu_{e_o}}}\left(\frac{p_{e_o}a_{e_o}}{p_e a_e}\,\frac{1}{\rho_{e_o}}\,\rho_e v_e + \frac{\rho_{e_o}a_{e_o}}{a_e}\,\frac{\partial Y}{\partial X}\,u_e\right) \end{aligned}\right\} \tag{41}$$

The initial conditions are:

$$\left.\begin{aligned} \text{At} \quad \xi = \xi_o \qquad & \bar{U} = \bar{U}_o(\eta) \\ & S = S_o(\eta) \end{aligned}\right\} \tag{42}$$

Ordinary differential equations.- The analysis thus far has been perfectly general with regard to both velocity and temperature. At this point the Crocco relationship will be assumed thereby removing the necessity for an energy equation. The Crocco relationship provides the following coupling between total temperature and velocity profiles:

$$S = S_w(1 - \bar{U}) \tag{43}$$

The first step in reducing the continuity and momentum equations to ordinary differential equations is to select a set of weighting functions. The set selected for this analysis is:

$$f_i = (1 - \bar{U})\bar{U}^{(i-1)} \qquad i = 1,2,3,\cdots \tag{44}$$

Since the weighting functions are functions only of $\bar{U}$, their derivatives can be represented by:

$$f_i' = \frac{df_i}{d\bar{U}} \tag{45}$$

Multiplying the continuity equation by f_i, the momentum equation by f_i', and adding the two equations gives the following result:

$$\frac{\partial(f_i\bar{U})}{\partial\xi} + \frac{\partial(f_i\bar{W})}{\partial\eta} = f_i'\left[(S + 1) - \bar{U}^2\right]\frac{\dot{U}_e}{U_e} + f_i'\frac{\partial}{\partial\eta}\beta\frac{\partial\bar{U}}{\partial\eta} \tag{46}$$

Integration and rearrangement yields

$$\frac{d}{d\xi}\int_0^1 \frac{f_i\bar{U}\,d\bar{U}}{\partial\bar{U}/\partial\eta} = \frac{\dot{U}_e}{U_e}\int_0^1 \frac{f_i'\left[(S + 1) - \bar{U}^2\right]d\bar{U}}{\partial\bar{U}/\partial\eta} - \frac{f_i'(0)\beta(\xi,0)}{\partial\bar{U}/\partial\eta} - \int_0^1 f_i''\beta\frac{\partial\bar{U}}{\partial\eta}\,d\bar{U} \tag{47}$$

This equation is termed the integral form of the momentum equation. It is seen that as many equations can be obtained from equation (47) as there are weighting functions. It is necessary to select as many weighting

functions as there are unknown coefficients in the velocity-gradient representation. Two velocity-gradient representations have been utilized. The velocity-gradient representation which has proved most useful is termed the no-root representation, and is given by:

$$\frac{\partial \bar{U}}{\partial \eta} = \frac{(1 - \bar{U})}{\sum_{j=1}^{n} c_j \bar{U}^{(j-1)}} \tag{48}$$

The no-root velocity-gradient representation is valid everywhere in an attached flow region except at a separation point where $\partial \bar{U}/\partial \eta$ is zero.

Substituting equations (43), (44), and (48) into the integral form of the momentum equation (47) gives the following ordinary differential equations for the flow field:

$$\left.\begin{aligned}
&\frac{\dot{c}_1}{2} + \frac{\dot{c}_2}{3} + \frac{\dot{c}_3}{4} + \cdots + \frac{\dot{c}_n}{n+1} = RH_1 \\
&\frac{\dot{c}_1}{3} + \frac{\dot{c}_2}{4} + \frac{\dot{c}_3}{5} + \cdots + \frac{\dot{c}_n}{n+2} = RH_2 \\
&\frac{\dot{c}_1}{4} + \frac{\dot{c}_2}{5} + \frac{\dot{c}_3}{6} + \cdots + \frac{\dot{c}_n}{n+3} = RH_3 \\
&\vdots \\
&\frac{\dot{c}_1}{n+1} + \frac{\dot{c}_2}{n+2} + \frac{\dot{c}_3}{n+3} + \cdots + \frac{\dot{c}_n}{2n} = RH_n
\end{aligned}\right\} \tag{49}$$

where

$$RH_1 = \frac{\beta(\xi,0)}{c_1} - \left[(S_w + 1)\left(c_1 + \frac{c_2}{2} + \frac{c_3}{3} + \cdots + \frac{c_n}{n}\right) + \left(\frac{c_1}{2} + \frac{c_2}{3} + \frac{c_3}{4} + \cdots + \frac{c_n}{n+1}\right)\right]\frac{\dot{U}_e}{U_e} \tag{50a}$$

$$RH_2 = 2P_1 - \frac{\beta(\xi,0)}{c_1} + \left[(S_w + 1)\left(c_1 + \frac{c_2}{2} + \frac{c_3}{3} + \cdots + \frac{c_n}{n}\right) - (1 + 2S_w)\left(\frac{c_1}{2} + \frac{c_2}{3} + \frac{c_3}{4} + \cdots + \frac{c_n}{n+1}\right) - 2\left(\frac{c_1}{3} + \frac{c_2}{4} + \frac{c_3}{5} + \cdots + \frac{c_n}{n+2}\right)\right]\frac{\dot{U}_e}{U_e} \tag{50b}$$

$$RH_3 = 6P_2 - 2P_1 + \left[2(S_w + 1)\left(\frac{c_1}{2} + \frac{c_2}{3} + \frac{c_3}{4} + \cdots + \frac{c_n}{n+1}\right)\right.$$
$$-(1 + 3S_w)\left(\frac{c_1}{3} + \frac{c_2}{4} + \frac{c_3}{5} + \cdots + \frac{c_n}{n+2}\right)$$
$$\left.-3\left(\frac{c_1}{4} + \frac{c_2}{5} + \frac{c_3}{6} + \cdots + \frac{c_n}{n+3}\right)\right]\frac{\dot{U}_e}{U_e} \tag{50c}$$

$$RH_n = n(n-1)P_{n-1} - (n-1)(n-2)P_{n-2}$$
$$+\left\{(n-1)(S_w + 1)\left[\frac{c_1}{n-1} + \frac{c_2}{n} + \frac{c_3}{n+1} + \cdots + \frac{c_n}{(2n-2)}\right]\right.$$
$$-(1 + nS_w)\left(\frac{c_1}{n} + \frac{c_2}{n+1} + \frac{c_3}{n+2} + \cdots + \frac{c_n}{2n-1}\right)$$
$$\left.-n\left(\frac{c_1}{n+1} + \frac{c_2}{n+2} + \frac{c_3}{n+3} + \cdots + \frac{c_n}{2n}\right)\right\}\frac{\dot{U}_e}{U_e} \tag{50d}$$

The term $\beta(\xi,0)$, which is the eddy viscosity at the wall, can be set equal to unity except possibly at a separation point where $\partial\overline{U}/\partial\eta$ is zero. The P_i's, which occur in the nonhomogeneous terms on the right-hand sides, are definite integrals of the following set:

$$P_i = \int_0^1 \beta \frac{\partial\overline{U}}{\partial\eta}\overline{U}^{(i-1)}\, d\overline{U} \tag{51}$$

It is interesting to note that the only difference between the laminar and turbulent flow equations occurs in these integrals, where, for laminar flow, β is unity. The eddy-viscosity distribution for turbulent flow as used in the present work will be described subsequently.

The other velocity-gradient representation utilized in the present work is called the root formulation and is given by:

$$\frac{\partial\overline{U}}{\partial\eta} = \frac{(1 - \overline{U})\sqrt{\overline{U} + \overline{c}}}{c_1 + c_2\overline{U} + c_3\overline{U}^5} \tag{52}$$

In this case it is noted that particular exponents are used in the denominator as opposed to the previous case where general exponents were

used. The root representation is, however, valid everywhere in an attached flow field including the separation point. The analysis for the root case is more complex than for the no-root case because of the square-root term, $\sqrt{\bar{U} + \bar{c}}$.

This analysis proceeds the same as the previous one with equations (43), (44), and (52) being substituted into equation (47) to give the following ordinary differential equations:

$$\left.\begin{aligned} g_1\dot{c}_1 + g_2\dot{c}_2 + g_6\dot{c}_3 + (c_1g_1' + c_2g_2' + c_3g_6')\dot{\bar{c}} &= RS_1 \\ g_2\dot{c}_1 + g_3\dot{c}_2 + g_7\dot{c}_3 + (c_1g_2' + c_2g_3' + c_3g_7')\dot{\bar{c}} &= RS_2 \\ g_3\dot{c}_1 + g_4\dot{c}_2 + g_8\dot{c}_3 + (c_1g_3' + c_2g_4' + c_3g_8')\dot{\bar{c}} &= RS_3 \\ g_4\dot{c}_1 + g_5\dot{c}_2 + g_9\dot{c}_3 + (c_1g_4' + c_2g_5' + c_3g_9')\dot{\bar{c}} &= RS_4 \end{aligned}\right\} \tag{53}$$

where the right-hand sides are given by

$$RS_1 = \frac{\beta(\xi,0)\sqrt{\bar{c}}}{c_1} - \left[(1 + S_w)(c_1g_0 + c_2g_1 + c_3g_5) + (c_1g_1 + c_2g_2 + c_3g_6)\right]\frac{\dot{U}_e}{U_e} \tag{54a}$$

$$RS_2 = 2G_1 - \frac{\beta(\xi,0)\sqrt{\bar{c}}}{c_0} + \left[(1 + S_w)(c_1g_0 + c_2g_1 + c_3g_5) - (1 + 2S_w)(c_1g_1 + c_2g_2 + c_3g_6) - 2(c_1g_2 + c_2g_3 + c_3g_7)\right]\frac{\dot{U}_e}{U_e} \tag{54b}$$

$$RS_3 = 6G_2 - 2G_1 + \left[2(1 + S_w)(c_1g_1 + c_2g_2 + c_3g_6) - (1 + 3S_w)(c_1g_2 + c_2g_3 + c_3g_7) - 3(c_1g_3 + c_2g_4 + c_3g_8)\right]\frac{\dot{U}_e}{U_e} \tag{54c}$$

$$RS_4 = 12G_3 - 6G_2 + \left[3(1 + S_w)(c_1g_2 + c_2g_3 + c_3g_7) - (1 + 4S_w)(c_1g_3 + c_2g_4 + c_3g_8) - 4(c_1g_4 + c_2g_5 + c_3g_9)\right]\frac{\dot{U}_e}{U_e} \tag{54d}$$

The g_i's which occur in these equations are definite integrals from the following set:

$$g_i(\bar{c}) = \int_0^1 \frac{\bar{U}^i \, d\bar{U}}{\sqrt{\bar{U} + \bar{c}}} \qquad i = 0,1,2,\cdots \tag{55}$$

and

$$g_i'(\bar{c}) = \frac{dg_i}{d\bar{c}} = -\frac{1}{2} \int_0^1 \frac{\bar{U}^i \, d\bar{U}}{(\bar{U} + \bar{c})^{3/2}} \qquad i = 0,1,2,\cdots \tag{56}$$

As with the no-root formulation the term $\beta(\xi,0)$ is the eddy viscosity at the wall, which can be set equal to unity except possibly at a separation point. The eddy viscosity again enters the analysis through the definite integrals contained in the nonhomogeneous terms. The definite integrals are members of the following set:

$$G_i = \int_0^1 \frac{\beta(1 - \bar{U})\bar{U}^{(i-1)}\sqrt{\bar{U} + \bar{c}}}{c_1 + c_2\bar{U} + c_3\bar{U}^5} \, d\bar{U} \tag{57}$$

The same eddy-viscosity models used for the no-root formulation can be used with this formulation.

Auxiliary equations.- This section is being presented for completeness in order to provide equations for the principal quantities of interest. The derivations will be omitted since they are not difficult.

The relationships between the axisymmetric quantities of interest and the corresponding two-dimensional quantities follow.

Skin friction:

$$c_{f_a} = \frac{\mu_{a_w} \left.\dfrac{\partial u_a}{\partial y_a}\right|_w}{\frac{1}{2} \rho_{a_e} u_{a_e}^2} = rc_f \tag{58}$$

Displacement thickness:

$$\delta_a^* = \int_{r_w}^{r_w+\delta_a} \left(1 - \frac{\rho_a u_a}{\rho_{a_e} u_{a_e}}\right) dy_a = \frac{1}{r_w} \int_0^{\delta} \left(1 - \frac{\rho u}{\rho_e u_e}\right) dy = \frac{\delta^*}{r_w} \tag{59}$$

Momentum thickness:

$$\theta_a = \int_{r_w}^{r_w+\delta_a} \frac{\rho_a u_a}{\rho_{a_e} u_{a_e}} \left(1 - \frac{u_a}{u_{a_e}}\right) dy_a = \frac{1}{r_w} \int_0^{\delta} \frac{\rho u}{\rho_e u_e} \left(1 - \frac{u}{u_e}\right) dy = \frac{\theta}{r_w} \tag{60}$$

Reference length:

$$\ell = r_{w_o}{}^2 L \tag{61}$$

Velocity gradient:

$$\frac{\partial (u_a/u_{a_e})}{\partial (y_a/L)} = \frac{r_w}{r_{w_o}{}^2} \frac{\partial (u/u_e)}{\partial (y/\ell)} \tag{62}$$

Velocity profile:

$$y_a - r_w = \frac{y}{r_w} \quad \text{and} \quad u_a = u \tag{63}$$

Mass flow:

$$\psi_a = 2\pi \int_0^{y_a} \rho_a u_a r_w \, dy_a \tag{64}$$

$$\overline{\psi}_a = \frac{\psi_a}{2\pi \mu_{e_o} r_w{}^2 \sqrt{\frac{\rho_{a_o} u_{a_o} L}{\mu_{a_o}}}} = \frac{\psi}{\mu_{e_o} \sqrt{\frac{\rho_{e_o} u_{e_o} \ell}{\mu_{e_o}}}} = \overline{\psi} \tag{65}$$

where

$$\psi = \int_0^{y} \rho u \, dy \tag{66}$$

In the two-dimensional plane the quantities of interest are obtained for the no-root formulation from the following relationships:

Skin friction:

$$c_f = \frac{\mu_w \left.\frac{\partial u}{\partial y}\right|_w}{\frac{1}{2}\rho_e u_e^2} = \frac{2}{\sqrt{R_{\ell_o}}} \left(\frac{1 + m_{e_o}}{1 + m_e}\right) \frac{1}{c_1} \tag{67}$$

where

$$R_{\ell_o} = \frac{u_{e_o} \ell}{\nu_{e_o}} \tag{68}$$

$$m = \frac{\gamma - 1}{2} M^2 \tag{69}$$

Displacement thickness:

$$\delta^* = \int_o^\delta \left(1 - \frac{\rho u}{\rho_e u_e}\right) dy \tag{70}$$

$$\delta^* = \frac{\ell}{\frac{U_e}{U_{e_o}}\sqrt{R_{\ell_o}}} \left(\frac{1 + m_e}{1 + m_{e_o}}\right)^{\frac{\gamma+1}{2(\gamma-1)}} \left[(1 + S_w)(1 + m_e) \sum_{j=1}^{n} \frac{c_j}{j} + m_e \sum_{j=1}^{n} \frac{c_j}{j+1}\right] \tag{71}$$

Momentum thickness:

$$\theta = \int_o^\delta \frac{\rho u}{\rho_e u_e} \left(1 - \frac{u}{u_e}\right) dy \tag{72}$$

$$\theta = \frac{\ell}{\frac{U_e}{U_{e_o}}\sqrt{R_{\ell_o}}} \left(\frac{1 + m_e}{1 + m_{e_o}}\right)^{\frac{\gamma+1}{2(\gamma-1)}} \left[\sum_{j=1}^{n} \frac{c_j}{j+1}\right] \tag{73}$$

Velocity gradient:

$$\frac{\partial\left(\frac{u}{u_e}\right)}{\partial\left(\frac{y}{\ell}\right)} = \frac{U_e}{U_{e_o}}\sqrt{R_{\ell_o}}\left(\frac{1 + m_{e_o}}{1 + m_e}\right)^{\frac{\gamma+1}{2(\gamma-1)}} \frac{1}{\left[(1 + S_w)(1 + m_e) - S_w(1 + m_e)\overline{U} - m_e\overline{U}^2\right]} \frac{(1 - \overline{U})}{\sum_{j=1}^{n} c_j \overline{U}^{(j-1)}} \tag{74}$$

Velocity profile:

$$y - w(x) = \frac{\ell}{\frac{U_e}{U_{e_o}}\sqrt{R_{\ell_o}}}\left(\frac{1 + m_e}{1 + m_{e_o}}\right)^{\frac{\gamma+1}{2(\gamma-1)}}\left\{\eta + \left[S_w(1 + m_e) + m_e\right]\sum_{j=1}^{n}\frac{c_j\overline{U}^j}{j} + m_e\sum_{j=1}^{n}\frac{c_j\overline{U}^{(j+1)}}{j+1}\right\} \tag{75}$$

and

$$\eta = \sum_{j=1}^{n} c_j F_j \tag{76}$$

where

$$F_j = \int_0^{\overline{U}} \frac{\overline{U}^{(j-1)}}{(1 - \overline{U})}\, d\overline{U} \tag{77}$$

Thus,

$$\left.\begin{aligned} F_1 &= -\ln(1 - \overline{U}) \\ F_j &= F_{j-1} - \frac{U^{(j-1)}}{(j-1)} \qquad j = 2,3,4,\cdots \end{aligned}\right\} \tag{78}$$

Mass flow:

$$\overline{\psi} = \int_0^{Y} \rho u\, dy \tag{79}$$

$$\overline{\psi} = \frac{\psi}{\mu_{e_o}\sqrt{R_{\ell_o}}} = \sum_{j=1}^{n} c_j F_{j+1} \tag{80}$$

The corresponding equations for the square-root formulation are:

Skin friction:

$$c_f = \frac{2}{\sqrt{R_{\ell_o}}} \left(\frac{1 + m_{e_o}}{1 + m_e}\right) \frac{\sqrt{\overline{c}}}{c_1} \tag{81}$$

Displacement thickness:

$$\delta^* = \frac{\ell}{\frac{U_e}{U_{e_o}}\sqrt{R_{\ell_o}}} \left(\frac{1 + m_e}{1 + m_{e_o}}\right)^{\frac{\gamma+1}{2(\gamma-1)}} \Big[(1 + S_w)(1 + m_e)(c_1 g_o + c_2 g_1 + c_3 g_5) + m_e(c_1 g_1 + c_2 g_2 + c_3 g_6)\Big] \tag{82}$$

Momentum thickness:

$$\theta = \frac{\ell}{\frac{U_e}{U_{e_o}}\sqrt{R_{\ell_o}}} \left(\frac{1 + m_e}{1 + m_{e_o}}\right)^{\frac{\gamma+1}{2(\gamma-1)}} (c_1 g_1 + c_2 g_2 + c_3 g_6) \tag{83}$$

Velocity gradient:

$$\frac{\partial\left(\frac{u}{u_e}\right)}{\partial\left(\frac{y}{\ell}\right)} = \frac{U_e}{U_{e_o}} \sqrt{R_{\ell_o}} \left(\frac{1 + m_{e_o}}{1 + m_e}\right)^{\frac{\gamma+1}{2(\gamma-1)}} \left[\frac{1}{(1 + S_w)(1 + m_e) - (1 + m_e) S_w \overline{U} - m_e \overline{U}^2}\right] \frac{(1 - \overline{U})\sqrt{\overline{U} + \overline{c}}}{(c_1 + c_2 \overline{U} + c_3 \overline{U}^5)} \tag{84}$$

Velocity profile:

$$y - w(x) = \frac{\ell}{\frac{U_e}{U_{e_o}}\sqrt{R_{\ell_o}}} \left(\frac{1 + m_e}{1 + m_{e_o}}\right)^{\frac{\gamma+1}{2(\gamma-1)}} \left\{\eta + \left[S_w(1 + m_e) + m_e\right](c_1\overline{F}_1 + c_2\overline{F}_2 + c_3\overline{F}_6) + m_e(c_1\overline{F}_2 + c_2\overline{F}_3 + c_3\overline{F}_7)\right\} \tag{85}$$

and

$$\eta = -c_3(\overline{F}_1 + \overline{F}_2 + \overline{F}_3 + \overline{F}_4 + \overline{F}_5) - c_2\overline{F}_1 + \frac{(c_1 + c_2 + c_3)}{\sqrt{\overline{c} + 1}} \ln\left[\frac{\left(\sqrt{\overline{c} + \overline{U}} + \sqrt{\overline{c} + 1}\right)\left(\sqrt{\overline{c}} - \sqrt{\overline{c} + 1}\right)}{\left(\sqrt{\overline{c} + \overline{U}} - \sqrt{\overline{c} + 1}\right)\left(\sqrt{\overline{c}} + \sqrt{\overline{c} + 1}\right)}\right] \tag{86}$$

where

$$\overline{F}_i = \int_0^{\overline{U}} \frac{\overline{U}^{(i-1)}}{\sqrt{\overline{U} + \overline{c}}}\, d\overline{U} \tag{87}$$

Thus,

$$\left.\begin{aligned} \overline{F}_1 &= 2\left(\sqrt{\overline{U} + \overline{c}} - \sqrt{\overline{c}}\right) \\ \overline{F}_i &= \frac{2}{2i - 1}\left[\overline{U}^{(i-1)}\sqrt{\overline{U} + \overline{c}} - (i - 1)\overline{c}\overline{F}_{(i-1)}\right] \qquad i = 2,3,4,\cdots \end{aligned}\right\} \tag{88}$$

Mass flow:

$$\overline{\psi} = -c_3(\overline{F}_3 + \overline{F}_4 + \overline{F}_5 + \overline{F}_6) - (c_2 + c_3)\overline{F}_2 - (c_1 + c_2 + c_3)\left\{\overline{F}_1 - \frac{1}{\sqrt{1 + \overline{c}}} \ln\left[\frac{\left(\sqrt{\overline{c} + \overline{U}} + \sqrt{1 + \overline{c}}\right)\left(\sqrt{\overline{c}} - \sqrt{1 + \overline{c}}\right)}{\left(\sqrt{\overline{c} + \overline{U}} - \sqrt{1 + \overline{c}}\right)\left(\sqrt{\overline{c}} + \sqrt{1 + \overline{c}}\right)}\right]\right\} \tag{89}$$

Eddy-Viscosity Parameter

The distribution of the eddy-viscosity parameter, β, that enters the P_i and G_i integrals is the actual distribution for the compressible nonadiabatic turbulent layer. It has not been transformed under the Stewartson or Dorodnitsyn transformations but has simply been carried along as a variable. Since the integrals are evaluated by numerical means, fairly complicated eddy-viscosity models can be used in the theory.

Incompressible eddy-viscosity model.- The detailed work is contained in Appendix A. This section contains only a basic description of the model and a summary of the pertinent results. The basic model is an incompressible one. For compressible flow the eddy-viscosity distribution is related to an equivalent incompressible one using the method outlined by Baronti and Libby in reference 14. This method is based on the transformation theory developed by Coles (ref. 15) and the sublayer hypothesis set forth by Donaldson (ref. 16).

The incompressible eddy-viscosity model is based on an inner layer where the shear is assumed constant and an outer layer where the eddy viscosity is assumed constant (ref. 17). The inner layer consists of a laminar sublayer, a buffer layer, and a region where the law of the wall is valid. The buffer layer is an arbitrary layer between the laminar sublayer and the law of the wall region where a fairing has been introduced to prevent a discontinuity in the eddy-viscosity distribution. Within the laminar sublayer the eddy-viscosity parameter β is unity, and in the region of the law of the wall it is obtained from well-known velocity correlations assuming the shear is constant at the wall value.

Within the outer layer, or wake region, the eddy-viscosity is constant and equal to the value prescribed by Clauser (ref. 17). The boundary between the inner and outer layers is established by assuming that the value of the eddy viscosity is continuous at the point of the join.

The eddy-viscosity parameter for the entire boundary layer is given by the following equations for the various regions.

Laminar sublayer:

$$\tilde{\beta} = 1.0 \qquad 0 \leq \frac{\tilde{u}}{\tilde{u}_\tau} \leq 7.95 \tag{90}$$

Buffer layer:

$$\tilde{\beta} = e^{0.4811\left[(\tilde{u}/\tilde{u}_\tau)-7.95\right]} \qquad 7.95 < \frac{\tilde{u}}{\tilde{u}_\tau} < 13.25 \tag{91}$$

Law-of-the-wall region:

$$\tilde{\beta} = \frac{1}{18.225} e^{(1/2.43)(\tilde{u}/\tilde{u}_\tau)} \qquad 13.25 \leq \frac{\tilde{u}}{\tilde{u}_\tau} < \left(\frac{\tilde{u}}{\tilde{u}}\right)_m \tag{92}$$

Wake:

$$\tilde{\beta} = 0.018\ \tilde{R}_{\delta *} \qquad \left(\frac{\tilde{u}}{\tilde{u}_\tau}\right)_m \leq \frac{\tilde{u}}{\tilde{u}_\tau} \tag{93}$$

The distribution of the incompressible eddy-viscosity parameter is shown in figure 1 in a way which displays the effect of Reynolds number. As the Reynolds number increases, the boundary between the inner layer and the wake moves to higher values of $\tilde{u}/\tilde{u}_\tau$ and $\tilde{\beta}$.

Compressible eddy-viscosity model.- The velocity profile for the inner layer of a compressible boundary layer is related to that for an equivalent incompressible boundary layer in accordance with the method given in reference 14. Under the assumptions of the method, which employs the Baronti-Libby transformation, the nondimensional velocity ratios and the eddy-viscosity parameters are equal at corresponding points in the compressible and incompressible boundary layers.

$$\frac{u}{u_e} = \frac{\tilde{u}}{\tilde{u}_e} \tag{94}$$

$$\beta = \tilde{\beta} \tag{95}$$

To evaluate the eddy-viscosity integrals, P_i and G_i, it is necessary to know β as a function of u/u_e. We need only know the skin-friction coefficient of the equivalent incompressible layer, $\tilde{c}_f$, to obtain the desired information from equations (94) and (95). The value of $\tilde{c}_f$ is obtained by solving the following two equations by iteration:

$$\tilde{c}_f = \frac{\tilde{\mu}}{\sigma \mu_e} c_f \tag{96}$$

$$\frac{\mu_e \sigma}{\tilde{\mu}} = \left(\frac{\rho_f}{\rho_e}\right)\left(\frac{\mu_e}{\mu_f}\right)\left[\frac{T_w}{T_e} + \left(\frac{T_{t_e}}{T_e} - \frac{T_w}{T_e}\right)\left(\frac{\tilde{c}_f}{2}\right)^{1/2} \frac{10.6}{2} - \left(\frac{T_{t_e}}{T_e} - 1\right)\left(\frac{\tilde{c}_f}{2}\right) \frac{(10.6)^2}{3}\right] \tag{97}$$

The value of u/u_e is obtained from $\tilde{c}_f$ through

$$\frac{u}{u_e} = \frac{\tilde{u}}{\tilde{u}_\tau} \sqrt{\frac{\tilde{c}_f}{2}} \tag{98}$$

and the value of $\tilde{\beta}$ is obtained from equations (90) through (92).

The first problem in obtaining β in the wake region of a compressible boundary layer is to find the point of the join. It is possible to find the point of the join from the condition that β of the inner layer equals β obtained from the Clauser relationship. An assumption is made for this purpose that the Baronti-Libby transformations can be used across the entire boundary layer in establishing the relationship between the compressible displacement and boundary-layer thicknesses and the equivalent incompressible thicknesses. The assumption is a fairly good one because the wake does not contribute much to the displacement and momentum thicknesses, and the velocity transformation is valid at the outer edge of the boundary layer. These considerations lead to the following result for the eddy-viscosity at the point of the join:

$$\beta = \beta_m = 0.018 \frac{T_e}{T_w} \left(\frac{\mu_e \sigma}{\tilde{\mu}} \right) (R_{\delta *} - m_e R_\theta) \tag{99}$$

In the wake itself, β is proportional to density and inversely proportional to viscosity. Since viscosity has been assumed proportional to temperature, and hence inversely proportional to density, it follows that β is proportional to density squared. Thus, in the wake region the eddy-viscosity parameter is given by:

$$\beta = \beta_m \left(\frac{\rho}{\rho_m} \right)^2 \tag{100}$$

CHOICE OF VELOCITY-GRADIENT REPRESENTATIONS

A study has been made to aid in the selection of the best velocity-gradient representation for the computer program. This study involves the fitting of various velocity-gradient representations to empirical flat-plate velocity-gradient profiles using the method of least squares. The accuracy of fit for the various representations is a factor in the choice of the one considered best suited for use in the analysis. As a by-product,

the least-squares fitting provides approximate initial conditions for starting subsequent solutions.

The velocity-gradient representations considered are:

No-root formulation:

$$\frac{\partial \overline{U}}{\partial \eta} = \frac{(1 - \overline{U})}{c_1 + c_2 \overline{U}^m + c_3 \overline{U}^n} \tag{101}$$

Root formulation:

$$\frac{\partial \overline{U}}{\partial \eta} = \frac{(1 - \overline{U})\sqrt{\overline{U} + \overline{c}}}{c_1 + c_2 \overline{U}^m + c_3 \overline{U}^n} \tag{102}$$

The empirical flat-plate profiles to be fit were obtained using Spalding's (ref. 18) generalized law of the wall combined with an analytic fit to Coles' (ref. 19) wake function. This combination was used in order to provide a continuous velocity profile which could be differentiated analytically for fitting purposes. In order to utilize these flat-plate velocity profiles, it is necessary that they be in the form

$$\frac{\tilde{u}}{\tilde{u}_e} = f(\eta) \tag{103}$$

The empirical profiles could be put into this form with the skin-friction coefficient, $\tilde{c}_f$, and the form factor, $\tilde{H}$, as parameters. In addition the condition that $\tilde{u}/\tilde{u}_e = 1$ at $\tilde{y} = \tilde{\delta}$ was imposed. However, the resulting profiles did not meet the condition that

$$\frac{\partial \overline{u}}{\partial \eta} = 0 \quad \text{at} \quad \overline{u} = 1 \tag{104}$$

The skin-friction coefficient and the form factor used for the flat-plate velocity profiles were obtained in the following ways. The skin-friction coefficient was predicted on the basis of flat-plate equations given by Sommer and Short (ref. 20) for incompressible flow:

$$\tilde{c}_f = 0.0578(\tilde{R}_x)^{1/5} \tag{105}$$

Clauser (ref. 17) presents the following form-factor correlation for incompressible zero pressure-gradient boundary layers

$$\tilde{H} = \frac{1}{1 - 6.8\sqrt{\tilde{c}_f/2}} \tag{106}$$

The empirical flat-plate velocity profile thus is a function only of $\tilde{R}_x$.

The empirical velocity profiles used in this study are for zero Mach number, adiabatic walls, and Reynolds numbers of 10^4 through 10^8. The velocity-gradient representations given by equations (101) and (102) were fit to the empirical profiles for the following matrix of m and n:

m \ n	2	3	4	5	6
1	✕	✕	✕	✕	✕
2		✕	✕	✕	✕
3			✕	✕	✕
4				✕	✕

It is of interest to look at the second derivative evaluated at the wall for the various representations. For the no-root formulation, assuming $n > m$, there is obtained

$$\left.\frac{\partial^2 \bar{U}}{\partial \eta^2}\right|_w = \left(-\frac{1}{c_1} - \frac{c_2}{c_1^2}\right)\frac{1}{c_1} \qquad m = 1 \tag{107}$$

$$\left.\frac{\partial^2 \bar{U}}{\partial \eta^2}\right|_w = -\frac{1}{c_1^2} \qquad m \geq 2 \tag{108}$$

The corresponding results for the root formulation still, assuming $n > m$, are:

$$\left.\frac{\partial^2 \bar{U}}{\partial \eta^2}\right|_w = \left(-\frac{\sqrt{\bar{c}}}{c_1} - \frac{\sqrt{\bar{c}}c_2}{c_1^2} + \frac{1}{2c_1\sqrt{\bar{c}}}\right)\frac{\sqrt{\bar{c}}}{c_1} \qquad m = 1 \tag{109}$$

$$\left.\frac{\partial^2 \bar{U}}{\partial \eta^2}\right|_w = \left(-\frac{\sqrt{\bar{c}}}{c_1} + \frac{1}{2\sqrt{\bar{c}}c_1}\right)\frac{\sqrt{\bar{c}}}{c_1} \qquad m \geq 2 \tag{110}$$

For positive skin friction, c_1 must be positive. For this case these equations show that with $m = 1$ any value, positive or negative, may be obtained for the second derivative at the wall with either formulation depending upon the sign and value of c_2. However, for m greater than 1, only negative values of the second derivative can be obtained for positive skin friction using the no-root formulation. These facts indicate that $m = 1$ should be included in the no-root formulation to include the possibility that the second derivative be zero at the wall for zero pressure gradient in accordance with boundary-layer theory. However, other values of m have been included in the studies for completeness.

The incompressible empirical flat-plate turbulent velocity gradients generated by the method previously described are shown as curves in figures 2 and 3. Also shown in the figures as symbols are the various fits obtained using the no-root and the root formulations. For the no-root formulation with $m = 1$ and $n = 3$ the fit seems better at low Reynolds number. For $m = 1$ and $n = 5$ the fit seems better at higher Reynolds numbers. Since high Reynolds numbers are of interest for turbulent boundary layers, it is felt that $m = 1$ and $n = 5$ offers the best overall fit for flat plates.

The results obtained for the root formulation, figure 3, are similar to those obtained for the no-root formulation. Here, however, the formulation with $m = 1$ and $n = 5$ yields a good fit over the entire Reynolds number range for flat plates.

Computer programs using the no-root formulation have been written using both $n = 2$ and 5. No preference of one over the other was found between similar computer runs. Under adverse pressure gradients, as the velocity profiles tend toward separated profiles, they are not nearly so full as flat-plate profiles at large Reynolds numbers. It appears that the less full profiles should be fit better with $n = 2$ than with $n = 5$. Accordingly, $n = 2$ was chosen as the exponent to use in the no-root velocity-gradient representation.

For the root velocity-gradient representation the exponents $m = 1$ and $n = 5$ were adopted. These exponents were adopted in view of the conclusions reached in the least-squares fitting study. It was also found that using a computer program based on $m = 1$ and $n = 2$, a convergent solution was not obtained. The reason for this behavior is not known.

DESCRIPTION OF COMPUTER PROGRAMS

During the course of this investigation several computer programs for turbulent boundary layers were generated. These programs are based on various velocity-gradient representations and eddy-viscosity models. Two of these are important with regard to the work reported herein.

The first program is one for the calculation of turbulent boundary layers on nonadiabatic two-dimensional or axisymmetric bodies with prescribed pressure distribution. A manual for this computer program, reference 21, has been written. The computer program is based on the no-root velocity-gradient representation with $m = 1$ and $n = 2$, and the eddy-viscosity model used is that previously described. The body shapes for either the two-dimensional or axisymmetric cases are introduced into the program in the form of segmented polynomials. The pressure distribution is introduced into the program in the same fashion as the body shapes. It is this program that has been used to make many predictions for comparison between experiment and theory.

The second program is based on the root velocity-gradient representation and the eddy-viscosity model previously described. The program is valid only for flat-plate configurations with a zero pressure gradient. Since the program is so limited, it has not been described in detail in any published documents. The program, when generalized to handle pressure gradients, contains the inherent possibility of being mathematically valid at separation.

It is noteworthy that the first computer program has upper and lower bounds of Reynolds number beyond which it will not operate properly. These limits are given in the manual for the program, reference 21.

INITIAL CONDITIONS

To start a boundary-layer solution requires initial values of the c_i's for the no-root formulation and of the c_i's and $\bar{c}$ for the root formulation. Obtaining initial conditions is a difficult problem associated with using the present computer program. Several methods have been developed for obtaining initial conditions, and these methods will now be presented.

The discussion of initial conditions has been divided into three main parts. In the first part general methods for obtaining initial conditions to start any problem are presented for both the root and no-root formulations. In the second part solutions for flat plates with no pressure gradients are discussed. These solutions can be used to start other types of solutions in many cases. The third and final part contains a discussion of the recommended procedure for obtaining initial conditions when an arbitrary pressure gradient occurs.

General Methods for Obtaining Initial Conditions

In this section two general methods are presented for finding initial conditions. The first method involves fitting a velocity profile with the velocity-gradient formulation to obtain the initial c_i's. The second method involves the solution of simultaneous equations in terms of such initial boundary-layer properties as skin-friction coefficient, displacement thickness, and momentum thickness. The first method can only be used when an initial velocity profile is given. The second method can be used when either a velocity profile or gross properties are given since gross properties can be obtained from the profile.

Least-squares method.- The method of least squares used above in the study of velocity-gradient representation can also be used to generate initial conditions. For incompressible adiabatic flow the method is direct. For compressible flows it becomes more complicated since the compressible profile must be transformed to the Dorodnitsyn plane. In view of this complication least-squares fitting of compressible velocity profiles was not carried out herein.

An approximate method of obtaining initial conditions from the least-squares method for compressible velocity profiles is to use the Baronti-Libby method, reference 14. The c_i's to be used for initial conditions are those obtained by fitting an equivalent incompressible velocity profile. The equivalent incompressible velocity profile corresponds to the incompressible skin-friction coefficient, $\tilde{c}_f$, and form factor $\tilde{H}$, found using the Baronti-Libby transformation. To find $\tilde{c}_f$, equations (96) and (97) are solved simultaneously. The form factor, $\tilde{H}$, is then obtained using equation (106) and the value obtained for $\tilde{c}_f$. With these two parameters, $\tilde{c}_f$ and $\tilde{H}$, an incompressible velocity profile can be constructed

for fitting purposes. The resulting c_i's can be used to start the compressible boundary-layer solution.

Initial conditions have been generated for several velocity-gradient representations for a wide range of flow conditions. These initial conditions were a by-product of the velocity-gradient representation study discussed previously. Results for both root and no-root formulations with $m = 1$ for $n = 2$ and 5 are presented in table I for incompressible flat-plate, adiabatic boundary layers with no pressure gradients.

The equations used in the least-squares method are described in detail in reference 21.

Gross properties method.- A second general method for obtaining initial conditions utilizes gross boundary-layer properties. It is assumed that the skin-friction coefficient, the displacement thickness, and the momentum thickness are either given or can be calculated from a given velocity profile. The simultaneous equations to be solved for the c_i's of the no-root formulation are:

Skin-friction coefficient:

$$c_f = \frac{2}{\sqrt{R_{\ell_o}}} \frac{1}{c_1} \tag{111}$$

Momentum thickness:

$$\theta = \frac{\ell}{\sqrt{R_{\ell_o}}} \left(\frac{c_1}{2} + \frac{c_2}{m+2} + \frac{c_3}{n+2} \right) \tag{112}$$

Displacement thickness:

$$\delta^* = \frac{\ell}{\sqrt{R_{\ell_o}}} (1 + m_e)(1 + S_w) \left(c_1 + \frac{c_2}{m+1} + \frac{c_3}{n+1} \right) + m_e \theta \tag{113}$$

It is a simple matter to solve these equations given c_f, δ^*, and θ. This method has been used successfully to obtain initial conditions. One difficulty has arisen for a case where $m = 1$ and $n = 2$. Consider the polynomial $c_1 + c_2\overline{U} + c_3\overline{U}^2$ that occurs in the denominator of the velocity-gradient representation. The c_i's obtained for the case in question resulted in roots of the polynomial in the range $0 \leq \overline{U} \leq 1$ so that $\partial\overline{U}/\partial\eta$

was infinite in the boundary layer. A slight perturbation in the value of momentum thickness, which could be within the experimental error, was found to cure the difficulty. Usually the roots of the polynomial are complex so that no infinity in $\partial\overline{U}/\partial\eta$ occurs in the boundary layer.

The application of the boundary-layer properties method to the root velocity-gradient representation involves four variables. Another gross property of the boundary layer must, therefore, be known. Such a property might be the moment-of-momentum thickness defined as

$$\theta^* = \int_0^\delta \frac{\rho u^2}{\rho_e u_e{}^2}\left(1 - \frac{u}{u_e}\right)dy \tag{114}$$

For the root formulation with $m = 1$ and $n = 5$ there is obtained

$$\theta^* = \frac{\ell}{\frac{U_e}{U_{e_o}}\sqrt{R_{\ell_o}}}\left(\frac{1 + m_e}{1 + m_{e_o}}\right)^{\frac{(\gamma+1)}{2(\gamma-1)}}(c_1 g_2 + c_2 g_3 + c_3 g_7) \tag{115}$$

The thermal energy thickness, which is another gross property frequently known, could not have been used in the present case because through the Crocco relationship it is identical with the momentum thickness.

Equations (81), (82), (83), and (115) can be solved simultaneously for the four unknowns $\overline{c}$, c_1, c_2, and c_3. For this solution m_e would be taken equal to m_{e_o}. This solution is not easy because of the g_i's which are complicated functions of $\overline{c}$. An iterative solution on a computer appears to be the best way to obtain a solution. The boundary-layer properties method has not been used during the present investigation for the root formulation case.

Initial Conditions in the Absence of Pressure Gradient

The computer program applied to boundary layers on flat plates or cylinders with sharp leading edges and no imposed pressure gradients will develop asymptotic or locked-in solutions. These locked-in solutions, which are the unique solutions for these configurations, are useful in

two respects. First they provide predictions for comparison with flat-plate data, which is the most common type of data available. Secondly, many solutions with pressure gradients can be started using the flat-plate initial conditions. If the pressure gradients prior to the desired start of calculations are zero everywhere, then these flat-plate solutions represent precise initial conditions. Even when pressure gradients exist at the starting point, flat-plate initial conditions are frequently very good.

Obtaining the locked-in flat-plate solutions is sometimes difficult and usually requires several computer runs. The solutions are generally started from an initial set of conditions obtained from some approximate scheme such as the general methods already presented. Then a flat-plate computer run over one or two orders of magnitude in axial distance is made. After a short transient, the resulting solution develops a long-term trend, such as a logarithmic variation, which indicates that it is locked in.

For the no-root formulation the c_i's obtained from a computer run after a long axial distance are then plotted and extrapolated back to the starting point. Using these new c_i's the same process is repeated until a locked-in solution is generated. Typical results obtained using the no-root program are shown in figure 4. The initial c_i's used for the first run were obtained by least-squares fitting and the Baronti and Libby method discussed previously. It is seen that the solution locked into a logarithmic trend very quickly. Two back extrapolations were required to establish the final solution.

Flat-plate solutions for the no-root formulation over a large matrix of Mach number, Reynolds number, and temperature ratio show that the c_i's versus axial distance followed straight lines on log-log paper. In addition, the skin-friction coefficient, displacement thickness, and momentum thicknesses are straight lines on log-log paper when plotted versus axial distance. This linear property allows presentation of a large matrix of initial conditions in the relatively short table, table II. The values shown in this table for the c_i's, skin-friction coefficient, displacement thickness, and momentum thickness for $x = 1.0$ and 10.0 allow the reader to establish values within the range by simply drawing straight lines on log-log paper. Extrapolation of the lines plotted outside of the range is dangerous but can be done within certain limits of Reynolds number to establish approximate initial conditions.

The wide range of flat-plate initial conditions was not generated for the root formulations for several reasons. In the first place the root program is not nearly so fast as the no-root program, and long runs cannot be generated quickly. In addition, the variation of $\overline{c}$ and the c_i's with axial distance is not linear on log-log paper. The only flat-plate solution generated during the present investigation for a zero Mach number adiabatic wall over a wide Reynolds number range is shown in figure 5. The figure shows an upper limit on the Reynolds number for which the root program will operate. At a Reynolds number of about $R_x = 10^8$, the c_i's tend to infinity. In this figure the predicted skin-friction coefficient is compared to those obtained from correlation laws of known validity. For these comparisons the numerical method of references 22 and 23 have been used. The agreement between prediction and experiment is considered good. While a convergent solution has been found for $m = 1$ and $n = 5$, only divergent solutions have been experienced for $m = 1$ and $n = 2$.

Initial Conditions with Pressure Gradients Present

Problems involving pressure gradients can be divided into two categories, those for which the initial conditions correspond to zero gradients and those for which they do not. In the second case the initial pressure gradient can be either positive or negative. This section considers initial conditions for the no-root formulation only since calculations with pressure gradients have not been made for the root formulation.

Any one of the previously presented methods for obtaining initial conditions may be useful for starting solutions with pressure gradients. It is recommended that the flat-plate solution be used as a first approximation even when pressure gradients are present. The c_i's for the locked-in flat-plate solution are then chosen to correspond to the edge flow conditions and some known boundary-layer quantities such as skin-friction coefficient, displacement thickness, or momentum thickness. It may not be possible to match all three boundary-layer quantities with flat-plate c_i's. This result follows from the fact that if the skin-friction coefficient is specified for a flat plate, then either displacement thickness or momentum thickness can be independently specified, but not both. In the case of severe pressure gradients acting on the boundary

layer in front of a location where initial conditions are to be specified, it is probable that flat-plate initial conditions will not provide a good first approximation.

If the initial conditions cannot be approximated by flat-plate initial conditions, then either one of the other two methods mentioned in the section on general methods can be used to start a pressure-gradient solution. Of these two methods the one preferred is the gross properties method. Here the skin-friction coefficient, displacement thickness, and momentum thickness are used to establish the initial values of the c_i's. This method guarantees that these initial gross properties are correct. Also, the method sets the eddy-viscosity model at the correct initial turbulence level since the model is a function of skin-friction coefficient and Reynolds number based on displacement thickness.

The least-squares method will work equally as well as the gross properties method, although it does not necessarily set the initial turbulence level precisely since a precise value of displacement thickness is not guaranteed by a least-squares fit to a velocity-gradient profile. The results using this method, however, appear to be equally as good as those obtained using the gross properties method. In both cases initial transients are small if the input data used to obtain the initial conditions are compatible with each other and with the pressure gradient to be imposed. For example, for a given initial pressure gradient, a given skin-friction coefficient, and a given displacement thickness, there is only one value of momentum thickness and thus one set of c_i's which will allow a solution of the boundary-layer equations to continue without transients.

COMPARISON BETWEEN EXPERIMENT AND THEORY FOR THE TWO-DIMENSIONAL CASE

In order to test the present theory a number of comparisons have been made between experimental results and theoretical predictions from the computer program based on the no-root formulation. The results obtained are presented in the following paragraphs for a wide range of speeds for two-dimensional configurations. The first two cases considered are for incompressible flow, and the subsequent cases are for supersonic flow.

Configuration of Schubauer-Klebanoff

In reference 24 Schubauer and Klebanoff present the results of a low-speed investigation of turbulent boundary layers on a streamlined configuration, the pressure distribution of which is controlled by a protuberance on the wind-tunnel wall. The resulting pressure distribution acting on the boundary layer is shown in figure 6 together with an analytical fit to the distribution. The analytical fit to the pressure distribution, used as input to the boundary-layer program, utilizes segmented polynomials of varying degree as shown in the figure. The initial conditions for the boundary-layer calculations were obtained using the gross properties method.

In figure 7(a) the predicted skin-friction coefficient is compared with the experimental skin-friction coefficient. The experimental skin-friction coefficients are not the ones to be found in reference 24, which were obtained from the momentum equation applied at the wall in conjunction with an extrapolation of turbulent shearing stress to the wall. These results are believed by the present authors to be in error. The experimental results presented in figure 7(a) were obtained at Stanford University by matching the experimental velocity profiles, presented in reference 24, to the law of the wall. The agreement between experiment and theory is good for the entire range of falling pressure and for about 3 feet of the 8 feet of adverse pressure gradient preceding separation.

The agreement between experiment and theory shown in figures 7(b) and (c) for displacement thickness and momentum thickness is also good for about one-half to two-thirds of the length of adverse pressure gradient preceding separation. Several possible causes exist for the lack of agreement in the neighborhood of separation. First the no-root velocity-gradient representation used for this analysis cannot reproduce the zero wall shear at separation. How far ahead of separation this mathematical ill-conditioning will have an influence is not known. Another possible cause of lack of agreement is the eddy-viscosity model being used. While the present model does not appear ill-conditioned at separation, there exists no experimental proof of its validity there. An additional question that has arisen concerning experimental low-speed turbulent boundary layers is whether they obey the two-dimensional boundary-layer equations at separation.

Figure 8 presents comparisons between experimental and predicted velocity profiles at selected stations. Figure 8(a) shows the initial velocity profile where the agreement is good. Figure 8(b) shows the agreement still to be good after about 6 feet of strong favorable pressure gradient. The agreement remains good through the nearly constant pressure region, as shown in figure 7(c), and continues into the strong adverse pressure-gradient region, as shown by figure 7(d). However, as separation is approached the agreement between theory and experiment deteriorates rapidly, until in figure 8(f) just before separation, it is not good at all. It cannot be said for certain what the exact cause of lack of agreement is, although the three factors previously mentioned could all be contributing.

Low-Speed Airfoil Data of Newman

Extensive, low-speed, turbulent, boundary-layer measurements have been presented in reference 25 by Newman for an airfoil configuration, a sketch of which is shown in figure 9. Also shown in the sketch are the stations at which boundary-layer traverses were made. It will be noted that all measurements were made on the lee side of the airfoil in the region of adverse pressure gradients.

The initial conditions for this run were established using the gross boundary-layer properties method discussed previously. The skin-friction coefficient, displacement thickness, and the momentum thickness were used to obtain the initial c_i's at station B. At station B the initial Mach number was 0.12 and the reference Reynolds number per foot was 8.23×10^5 (1/ft).

The pressure distribution which resulted on the wing is shown in figure 10 along with a straight-line fit. A straight-line fit was considered adequate because the pressure coefficients could not be read accurately from the very small figure in reference 25.

In figure 11(a) the predicted displacement and momentum thicknesses are compared with the experimental values of these quantities. Both predicted quantities agree well with the experimental quantities except near the trailing edge where the predicted thicknesses tend to be too large. At station G the boundary layer is nearly separated, and the no-root formulation cannot go to separation. Thus, the good agreement between the

predicted and experimental values of δ^* and θ approaching the trailing edge is encouraging.

The predicted skin-friction coefficient variation is compared with experimental data in figure 11(b). The overall agreement between experiment and theory is considered fair.

In figure 12 predicted and experimental velocity profiles are compared. Figure 12(a) shows the initial velocity profile at station B, where gross boundary-layer properties were matched to start the calculations. The agreement between experiment and theory is considered fair here as well as at the two other stations. It should be noted that Newman considers that his flow approaching the separation point does not obey two-dimensional equations.

Hypersonic Turbulent Layer on Flat Plate With and Without Oblique Shock Impingement

Data were obtained on a flat plate 4 feet long on which an oblique shock wave could be induced by a wedge. The data used in this section for comparison with theory were taken during the course of the experimental investigation reported in reference 26. The specific data used herein were not incorporated in reference 26. Two measuring stations were used. The 2.17-foot station is near the middle of the interaction zone for a 5° shock generator while the 2.95-foot station is just downstream of the interaction zone. All distances are measured from the plate leading edge.

To start the flat-plate solution, initial conditions were obtained from table II by interpolation for the initial Mach number, Reynolds number, and temperature ratio shown in figure 13. The velocity profiles resulting from the zero pressure-gradient solution are compared with the experimental ones in figures 13(a) and 13(b). For both positions agreement between prediction and theory is good for this zero pressure-gradient case.

As a matter of interest the temperature profile at station 2.17 is compared in figure 13(c) with the predicted profile. It is seen that the comparison is quite good except near the wall. The two data points at the wall show how much the wall temperature rose during the run. The accuracy of the temperature measurements near the wall because of errors induced by the presence of the wall is unknown.

Figure 14 shows the experimental pressure distribution resulting from shock-wave, boundary-layer, interaction as well as the analytic fit to the experimental pressure distribution used as input to the boundary-layer program. The boundary-layer thickness prior to interaction is about 0.03 foot, and the entire pressure rise occurs in approximately 10 boundary-layer thicknesses. Pressure gradients of this type are considered severe.

The flow edge conditions were determined from the isentropic flow relations and the pressure distribution for the incident-shock case. Figure 15 shows a comparison between the predicted and experimental displacement and momentum thicknesses for the flat plate with and without shock impingement. The agreement between experiment and theory for the displacement thickness is very good for both cases. For the momentum thickness, however, the agreement is not as good with the zero-pressure-gradient prediction lying above the data and the pressure-gradient prediction lying below the datum point. In the case of a shock-wave, boundary-layer interaction, agreement between experiment and theory might be expected upstream and downstream of the shock impingement. However, within the interaction zone no agreement can be expected since the theory does not account for the fact that the incident shock penetrates deep into the layer. The measuring station for the incident shock case is quite close to the downstream end of the pressure rise, and the boundary layer has not yet become an equilibrium one. Disagreement between experiment and theory could arise from this cause.

No experimental skin-friction data were available for this case, but as a matter of interest the predicted variation of c_f is shown in figure 16 with and without pressure gradients. For comparison with the zero-pressure-gradient prediction the skin-friction coefficient variation obtained using the method outlined in reference 22 is presented. Agreement between these two predictions is good except near the leading edge. The figure shows two qualitative effects for the pressure-gradient case; first, the skin-friction coefficient decreases as it does approaching a separation point; and secondly, the downstream skin-friction variation is above the flat-plate value for no pressure gradients.

In figure 17 the velocity profiles are compared at the one available station where data were taken for the shock impingement case. It appears that the experimental profile has not yet completely filled out after traversing the interaction region.

Compression Surface Tested at $M_\infty = 7.4$

The configuration for this case is the 4-foot-long compression ramp shown in figure 18. All data presented in this report are published in reference 26 except the velocity profile data. In the present case the pressure rise occurs over approximately 100 boundary-layer thicknesses. The boundary-layer thickness at the first measuring station was 0.0233 foot.

Nonisentropic edge conditions not accounted for in the computer program made it difficult to determine accurate initial conditions for the computer run. While the pressure distribution is known over most of the length of the compression surface, displacement and momentum thicknesses are known only at the two measuring stations. As shown in figure 19, the pressure distribution is smooth and the analytical fit to the distribution is good. The distribution of edge Mach number and Reynolds number per foot are shown based on isentropic edge conditions starting from an initial edge Mach number of 6.07 and an initial Reynolds number per foot of 1.825×10^6. These two values were selected so that the curves would go through the experimental points for the first station. However, it is seen from the lack of agreement at the downstream station that the edge conditions are not even approximately isentropic probably because of curvature of the bow shock. However, it was decided to proceed with the calculation on the assumption of isentropic edge conditions. The initial conditions were taken to be locked-in flat-plate conditions obtained from table II by interpolation using the initial Mach number and Reynolds number per unit length previously quoted.

The results of the boundary-layer calculation are compared with experiment in figure 20 for displacement thickness and momentum thickness. The agreement at the first measuring station has been forced as previously mentioned. The agreement at the downstream measuring station is not very good. The disagreement between experiment and theory shown for this case may be the result of inaccurate initial conditions and nonisentropic edge effects. The importance of the nonisentropic edge conditions can be assessed by including them as a future option in the computer program.

In figure 21 a comparison between the predicted and measured velocity profile at the first data-taking station is made. The good agreement of the experimental and predicted velocity profiles is helped by the enforced agreement of the values of δ^* and θ at this station.

Compression Surface Tested at $M_\infty = 10.4$

The configuration for this case is the same as for the previous case and is shown in figure 18. As with the previous case all data used herein are to be found in reference 26 except for the velocity profile data.

The experimental pressure distribution for M_∞ of 10.4 is shown in figure 22(a) together with the analytically fitted curves. While the compression is not severe, the pressure rise occurs over approximately 150 boundary-layer thicknesses. The boundary-layer edge conditions for this case are nonisentropic because of bow-shock curvature. The nonisentropic edge effect is illustrated by figure 22(b), which shows edge Mach number, and figure 22(c), which shows edge Reynolds number per foot. In these figures the lines representing isentropic conditions according to the experimental pressure distribution were made to match the data at the first measuring station. The deviation of the lines from the data at the second measuring station illustrates the extent of the nonisentropic edge condition. The edge conditions for this case with $M_\infty = 10.4$ appear more closely isentropic than at $M_\infty = 7.4$.

Figure 23 shows the comparison of the predicted values and the experimental values of δ^* and θ at the two measuring stations. The enforced fit at the first station is seen. The agreement at the second station is fair.

Figure 24 shows the comparison of the calculated and measured velocity profiles at $x = 2.17$ feet. As with the previous case good agreement at the upstream measuring station was obtained.

One point of difference between the $M_\infty = 10.4$ data and the $M_\infty = 7.4$ data for this configuration exists. At the higher Mach number the boundary layer was tripped near the leading edge while at the lower Mach number natural transition occurred.

Boundary-Layer, Shock-Wave Interaction Data of Pinckney

Pinckney in reference 27 presents data for boundary-layer, shock-wave interaction on a flat plate with a sharp leading edge and with an incident oblique shock. The set of data used for comparison purposes is represented by the runs of reference 27 numbered 46, 48, and 50. A 2-foot-long flat plate lies ahead of the instrumentation area. The initial

edge Mach number was 1.97 and the initial Reynolds number per foot was 8.48×10^6.

The experimental pressure distribution for the present case is shown in figure 25 together with the edge flow conditions. The pressure distribution was fit with 5 segmented polynomials as shown in figure 25(a) for use in the boundary-layer program. With this fitted pressure distribution, the resulting edge Mach numbers and Reynolds number per unit length computed using isentropic flow relations are seen to be in very good agreement with the experimental values at the three measuring stations.

Initial conditions for this case were obtained from a locked-in flat-plate solution started with values obtained from table II(b). The momentum- and displacement-thickness comparisons are shown in figure 26. A scatter band has been estimated for the data in figure 26 as indicated on each point. It is seen that the experimental and theoretical values of momentum thickness are in good agreement. The agreement for displacement thickness, however, is not nearly so good as for momentum thickness. Within the interaction zone the difference is about 20 percent of the displacement thickness and after the shock impingement the difference is about 15 percent. The agreement within the interaction zone is not expected to be good, but downstream the effect of shocks in the boundary layer should damp out, and the agreement should improve.

Figure 27 presents the predicted skin-friction variation for this case. However, reference 27 presented no skin-friction data.

In figure 28 the predicted velocity profiles are compared with the experimental profiles. Ahead of the shock the theoretical velocity profile agrees well with the data as shown in figure 28(a). The scatter of the data occurred with one run. For the next measuring station, figure 28(b), the profile is in the interaction zone and the agreement is not good. The experimental profile has taken on the appearance of a profile near separation but the predicted profile has not. At the last measuring station, figure 28(c), the agreement has improved over the previous measuring station.

COMPARISON BETWEEN EXPERIMENT AND THEORY FOR AN AXISYMMETRIC CONFIGURATION

Comparison has been made between predictions of the present theory and a set of data (ref. 28) for a turbulent boundary layer on a axisymmetric configuration consisting of a hollow, circular cylinder culminating in a compression flare. The flare is of such shape that large pressure gradients are generated normal to the compression surface at the test Mach number of 5.75. Boundary-layer profiles of total pressure and static pressure at a series of stations were measured as well as surface heat-transfer rates.

In the following sections, several methods of comparison between theory and experiment will be used. In reference 28, data have been corrected for pressure gradients normal to the flare surface by the method of reference 29, and the corrected data will be compared with the predictions of present theory. In the second case, the present boundary-layer theory will be adjusted for normal pressure gradients, and the adjusted theory will be compared with the uncorrected data.

Description of Model and Data

A tabulation of the compression surface dimensions is given in Appendix B of reference 30. The inclination of the compression surface reaches an angle of 42° at its downstream end.

The pressures at the wall and the edge of the boundary layer as a fraction of the free-stream total pressure have been read from figures 23 to 34 of reference 28, and these data are listed in table III. Since the data are for even values of ϕ, the x coordinates are not evenly spaced. There is no pressure drop across the boundary layer at the beginning of the flare, but the edge pressure is only about 50 percent of the wall pressure for values of ϕ between 7.5° and 35°.

It is possible from the data of reference 28 to evaluate the stagnation pressure distribution at the edge of the boundary layer and thereby to assess the degree to which the flow outside the boundary layer is isentropic. Both the edge static pressure, p_e, and pitot pressure p_{t_2}, are given as fractions of the free-stream stagnation pressure, p_{t_∞}. Even though the edge stagnation pressure p_{t_1} is different from p_{t_∞}, the ratio of p_e/p_{t_2} should yield the local Mach number and the ratio

p_{t_1}/p_{t_2}. The local stagnation pressure as a fraction of free-stream total pressure is then

$$\frac{p_{t_1}}{p_{t_\infty}} = \left(\frac{p_{t_1}}{p_{t_2}}\right)\left(\frac{p_{t_2}}{p_{t_\infty}}\right) \tag{116}$$

In table IV the edge Mach number and total pressure ratio obtained by the foregoing method are shown. It is noted that the edge total pressure increases above the value of p_{t_∞} at first and falls beneath this value at a value of ϕ between 25° and 30°. Since in principle the edge total pressure cannot exceed p_{t_∞}, some unknown inaccuracy appears to be present in the data. The theory presented herein does not account for total pressure variations at the edge of the boundary layer.

Input Quantities for Computer Program

The slope of the compression surface has been fitted with segmented polynomials in x_a to provide an input to the computer program. The pressure distribution has also been fitted with segmented polynomials. The details are included in Appendix B. In figure 29 the tabulated slopes from reference 30 are compared with those given by the polynomial fits. The second derivative d^2r/dx_a^2 is also shown as determined from the polynomials. A comparison of the pressure distributions given by the polynomials with the experimental distribution is shown in figure 30.

In addition to the foregoing input quantities, the following quantities were used as initial conditions

$$\left.\begin{aligned} M_{e_o} &= 5.75 \\ T_w/T_{t_e} &= 0.634 \\ R_{\ell_o}/\ell &= 3.6\times10^7 \end{aligned}\right\} \tag{117}$$

The initial values of the c_i's were obtained using the gross properties method. The experimental values of the properties were

$$\left.\begin{aligned} \delta_a^* &= 0.01333 \text{ ft} \\ \theta_a &= 0.001066 \text{ ft} \\ c_{f_a} &= 6.32\times10^{-4} \end{aligned}\right\} \tag{118}$$

The value of skin friction was obtained through Reynolds analogy using the experimental value of the heat-transfer rate at the juncture between the cylinder and the flare. The quoted value from figure 103 of reference 28 is

$$q_{w_a} = 2.6 \text{ Btu/ft}^2\text{-sec} \tag{119}$$

In this case the experimental values for displacement thickness, momentum thickness, and skin friction gave roots of the velocity gradient polynomial in the range $0 \leq \overline{U} \leq 1.0$. In order to cure the problem the momentum thickness was adjusted to force the roots to be complex. The adjustment required was well within the experimental error, and the new value of momentum thickness was 1.030×10^{-3} ft.

Comparison Between Prediction and Data of Hoydysh and Zakkay

Comparisons are made between the predictions of the present method and the displacement thickness and momentum thickness measurements of reference 28, as corrected therein for normal pressure gradients. Also, comparison will be made between predicted and measured Mach number profiles rather than velocity profiles since the Crocco relationship was assumed in obtaining experimental velocity profiles. Heat-transfer rates measured on the compression surface will be compared with those obtained from the computer program.

Pressure distribution.- It is of interest to know how the pressure distribution acting on the compression surface compares with that predicted from shock-expansion theory. The shock-expansion static pressure, p_{se}, divided by that for $\phi = 0$ is shown in table III. It is seen that the surface pressure lies slightly below the shock-expansion theory for all values of ϕ. Precise agreement would not be expected because of normal pressure gradients, nonisentropic flow at the edge of the boundary layer, and boundary-layer displacement effects.

Reference quantities and corrections to data.- Corrections, which are not always small compared to the uncorrected values, have been applied in reference 28 to both displacement thickness and momentum thickness to account for normal pressure gradients. The determination of these corrections and the choice of reference conditions needs discussion. The definitions of δ^* and θ contain a reference velocity and density, u_r and ρ_r, as follows:

$$\delta^* = \int_0^\delta \left(1 - \frac{\rho u}{\rho_r u_r}\right) dy \tag{120}$$

$$\theta = \int_0^\delta \frac{\rho u}{\rho_r u_r}\left(1 - \frac{u}{u_r}\right) dy \tag{121}$$

The values of ρ and u at the outer edge of the boundary layer with the normal pressure gradients present are not appropriate reference quantities in this instance because we are "correcting" the data to the case of no normal pressure gradient. Consider a purely inviscid flow in which the pressure distribution is identical to that for the real flow but throughout which the entropy is uniform. This "reference" flow is the basis for both the reference conditions and the corrections. Let the primed symbols refer to quantities in the reference flow. Then ρ_w' and u_w' are taken to be the reference density and velocity for the present purposes in accordance with the work of references 28 and 29. The quantities ρ_w' and u_w' are also the values of ρ and u at the edge of the boundary layer if the static pressure there were brought up to wall pressure at constant free-stream entropy. As such they represent edge conditions for no normal pressure gradients. Accordingly, we have

$$\delta_m^* = \int_0^\delta \left(1 - \frac{\rho u}{\rho_w' u_w'}\right) dy \tag{122}$$

$$\theta_m = \int_0^\delta \frac{\rho u}{\rho_w' u_w'}\left(1 - \frac{u'}{u_w'}\right) dy \tag{123}$$

The correction procedure is a gross one based on the assumption that the values of δ^* and θ for the reference flow can be subtracted from the values for the real flow to account for normal pressure gradients. The theoretical basis for such a procedure does not seem to be given in references 28 or 29. However, on the basis of such an assumption, we can write

$$\theta_m = \theta_{vis} + \theta_{in} \tag{124}$$

$$\delta_m^* = \delta_{vis}^* + \delta_{in}^* \tag{125}$$

The inviscid values of θ and δ^*, which represent the effect of normal pressure gradients, are thus written

$$\delta^*_{in} = \int_0^{\delta} \left(1 - \frac{\rho'u'}{\rho'_w u'_w}\right) dy \tag{126}$$

$$\theta_{in} = \int_0^{\delta} \frac{\rho'u'}{\rho'_w u'_w}\left(1 - \frac{u'}{u'_w}\right) dy \tag{127}$$

In the reference flow the velocity u' increases as distance from the wall increases since the static pressure is falling and the complete flow is isentropic. Accordingly, the ratio u'/u'_w is greater than unity and θ_{in} is negative. Since the Mach number increases supersonically as we move away from the wall, the ratio $\rho'u'/\rho'_w u'_w$ decreases below unity, and δ^*_{in} is positive.

Displacement and momentum thicknesses.- The δ^* comparisons are shown in figure 31(a), and the θ comparisons are shown in figure 31(b). In figure 31(a) the circles represent δ^*_m, and the squares represent δ^*_{vis} as obtained from equation (125). Comparison of δ^*_{vis} with the prediction of the present computer program shows good agreement even at large values of ϕ. The corrections to the data are generally a large percentage of the uncorrected values. At large values of ϕ the theory is invalid.

In figure 31(b) the comparison between experiment and theory for θ shows good agreement. The data in this figure represent revisions to the corresponding data of reference 28 in accordance with a private communication received from an author of that report.

Heat-transfer rate.- Heat-transfer rates were measured at a number of points on the compression surface. The ratio of the local heat-transfer rate to that at the beginning of the compression surface has been determined from the present computer program for comparison with these data. The ratio has been obtained from the Reynolds analogy.

$$St = \frac{q_w}{c_p \rho'_w u'_w \left(T_{t_e} - T_w\right)} = \frac{c_f}{2} \tag{128}$$

The ratio of heat-transfer rates is then

$$\frac{q_w}{q_{w_o}} = \frac{(c_f \rho_w' u_w')}{(c_f \rho_w' u_w')_o} \tag{129}$$

The calculated and experimental values of these ratios are shown in figure 32. The general agreement between theory and experiment is good.

Mach number profiles.- A comparison between the prediction and experimental Mach number profiles is shown in figure 33 for various values of ϕ. At the beginning of the flare, $\phi = 0$, the profiles are in fair agreement. The Mach numbers at the edge of the layer are identical since no normal pressure gradients are present. As ϕ increases the experimental Mach number at the edge of the boundary layer becomes greater than the predicted Mach number because the edge pressure is less than wall pressure. For $\phi = 5^o$ an adjustment has been made to the theoretical Mach number profile to account for normal pressure gradients. It has been assumed that at any point in the boundary layer the static pressure drops isentropically from the wall value to the local measured value. Accordingly, the local Mach number increases. There is little change in profile in the inner layer, and the profiles come into good agreement in the outer part of the layer. At large values of ϕ, the boundary-layer thickness is underestimated.

Adjustment of Boundary-Layer Calculation for Normal Pressure Gradient

The method of correcting boundary-layer data for normal pressure gradients as done in references 28 and 29 makes use of experimental values of the boundary-layer thickness and the static and total pressure profiles. The corrected data are then compared with boundary-layer theory. It is of interest to reverse the above process and predict the experimental boundary-layer characteristics by adjusting boundary-layer theory for normal pressure gradients. Since the experimental values of the boundary-layer thickness and the pressure profiles are not available for this purpose, some additional assumptions are required to carry out the adjustment.

An approximate method for adjusting boundary-layer theory for normal pressure gradients was formulated on relatively simple grounds. The method furnishes first approximations to the magnitude of the corrections

to δ^* and θ due to normal pressure gradients and indicates how important normal pressure-gradient effects are on boundary-layer quantities in any particular case.

Normal pressure gradients.- One of the first problems is to estimate the magnitude of the normal pressure gradients. An estimate can be obtained from a method of characteristics solution for isentropic flow over the compression surface. If such a solution is unavailable, a simple method based on shock-expansion theory can be used. According to reference 31, the equation for the pressure gradient normal to the streamlines of a compressible isentropic flow is

$$\frac{\partial p}{\partial n} = -\rho v_t^2 k_s \tag{130}$$

where v_t is the velocity along the streamline and k_s is the curvature of the streamline given by

$$k_s = \frac{d^2r/dx_a^2}{\sqrt{1 + (dr/dx_a)^2}} \tag{131}$$

If M_w is the Mach number at the wall obtained from shock-expansion theory, equation (130) becomes

$$\frac{1}{p}\frac{\partial p}{\partial n} = -\gamma M_w^2 k_s \tag{132}$$

Equation (132) yields a simple first approximation to the magnitude of the normal gradients.

Equation (132) has been applied to the flare of reference 28. The values of dr_a/ds given in Appendix B of reference 30 were used in evaluating k_s in equation (131), and the first differences of dr_a/ds were used to evaluate $\partial^2 r_a/\partial s^2$. The Mach number M_w based on shock-expansion theory applied to the flare slope were also used. The calculated curve of $(1/p)(\partial p/\partial n)$ is shown in figure 34. Also shown in this figure are the experimental values of $(1/p_w)(p_w - p_e)/\delta$. This parameter represents the average value of the normal pressure gradient across the boundary layer. For values of ϕ below 10°, the predicted results exceed the experimental results. It is noted that at the flare-cylinder juncture the curvature jumps almost discontinuously from 0 to a finite value

(fig. 29). The flow at the wall may respond immediately to this discontinuous change, but the entire boundary layer cannot. In fact in this case it takes about 8 boundary-layer thicknesses for the entire boundary layer to achieve the predicted normal pressure gradient. At angles much above 25° the normal pressure gradients are underpredicted.

Adjustments to δ^* and θ.- The adjustment of the Mach number profile for normal pressure gradients discussed in connection with figure 33(b) suggests an approach for estimating incremental values of δ^* and θ due to the gradients. The adjusted Mach number profile is obtained by permitting the pressure at all points in the boundary layer to fall from wall pressure to local static pressure at constant local entropy. As shown in figure 33(b), the effect near the wall is negligible so that no change in skin-friction coefficient is involved. However, the velocity profiles are changed significantly in the outer part of the layer, and in particular the edge conditions are brought into agreement. The incremental values of δ^* and θ, namely $\Delta\delta^*$ and $\Delta\theta$, are then simply the differences in δ^* and θ between the adjusted profile and the unadjusted profile. In this scheme the increments are calculated for a small perturbation of the boundary-layer profile.

Let values of u, ρ, δ^*, and θ predicted by boundary-layer theory be indicated by u_b, ρ_b, δ_b^*, and θ_b, respectively. Let the symbols with a subscript "c" correspond to the "adjusted" Mach number profile. Then using the former reference conditions, ρ_w' and u_w', we have

$$\delta_b^* = \int_0^{\delta} \left(1 - \frac{\rho_b u_b}{\rho_w' u_w'}\right) dy \tag{133}$$

$$\theta_b = \int_0^{\delta} \frac{\rho_b u_b}{\rho_w' u_w'} \left(1 - \frac{u_b}{u_w'}\right) dy \tag{134}$$

Note that at the edge of the boundary layer

$$u_b = u_w'$$

$$\rho_b = \rho_w'$$

From equations (120) and (121), the values of δ_c^* and θ_c for the adjusted profile with the same reference conditions are

$$\delta_c^* = \int_0^{\delta} \left(1 - \frac{\rho_c u_c}{\rho_w' u_w'}\right) dy \tag{135}$$

$$\theta_c = \int_0^{\delta} \frac{\rho_c u_c}{\rho_w' u_w'} \left(1 - \frac{u_c}{u_w'}\right) dy \tag{136}$$

The incremental values $\Delta\delta^*$ and $\Delta\theta$ due to normal pressure gradients are then

$$\Delta\delta^* = \delta_c^* - \delta_b^* \tag{137}$$

$$\Delta\theta = \theta_c - \theta_b \tag{138}$$

The value of δ used in these formulas corresponds to y for $\overline{U} = 0.999$. No adjustments were made for the expansion of the local stream tubes during the expansion from the conditions denoted by "b" to those denoted by "c". Such adjustments, if made, would introduce a stretching of the y scale.

In order to test these prediction techniques the values of δ_c^* and θ_c with normal pressure gradients have been predicted for the compression flare case of reference 28. The predicted Mach number profiles in figure 33 were adjusted using the experimental static-pressure distributions. The experimental static-pressure distributions were used so that any errors in static-pressure prediction would not mask the accuracy of the boundary-layer adjustment calculation. The adjusted values of δ_c^* and θ_c are compared with the data of reference 28 in figures 35(a) and 35(b), respectively. The predictions of δ^* and θ are considered fair. The data of figure 35(b), like those of figure 31(b), represented revisions of the corresponding data in reference 28.

TURBULENT BOUNDARY-LAYER, SHOCK-WAVE INTERACTION MODEL

The present computer program has been used to make detailed studies of the interaction between turbulent boundary layers and oblique shock

waves with a view to developing a boundary-layer model for studying such interactions. On the basis of the studies a promising model is proposed.

In turbulent boundary-layer, shock-wave interaction, the shock wave penetrates deeply into the boundary layer, and the usual boundary-layer assumption of constant pressure across the boundary layer is not met (ref. 32). This fact requires the concept of an ideal boundary-layer model for such interactions. The ideal boundary-layer model results from the solution of the turbulent boundary-layer equations for the given experimental pressure distribution assuming the static pressure to be constant across the boundary layer. The part of the boundary-layer flow for the ideal model beneath the δ^* line should correspond closely to the part of the real flow beneath the δ^* line. The outer boundary-layer flow will not be in good agreement with the real flow because of the presence of shock waves in the real flow. Based on the results of Watson, Murphy, and Rose in reference 32, there is reason to expect that a realistic outer flow solution with shock waves may be obtained by the use of a technique such as the rotational inviscid method of characteristics. The technique should be able to handle a curved oblique shock of variable strength in the outer flow and at the same time account for its reflection from the boundary at which the inner and outer flows are joined.

The applicability of the free-interaction principle to turbulent boundary-layer, shock-wave interaction is limited. Consider the upstream pressure fields including possible separation pressure fields induced by various downstream means, such as an incident shock or a forward-facing step. If for given initial conditions (Mach number, Reynolds number, and temperature ratio) at the beginning of interaction, the induced pressure distribution is independent of the means of inducing it, free interaction is said to exist. Chapman, Kuehn, and Larson, reference 33, point out that free-interaction for turbulent layers is valid up to separation or slightly downstream in contrast to laminar layers for which free interaction appears valid well downstream of separation. Thus, even though the incident shock causes separation of a turbulent boundary layer, we might expect a free-interaction principle to be valid up to the separation point but not beyond. The actual principle governing free interaction for turbulent boundary layers need not necessarily be the same as that for laminar boundary layers.

Insight into the plausibility of the ideal boundary-layer model for turbulent boundary-layer, shock-wave interaction has been obtained by applying the present computer program to the case of a shock wave incident on a flat plate. Consider the case covered by figures 14 to 17 for which the oblique shock wave is generated by a 5° wedge and is incident on a turbulent boundary layer on a flat plate at an edge Mach number of 6.55. The experimental wall pressure distribution has been imposed on the boundary layer as if the pressure were uniform across the layer and the detailed flow field calculated. Figure 36 shows the shapes of an outer-edge streamline and of the δ^* line. The experimental pressure rise begins very sharply at $x = 1.88$ ft as shown in figure 14.

The slope of the δ^* line is shown in figure 37 as a function of x as obtained from the computer program. The δ^* line changes its slope from a maximum to a minimum in about one boundary-layer thickness. In the ideal boundary-layer model, we assume that the change in $d\delta^*/dx$ occurs discontinuously just as in the model for laminar boundary-layer, shock-wave interaction (ref. 34). The dotted line in the figure corresponds to such a discontinuity with the total area under the $d\delta^*/dx$ curve unchanged so that the final δ^* is unchanged.

A free-interaction pressure law is now postulated based on the calculated flow model. At the point of shock impingement the static pressure and Mach number must be continuous at the edge of the layer even though the δ^* line changes discontinuously in slope. Let us start at point B, figure 37, with the same static pressure and Mach number as at point A and apply shock-expansion theory to calculate a pressure distribution based on $d\delta^*/dx$. If this is done, the pressure distribution shown in figure 38 is obtained. The calculated distribution is seen to be in fair agreement with the experimental pressure distribution. One difference is a parallel shift near the beginning of interaction because no account was taken in the free-interaction model of the small extent of upstream influence of the oblique shock. Application of shock-expansion theory to the outer-edge streamline yields a compression ratio of the order of 10 rather than 4. This result tends to indicate that the use of the δ^* line in the free-interaction pressure law is to be preferred to the use of a streamline near the edge of the boundary layer.

CONCLUDING REMARKS

A new technique has been developed for calculating the characteristics of turbulent boundary layers under the action of prescribed pressure gradients on two-dimensional or axisymmetric bodies. The technique is a new application of the method of integral relations previously used successfully to predict the characteristics of separated laminar boundary layers. An eddy-viscosity model has been developed for use in the turbulent boundary-layer equations, and a computer program has been written to solve the equations with prescribed pressure gradients for flows from low speeds to hypersonic speeds.

A number of methods of obtaining initial conditions are described. Difficulty was experienced in obtaining good initial conditions in some cases, and the best means for any particular case depends on the initial data available as well as the configuration.

The computer program has been applied to a number of two-dimensional cases for which data are available. From comparisons with low-speed data it was found that generally good agreement was obtained in favorable pressure gradients. In unfavorable pressure gradients the calculated quantities departed from the measured quantities ahead of separation. It is known that the analytical velocity-gradient representation used in the program is not valid at separation, but the lack of agreement upstream of separation is not necessarily all due to this factor. For instance, the validity of the eddy-viscosity model at separation has not been proven. Also, in at least one of the two low-speed cases, the two dimensionality of the flow approaching separation is open to question. No separated layers were studied at high speeds.

A number of comparisons were made for high-speed boundary layers on flat and curved two-dimensional plates. For the flat plate at hypersonic speeds good agreement is obtained between the theoretical and experimental displacement thicknesses, momentum thicknesses, and velocity profiles. For the curved plates, generally good agreement was obtained for displacement and momentum thickness at $M_\infty = 10.4$, but poor agreement was obtained at $M_\infty = 7.4$. The results for the curved plate are clouded by difficulty in obtaining accurate initial conditions due to the paucity of initial data and by nonisentropic flow at the edge of the boundary layer. The desirability of including nonisentropic edge effects in an enhanced computer program is apparent.

In the case of incident oblique shocks interacting with turbulent boundary layers on flat plates, the pressure gradients are very large and the pressure rise occurs typically in 10 boundary-layer thicknesses. Also, the shock wave penetrates so far into the boundary layer that the usual assumption of constant pressure across the boundary layer is violated. In the application of the computer program to hypersonic, boundary-layer, shock-wave interaction, it is expected that quantities sufficiently far downstream of interaction will be well predicted. However, in the interaction region accurate predictions would not be expected. The program has shown good to poor results in predicting these downstream quantities for the two cases investigated. The interpretation of the comparisons has been clouded by questions concerning the accuracy of the experimental results. More comparisons with data of known accuracy are required.

The computer program has been applied to only one axisymmetric configuration consisting of a hollow circular cylinder culminating in a compression flare. The compression flare had sufficiently large curvature that significant pressure differences occurred between the wall and the outer edge of the boundary layer. Applying the computer program to the configuration yielded good agreement between predicted and measured heat-transfer rates and displacement thicknesses provided corrections were applied to the data to account for the normal pressure gradients. Fair agreement was obtained between experimental Mach number profiles and the predicted profiles by adjusting the predicted profiles to account for normal pressure gradients. The adjustment for the Mach number profile also yields adjustments for the displacement and momentum thicknesses. After adjustment fair agreement was obtained between experiment and theory for displacement thickness and momentum thickness.

A study was made of an idealized boundary-layer model for shock-wave, boundary-layer interaction by calculating the detailed flow field of such an interaction using the computer program. It was found that the streamlines undergo a nearly discontinuous change in slope where the pressure rises due to shock impingement. It was also found for the one case studied that application of the shock-expansion theory to the δ^* line yielded a good prediction of the prescribed pressure distribution, whereas the same theory applied to a streamline at the outer edge of the flow did not. These findings suggest that a free-interaction model successfully used to predict laminar boundary-layer, shock-wave, interaction may be

adapted to the turbulent case for pressure ratios up to those for incipient separation. The idealized model will not predict the shock structure resulting from penetration of the oblique shock into the boundary layer.

A computer program has been written using an analytical velocity-gradient representation which is mathematically capable of representing a separated velocity profile. A run made with this program for a low-speed boundary layer on a flat plate gave valid skin-friction results out to a Reynolds number of about 10^8. The program is much slower than the main program used herein, but it represents the first step toward a program which will go to separation.

Nielsen Engineering & Research, Inc.
Palo Alto, Calif.
July 1968

APPENDIX A

EDDY-VISCOSITY MODEL

The eddy-viscosity distribution for compressible nonadiabatic turbulent boundary layers is basically an incompressible distribution transformed to the compressible plane. In the following development the incompressible model will be derived first and will then be transformed.

Incompressible Eddy-Viscosity Model

The incompressible model used is well known. It consists of an inner layer, where the shear is assumed constant, and an outer layer where the eddy viscosity is assumed constant. Within the inner layer the eddy-viscosity parameter β is obtained from an assumed velocity profile with the help of the following relationship:

$$\tilde{\beta} = \frac{\tilde{\tau}_w}{\tilde{\mu}(\partial\tilde{u}/\partial\tilde{y})} \tag{A-1}$$

(Tildes will be used to indicate quantities for a constant density turbulent boundary layer.) This equation becomes nondimensional in terms of standard velocity correlation coordinates. Velocity correlations are usually made on the basis of the friction velocity, which is defined as

$$\tilde{u}_\tau = \sqrt{\frac{\tilde{\tau}_w}{\tilde{\rho}}} = u_e\sqrt{\frac{\tilde{c}_f}{2}} \tag{A-2}$$

and a Reynolds number $\tilde{\zeta}$ based on distance from the wall

$$\tilde{\zeta} = \frac{\tilde{y}\tilde{u}_\tau}{\tilde{\nu}} \tag{A-3}$$

In the inner layer the velocity ratio $\tilde{u}/\tilde{u}_\tau$ is basically a function only of the Reynolds number $\tilde{\zeta}$. With these standard definitions the equation for the eddy-viscosity parameter can be rearranged as follows:

$$\tilde{\beta} = \frac{\tilde{\tau}_w/\tilde{\rho}}{\tilde{\mu}\,\dfrac{\partial(\tilde{u}/\tilde{u}_\tau)}{\partial(\tilde{y}\tilde{u}_\tau/\tilde{\nu})}}\;\frac{\tilde{\rho}}{\tilde{u}_\tau^2/\tilde{\nu}} = \frac{\partial\tilde{\zeta}}{\partial(\tilde{u}/\tilde{u}_\tau)} \tag{A-4}$$

With the assumption of constant wall shear within the inner layer it is seen that only a velocity profile is required to evaluate $\tilde{\beta}$. For the present eddy-viscosity model a laminar sublayer is used together with a law-of-the-wall region. The law of the wall, given by a logarithmic equation, is based on Prandtl's mixing length theory and the assumption that shear is constant across the layer at the wall value, reference 35. The velocity profile obtained from these assumptions is:

Laminar sublayer:

$$\frac{\tilde{u}}{\tilde{u}_\tau} = \tilde{\zeta} \qquad 0 \le \tilde{\zeta} \le \tilde{\zeta}_f \tag{A-5}$$

Law-of-the-wall region:

$$\frac{\tilde{u}}{\tilde{u}_\tau} = A \ln b\tilde{\zeta} \qquad \tilde{\zeta}_f \le \tilde{\zeta} \le \tilde{\zeta}_m \tag{A-6}$$

where

$\tilde{\zeta}_f$ = value of $\tilde{\zeta}$ at outer edge of laminar sublayer = 10.6

A = 2.43

b = 7.5

$\tilde{\zeta}_m$ = value of $\tilde{\zeta}$ at outer edge of inner layer

The numerical values for ζ_f, A, and b are those of Clauser, reference 17. Using equation (A-4) along with equations (A-5) and (A-6) gives the following equations for the eddy-viscosity distribution within the inner layer

$$\left.\begin{aligned} \tilde{\beta} &= 1 \\ & \qquad 0 \le \tilde{\zeta} < 10.6 \\ & \qquad 0 \le \tilde{u}/\tilde{u}_\tau \le 10.6 \end{aligned}\right\} \tag{A-7}$$

$$\left.\begin{aligned} \tilde{\beta} &= \frac{\tilde{\zeta}}{A} & & 10.6 \le \tilde{\zeta} \le \tilde{\zeta}_m \\ \text{or} & & & \\ \beta &= \frac{1}{Ab}\, e^{(1/A)(\tilde{u}/\tilde{u}_\tau)} & & 10.6 \le \tilde{u}/\tilde{u}_\tau \le \left(\tilde{u}/\tilde{u}_\tau\right)_m \end{aligned}\right\} \tag{A-8}$$

The distribution for the inner layer is shown in figure 1. It will be noted that the foregoing equations provide a distinct discontinuity in the eddy-viscosity distribution at $\tilde{u}/\tilde{u}_\tau$ of 10.6. In order to prevent

this discontinuity from causing numerical difficulties in the evaluation of the eddy-viscosity integrals, the fairing between the laminar sublayer and the law-of-the-wall region, shown in figure 1, was utilized. This fairing was selected arbitrarily, and is given by

$$\tilde{\beta} = e^{K\left[(\tilde{u}/\tilde{u}_\tau)-7.95\right]} \qquad 7.95 \leq \tilde{u}/\tilde{u}_\tau \leq 13.95 \tag{A-9}$$

where

$$K = \frac{1}{5.3}\left[\frac{13.25}{2.43} - \ln(18.225)\right]$$

$$= 0.48111 \tag{A-10}$$

The final distribution for the inner layer is composed of three sections; a laminar sublayer part, a fairing, and a law-of-the-wall part.

For the outer layer or wake region only one section will be required. Here the eddy viscosity for an incompressible constant density turbulent boundary layer is a constant as postulated by Clauser, reference 17. The expression used for calculating the value of $\tilde{\beta}$ for the wake is

$$\tilde{\beta} = 0.018\ \tilde{R}_{\delta*} \tag{A-11}$$

The boundary between the inner and outer layers is obtained by matching the value of $\tilde{\beta}$ obtained from the inner layer to the value of $\tilde{\beta}$ given by Clauser's relation. When the match point falls on the law of the wall, the relation for determining the value of $\tilde{u}/\tilde{u}_\tau$ at this point is

$$\frac{\tilde{u}}{\tilde{u}_\tau} = 2.43\ \ln(0.32805\ \tilde{R}_{\delta*}) \tag{A-12}$$

Compressible Eddy-Viscosity Model; Inner Layer

The compressible eddy-viscosity model is obtained using the Baronti-Libby transformation for the inner layer and using density scaling in the outer layer. Baronti and Libby (ref. 14) used Coles' transformation (ref. 15) coupled with Donaldson's hypothesis (ref. 16) to collapse compressible velocity profiles onto the incompressible law of the wall. The agreement between the incompressible law of the wall and compressible velocity profiles transformed to incompressible profiles is good everywhere

except in the wake. This type of agreement leads to a compressible, non-adiabatic eddy-viscosity model based on two layers. The model from the wall out to the wake is a transformed incompressible eddy-viscosity model. In the wake region Clauser's constant eddy viscosity is scaled for local density. The eddy-viscosity model for the inner layer is constructed as follows.

Given in the compressible plane the two basic boundary-layer properties, skin friction and displacement thickness, along with all flow conditions at the boundary-layer edge, it is required to construct an eddy-viscosity distribution. The first step in determining the parameters specifying the equivalent incompressible eddy-viscosity distribution is to establish the transformations to be employed. Consider the Coles' transformation:

$$\frac{d\tilde{x}}{dx} = \tilde{\xi}(x) \tag{A-13}$$

$$\frac{d\tilde{y}}{dy} = \tilde{\eta}(x)\ \frac{\rho}{\tilde{\rho}} \tag{A-14}$$

and a streamline stretching factor $\sigma(x)$, defined by

$$\tilde{\psi}(\tilde{x},\tilde{y}) = \sigma(x)\psi(x,y) \tag{A-15}$$

The stream functions are defined in the usual way

$$\rho u = \frac{\partial \psi}{\partial y} \qquad \rho v = -\frac{\partial \psi}{\partial x} \tag{A-16}$$

$$\tilde{\rho}\tilde{u} = \frac{\partial \tilde{\psi}}{\partial \tilde{y}} \qquad \tilde{\rho}\tilde{v} = -\frac{\partial \tilde{\psi}}{\partial \tilde{x}} \tag{A-17}$$

Under these transformations it can be shown that at corresponding points

$$\frac{u}{u_e} = \frac{\tilde{u}}{\tilde{u}_e} \qquad u = \frac{\tilde{\eta}\tilde{u}}{\sigma} \tag{A-18}$$

To establish the parameters for the equivalent incompressible model, consider the wall shears

$$\tilde{\tau}_w = \tilde{\mu}\left(\frac{\partial \tilde{u}}{\partial \tilde{y}}\right)_w \qquad \tau_w = \mu_w\left(\frac{\partial u}{\partial y}\right)_w \tag{A-19}$$

and form their ratio

$$\frac{\tilde{\tau}_w}{\tau_w} = \frac{\tilde{\rho}\tilde{\mu}}{\rho_w \mu_w} \frac{\sigma}{\eta^2} \tag{A-20}$$

From equation (A-20) we obtain the first basic equation used in finding the equivalent incompressible model

$$\tilde{c}_f = \frac{\rho_e \mu_e}{\rho_w \mu_w} \frac{\tilde{\mu}}{\sigma \mu_e} c_f \tag{A-21}$$

The starting point for obtaining a second equation is Donaldson's hypothesis, which states that the Reynolds number for the laminar sublayer edge is preserved during the transformation.

$$\frac{\rho_f u_f y_f}{\mu_f} = \frac{\tilde{\rho}\tilde{u}_f \tilde{y}_f}{\tilde{\mu}} \tag{A-22}$$

After rearrangement and use of the y transformation to obtain the stretched coordinate, equation (A-22) yields

$$\frac{\mu_e \sigma}{\tilde{\mu}} = \left(\frac{\rho_f}{\rho_e}\right)\left(\frac{\mu_e}{\mu_f}\right) \frac{1}{\tilde{\zeta}_f} \int_0^{\tilde{\zeta}_f} \left(\frac{\rho_e}{\rho}\right) d\tilde{\zeta} \tag{A-23}$$

Using the Crocco relationship and the constancy of pressure across the boundary layer yields the following relationship for density

$$\frac{\rho_e}{\rho} = \frac{T}{T_e} = \frac{T_w}{T_e} + \left(\frac{T_{t_o}}{T_e} - \frac{T_w}{T_e}\right) \frac{u}{u_e} - \left(\frac{T_{t_o}}{T_e} - 1\right)\left(\frac{u}{u_e}\right)^2 \tag{A-24}$$

For the laminar sublayer equations (A-2) and (A-18) give

$$\frac{u}{u_e} = \frac{\tilde{u}}{\tilde{u}_e} = \frac{\tilde{u}}{\tilde{u}_\tau} \left(\frac{\tilde{c}_f}{2}\right)^{1/2} = \tilde{\zeta}\left(\frac{\tilde{c}_f}{2}\right)^{1/2} \tag{A-25}$$

Integration of equation (A-23) with the help of equations (A-24) and (A-25) yields the desired second equation.

$$\frac{\mu_e \sigma}{\tilde{\mu}} = \left(\frac{\rho_f}{\rho_e}\right)\left(\frac{\mu_e}{\mu_f}\right)\left[\frac{T_w}{T_e} + \left(\frac{T_{t_o}}{T_e} - \frac{T_w}{T_e}\right)\left(\frac{\tilde{c}_f}{2}\right)^{1/2} \frac{\tilde{\zeta}_f}{2} - \left(\frac{T_{t_o}}{T_e} - 1\right)\left(\frac{\tilde{c}_f}{2}\right) \frac{\tilde{\zeta}_f^2}{3}\right] \tag{A-26}$$

Since $\tilde{\zeta}_f$ is just a number equal to 10.6, the parameter $\mu_e \sigma/\tilde{\mu}$ and the incompressible skin-friction coefficient can be obtained from equations (A-21 and (A-26) by iteration. With these quantities, the incompressible eddy-viscosity $\tilde{\beta}$ for the inner layer as a function of u/u_e can be determined from equations (A-7) and (A-8) with the help of equation (A-25).

It remains only to determine the relationship between $\tilde{\beta}$ and the compressible eddy-viscosity parameter, β. In general

$$\beta = \frac{\tau}{\mu \frac{\partial u}{\partial y}} \tag{A-27}$$

For the inner zone it is assumed that the shear is constant at the wall value so that

$$\beta = \frac{\tau_w}{\mu \frac{\partial u}{\partial y}} \tag{A-28}$$

Applying the transformation to this equation yields the desired relationship between β and $\tilde{\beta}$

$$\beta = \left(\frac{\rho_w \mu_w}{\rho \mu}\right) \tilde{\beta} \tag{A-29}$$

In accordance with the assumption of the boundary-layer analysis $\rho\mu$ is assumed constant across the boundary layer so that

$$\beta = \tilde{\beta} \tag{A-30}$$

This relation completes the information required to determine the compressible eddy-viscosity distribution across the inner layer.

Compressible Eddy-Viscosity Model; Outer Layer

The eddy-viscosity distribution for the outer layer will now be developed, but first the boundary between the inner and outer layers will be determined. To aid in obtaining the point of the join, consider first the following definitions

$$\left.\begin{aligned} \tilde{\delta}^* &= \int_0^{\tilde{\delta}} \left(1 - \frac{\tilde{u}}{\tilde{u}_e}\right) d\tilde{y} & \delta^* &= \int_0^{\delta} \left(1 - \frac{\rho u}{\rho_e u_e}\right) dy \\ \tilde{\theta} &= \int_0^{\tilde{\delta}} \frac{\tilde{u}}{\tilde{u}_e}\left(1 - \frac{\tilde{u}}{\tilde{u}_e}\right) dy & \theta &= \int_0^{\delta} \frac{\rho u}{\rho_e u_e}\left(1 - \frac{u}{u_e}\right) dy \end{aligned}\right\} \quad \text{(A-31)}$$

If the quantity $\tilde{R}_{\delta^*}$ can be determined in terms of compressible boundary-layer parameters, then equation (A-11) can be used to determine the value of $\beta = \tilde{\beta}$ at the join. The value of $\tilde{R}_{\delta^*}$ can be approximately determined by applying the Baronti-Libby transformation across the entire layer. The relationship obtained by this means is

$$\tilde{R}_{\delta^*} = \frac{T_e}{T_w}\left(\frac{\mu_e \sigma}{\tilde{\mu}}\right)\left(R_{\delta^*} - m_e R_\theta\right) \quad \text{(A-32)}$$

where

$$\left.\begin{aligned} \tilde{R}_{\delta^*} &= \frac{\tilde{\rho}\tilde{u}_e\tilde{\delta}^*}{\tilde{\mu}} \\ R_{\delta^*} &= \frac{\rho_e u_e \delta^*}{\mu_e} \\ R_\theta &= \frac{\rho_e u_e \theta}{\mu_e} \\ m_e &= \frac{\gamma - 1}{2} M_e^2 \end{aligned}\right\} \quad \text{(A-33)}$$

The value of the eddy-viscosity parameter at the join is

$$\beta_m = \tilde{\beta} = 0.018\ \tilde{R}_{\delta*} = 0.018\ \frac{T_e}{T_w}\left(\frac{\mu_e \sigma}{\tilde{\mu}}\right)(R_{\delta*} - m_e R_\theta) \tag{A-34}$$

In developing equation (A-32) application of the transformations across the entire layer was made only in integral quantities defined by equation (A-31) to obtain the following relationship

$$\tilde{\delta}* = \frac{T_e}{T_w}\ \frac{\rho_e \tilde{\eta}}{\tilde{\rho}}\ (\delta* - m_e \theta) \tag{A-35}$$

It is believed that use of the Baronti-Libby transformation to obtain the velocity profile for the entire boundary layer is probably warranted in this case for two reasons: (1) the principal contributions to the integrals will come from the inner layer, and (2) the velocity relationship established by the transforms is valid out to the join and at the boundary-layer edge, that is,

$$\frac{u}{u_e} = \frac{\tilde{u}}{\tilde{u}_e} \tag{A-36}$$

For the limiting case of zero Mach number and adiabatic walls, the incompressible results are obtained.

While the eddy-viscosity parameter $\tilde{\beta}$ is constant across an incompressible wake according to equation (A-11), it is variable across a compressible wake because the density and molecular viscosity are not constant. Consider the definition of the eddy-viscosity parameter

$$\beta = 1 - \frac{\overline{\rho v_u' u_u'}}{\mu(\partial u/\partial y)} \tag{A-37}$$

where in this expression $\overline{u_u' v_u'}$ is the time average of the product of the turbulent components of the u and v velocities. The other symbols used represent time-averaged quantities. In the wake region the turbulent fluctuations dominate and, therefore,

$$\beta \cong \frac{\overline{\rho u_u' v_u'}}{\mu(\partial u/\partial y)} \tag{A-38}$$

In the wake the eddy-viscosity parameter varies directly as density and, inversely, as viscosity. The earlier assumption that $\rho\mu$ is constant leads to the result that β must vary as density squared. Assuming that the value of β_m at the join is correct as given by equation (A-34), the value of β in the wake becomes

$$\beta = \beta_m \left(\frac{\rho}{\rho_m} \right)^2 \qquad \text{(A-39)}$$

APPENDIX B

ANALYTICAL EXPRESSIONS FOR AXISYMMETRIC COMPRESSION SURFACE SHAPE AND PRESSURE DISTRIBUTION

To obtain an analytical expression for the shape of the axisymmetric compression surface of reference 30, the values of ϕ in that reference were converted to slopes by

$$\frac{dr}{dx_a} = \tan \phi \tag{B-1}$$

and the slopes were fitted for various segments of the flare with polynomials of the form

$$\frac{dr}{dx_a} = \sum_{n=1}^{4} \alpha_n x_a^{(n-1)} \tag{B-2}$$

The coefficients were determined by requiring continuity of dr/dx_a and d^2r/dx_a^2 at the segment boundaries. For the purpose of describing the shape, equation (B-2) was integrated and the condition of continuity of r was imposed. The axial distance was expressed in feet measured from the beginning of the cylinder with 2.433 feet corresponding to the cylinder-flare junction. In terms of this axial distance coordinate, x_a', the flare shape is given by

$2.433' \leq x_a' \leq 2.450' \qquad 0 \leq x_a \leq 0.2"$

$$r = -10944.853 + 17882.088x_a' - 10955.539x_a'^2 + 2982.9787x_a'^3 - 304.56572x_a'^4 \tag{B-3}$$

$2.450' \leq x_a' \leq 2.68333' \qquad 0.2" \leq x_a \leq 3.0"$

$$r = 4.1741342 - 5.0248867x_a' + 2.5800906x_a'^2 - 0.6796182x_a'^3 + 0.078720188x_a'^4 \tag{B-4}$$

$2.68333' \leq x_a' \leq 2.85' \qquad 3.0" \leq x_a \leq 5.0"$

$$r = 374.23568 - 552.88734x_a' + 306.72432x_a'^2 - 75.718106x_a'^3 + 7.020943x_a'^4 \qquad \text{(B-5)}$$

$2.85' \leq x_a' \leq 2.9333' \qquad 5.0" \leq x_a \leq 6.0"$

$$r = 3244.3716 - 4561.6647x_a' + 2406.3524x_a'^2 - 564.46037x_a'^3 + 49.682652x_a'^4 \qquad \text{(B-6)}$$

Another input into the computer program is the pressure distribution. The pressure distribution existing at the wall was used rather than that acting at the outer edge of the boundary layer. The polynomials describing the wall pressure distribution are as follows:

$0 \leq x_a \leq 0.8"$

$$\frac{p_w}{p_{w_o}} = 3399.0535 - 3992.2842x_a' + 1559.6654x_a'^2 - 202.55691x_a'^3 \qquad \text{(B-7)}$$

$0.8" \leq x_a \leq 2.0"$

$$\frac{p_w}{p_{w_o}} = -2876.0597 + 3481.6263x_a' - 1407.4084x_a'^2 + 190.0542x_a'^3 \qquad \text{(B-8)}$$

$2.0" \leq x_a \leq 4.0"$

$$\frac{p_w}{p_{w_o}} = -5730.5403 + 6670.1398x_a' - 2593.3295x_a'^2 + 336.91196x_a'^3 \qquad \text{(B-9)}$$

$4.0" \leq x_a \leq 5.0"$

$$\frac{p_w}{p_{w_o}} = -34461.726 + 38775.59x_a' - 14541.502x_a'^2 + 1817.872x_a'^3 \qquad \text{(B-10)}$$

$5.0" \leq x_a \leq 6.0"$

$$\frac{p_w}{p_{w_o}} = 207461.82 - 209345.92x_a' + 70225.728x_a'^2 - 7828.2407x_a'^3 \qquad \text{(B-11)}$$

REFERENCES

1. Head, M. R.: Entrainment in the Turbulent Boundary Layer. ARC R&M 3152, 1960.

2. Maskell, B. A.: Approximate Calculation of the Turbulent Boundary Layer in Two-Dimensional Incompressible Flow. Great Britain, R.A.E. Rep. Aero. 2443, Nov. 1951.

3. Reshotko, E. and Tucker, M.: Effect of a Discontinuity on Turbulent Boundary-Layer-Thickness Parameters with Application to Shock-Induced Separation. NACA TN 3454, May 1955.

4. Rubert, K. F. and Persh, J.: A Procedure for Calculating the Development of Turbulent Boundary Layers under the Influence of Adverse Pressure Gradients. NACA TN 2478, Sept. 1951.

5. Sasman, P. K. and Cresci, R. J.: Compressible Turbulent Boundary Layer with Pressure Gradient and Heat Transfer, AIAA Jour., vol. 4, no. 1, pp. 19-25, 1966.

6. Spence, D. A.: The Development of Turbulent Boundary Layers. Jour. of the Aeronautical Sci., vol. 23, no. 1, Jan. 1956.

7. Truckenbrodt, E.: A Method of Quadrature for Calculation of the Laminar and Turbulent Boundary Layer in Case of Plane and Rotationally Symmetrical Flow. NACA TM 1379, May 1955.

8. Von Doenhoff, A. E. and Tetervin, N.: Determination of General Relations for the Behavior of Turbulent Boundary Layers. NACA Rep. No. 772, 1943.

9. Smith, A. M. O. and Cebeci, T.: Numerical Solution of the Turbulent-Boundary-Layer Equations. Douglas Aircraft Div., Rep. No. DAC 33735, May 29, 1967.

10. Nielsen, J. N., Lynes, L. L., and Goodwin, F. K.: Calculation of Laminar Separation with Free Interaction by the Method of Integral Relations. Part I - Two-Dimensional Supersonic Adiabatic Flows. Air Force Flight Dynamics Lab. Rep. AFFDL-TR-65-107, June 1965.

11. Nielsen, J. N., Lynes, L. L., and Goodwin, F. K.: Calculation of Laminar Separation with Free Interaction by the Method of Integral Relations. Part II - Two-Dimensional Supersonic Nonadiabatic Flow and Axisymmetric Supersonic Adiabatic and Nonadiabatic Flows. Air Force Flight Dynamics Lab. Rep. AFFDL-TR-65-107, Jan. 1966.

12. Nielsen, J. N., Lynes, L. L., and Goodwin, F. K.: Theory of Laminar Separated Flows on Flared Surfaces Including Supersonic Flow with Heating and Cooling. AGARD Conference Proceedings, no. 4, part 1, proceedings of AGARD Fluid Dynamics Panel held in Rhode-Saint-Genise, Belgium, 10-13 May 1966, pp. 37-68.

13. Dorodnitsyn, A. A.: General Method of Integral Relations and its Application to Boundary Layer Theory. Advances in Aero. Sci., vol. III, Macmillan, New York, 1960, pp. 207-219.

14. Baronti, P. O. and Libby, P. A.: Velocity Profiles in Turbulent Compressible Boundary Layers. AIAA Jour., vol. 4, no. 2, Feb. 1966, pp. 193-202.

15. Coles, D. E.: The Turbulent Boundary Layer in a Compressible Fluid. The Rand Corp., R-403-PR, Sept. 1962.

16. Donaldson, Coleman duP.: On the Form of the Turbulent Skin-Friction Law and its Extension to Compressible Flows. NACA TN 2692, May 1952.

17. Clauser, F. H.: The Turbulent Boundary Layer. Advances in Appl. Mech., vol. IV, Academic Press, Inc., 1956, pp. 1-52.

18. Spalding, D. B.: A Single Formula for the "Law of the Wall." Jour. of Appl. Mech., Sept. 1962, pp. 455-458.

19. Coles, D.: The Law of the Wake in the Turbulent Boundary Layer. Jour. of Fluid Mech., vol. 1, part 2, July 1956, pp. 191-226.

20. Sommer, S. C. and Short, B. J.: Free-Flight Measurements of Turbulent-Boundary-Layer Skin Friction in the Presence of Severe Aerodynamic Heating at Mach Numbers from 2.8 to 7.0. NACA TN 3391, Mar. 1955.

21. Kuhn, G. D., Lynes, L. L., and Nielsen, J. N.: Computer Program for Turbulent Boundary Layers on Nonadiabatic Two-Dimensional or Axisymmetric Bodies with Prescribed Pressure Distribution. Nielsen Engineering & Research, Inc., Tech. Rep. TR 7, July 1968.

22. The Vidya Staff: Effects of Supersonic and Hypersonic Aircraft Speed Upon Aerial Photography. Vidya Rep. No. 37, Jan. 1961.

23. Spalding, D. B. and Chi, S. W.: The Drag of a Compressible Turbulent Boundary Layer on a Smooth Flat Plate with and without Heat Transfer. Jour. Fluid Mech., vol. 18, part I, Jan. 1964, pp. 117-143.

24. Schubauer, G. B. and Klebanoff, P. S.: Investigation of Separation of the Turbulent Boundary Layer. NACA Rep. 1030, 1951.

25. Newman, B. G.: Some Contributions to the Study of the Turbulent Boundary Layer Near Separation. Commonwealth of Australia, Department of Supply, Aeronautical Research Consultative Committee, Rep. ACA-53, Mar. 1951.

26. Kutschenreuter, P. H., Jr., Brown, D. L., Hoelmer, W., et al.: Investigation of Hypersonic Inlet Shock-Wave Boundary Layer Interaction. Part II - Continuous Flow Test and Analyses. AFFDL TR 65-36, AD 636 981, Apr. 1966.

27. Pinckney, S. Z.: Data on Effects of Incident-Reflecting Shocks on the Turbulent Boundary Layer. NASA TM X-1221, Mar. 1966.

28. Hoydysh, W. G. and Zakkay, V.: An Experimental Investigation of Hypersonic Turbulent Boundary Layers in Adverse Pressure Gradient. Rep. No. F-67-5, New York Univ., School of Engr. and Sci., Aug. 1967.

29. McLafferty, G. H. and Barber, R. E.: The Effect of Adverse Pressure Gradients on the Characteristics of Turbulent Boundary Layers in Supersonic Streams. Jour. Aerospace Sci., vol. 29, no. 1, Jan. 1962, pp. 1-10.

30. Hoydysh, W. G. and Zakkay, V.: An Experimental Investigation of Hypersonic Turbulent Boundary Layers in Adverse Pressure Gradient. AIAA Paper No. 68-44, Sixth Aerospace Science Meeting, New York, N. Y., Jan. 22-24, 1968.

31. Milne-Thomson, L. M.: Theoretical Hydrodynamics. Second Ed., The MacMillan Co., 1950, p. 583.

32. Watson, E. C., Murphy, J. D., and Rose, W. C.: Shock-Wave, Boundary-Layer Interactions in Hypersonic Inlets. NASA Conference on Hypersonic Aircraft Technology, Ames Research Center, May 16-18, 1967. CONFIDENTIAL

33. Chapman, D. R., Kuehn, D. M., and Larson, H. K.: Investigation of Separated Flows in Supersonic and Subsonic Streams with Emphasis on the Effect of Transition. NACA TN 3869, Mar. 1957.

34. Goodwin, F. K., Nielsen, J. N., and Lynes, L. L.: Calculation of Laminar Boundary Layer—Shock Wave Interaction on Cooled Walls by the Method of Integral Relations. NEAR Rep. TR 2, July 1967.

35. Schlichting, H.: Boundary-Layer Theory. McGraw-Hill Book Co., Inc., Fourth Edition, 1960.

TABLE I

INITIAL CONDITIONS OBTAINED BY FITTING ZERO-PRESSURE-GRADIENT, INCOMPRESSIBLE, TURBULENT, VELOCITY PROFILES

(a) m = 1, n = 2

R_x	No root			Root			
	c_1	c_2	c_3	$\overline{c}$	c_1	c_2	c_3
10^4	2.1834	-3.1217	3.1702	0.4404	1.4489	-0.9421	1.6951
10^5	1.0944	-1.9771	3.7943	.2116	.5038	- .1600	1.8398
10^6	.5485	-1.2686	3.8569	.1046	.1772	.0961	1.5134
10^7	.2749	- .7925	3.5096	.0598	.0672	.1261	1.1661
10^8	.1378	- .4934	3.0471	.0375	.0267	.1000	.8762

(b) m = 1, n = 5

R_x	No root			Root			
	c_1	c_2	c_3	$\overline{c}$	c_1	c_2	c_3
10^4	2.1834	-1.9547	4.3483	0.3337	1.2613	-0.1125	2.3114
10^5	1.0944	- .9677	12.3504	.3544	.6520	- .0035	9.4340
10^6	.5485	- .5044	28.6241	.7777	.4832	- .2201	29.8697
10^7	.2749	- .2577	55.2333	1.2127	.3029	- .1900	67.8473
10^8	.1378	- .1314	98.8472	.5655	.1037	- .0273	88.5148

TABLE II

INITIAL CONDITIONS FOR A FLAT PLATE

(a) $M = 0$, $R_{\ell_o} = 10^6$

$\frac{T_w}{T_{t_e}}$	x	c_1	c_2	c_3	δ^* (ft$\times 10^3$)	θ (ft$\times 10^3$)	c_f ($\times 10^3$)
1.0	1.0	0.54	- 3.18	11.8	2.88	2.16	3.73
	10.0	.79	-12.5	75.6	19.74	15.13	2.53
0.6	1.0	.50	- 3.25	12.2	1.76	2.21	4.04
	10.0	.70	-12.5	81.0	12.87	16.43	2.85
0.2	1.0	.47	- 2.95	11.7	.58	2.18	4.26
	5.0	.57	- 8.40	48.6	2.51	9.64	3.51

(b) $M = 2$, $R_{\ell_o} = 2.5\times 10^6$

$\frac{T_w}{T_{t_e}}$	x	c_1	c_2	c_3	δ^* (ft$\times 10^3$)	θ (ft$\times 10^3$)	c_f ($\times 10^3$)
1.0	1.0	0.51	- 3.40	12.4	4.47	1.41	2.48
	10.0	.79	-12.90	77.0	30.5	9.71	1.60
0.6	1.0	.46	- 3.40	13.3	3.41	1.53	2.75
	10.0	.68	-12.90	85.0	24.2	10.94	1.86
0.2	1.0	.42	- 3.40	13.5	1.96	1.54	3.01
	10.0	.58	-12.90	94.5	15.7	12.42	2.20

TABLE II

CONTINUED

(c) $M = 4$, $R_{\ell_o} = 2.5 \times 10^6$

$\frac{T_w}{T_{t_e}}$	x	c_1	c_2	c_3	δ^* ($ft \times 10^3$)	θ ($ft \times 10^3$)	c_f ($\times 10^3$)
1.0	1.0	0.76	- 3.60	11.0	10.88	1.22	1.66
	10.0	1.21	-12.5	57.0	58.70	6.76	1.05
0.6	1.0	.69	- 3.48	11.2	8.29	1.26	1.83
	10.0	1.07	-12.5	61.0	47.67	7.35	1.18
0.2	1.0	.63	- 3.25	11.4	5.70	1.32	2.01
	10.0	.93	-12.5	67.0	35.45	8.25	1.36

(d) $M = 6$, $R_{\ell_o} = 2.5 \times 10^6$

$\frac{T_w}{T_{t_e}}$	x	c_1	c_2	c_3	δ^* ($ft \times 10^3$)	θ ($ft \times 10^3$)	c_f ($\times 10^3$)
1.0	1.0	1.00	- 3.70	9.9	20.64	1.10	1.26
	10.0	1.70	-12.45	46.0	93.39	5.19	.74
0.6	1.0	.91	- 3.55	9.8	15.31	1.09	1.39
	10.0	1.50	-12.30	48.0	74.71	5.47	.84
0.2	1.0	.87	- 3.56	10.0	10.47	1.11	1.45
	10.0	1.35	-12.10	52.0	57.01	6.10	.94

TABLE II

CONCLUDED

(e) $M = 8$, $R_{\ell_o} = 3.2 \times 10^6$

$\frac{T_w}{T_{t_e}}$	x	c_1	c_2	c_3	δ^* ($ft \times 10^3$)	θ ($ft \times 10^3$)	c_f ($\times 10^3$)
1.0	1.0	1.24	- 4.10	9.3	32.7	1.00	1.02
	10.0	2.13	-12.40	39.0	132.0	4.23	.59
0.6	1.0	1.11	- 3.68	8.4	22.4	.90	1.14
	10.0	1.94	-12.00	41.0	108.8	4.57	.65
0.2	1.0	1.12	- 3.80	9.8	18.5	1.10	1.13
	10.0	1.75	-12.00	44.0	81.9	4.98	.72

TABLE III

TABULATED PRESSURE DISTRIBUTIONS FOR COMPRESSION FLARE OF REFERENCE 28

ϕ (degs)	x (ins.)	$\frac{p_w}{p_{t_\infty}}$ ($\times 10^3$)	$\frac{p_e}{p_{t_\infty}}$ ($\times 10^3$)	$\frac{p_w}{p_{e_o}}$	$\frac{p_e}{p_{e_o}}$	$\frac{p_{se}}{p_{e_o}}$
0	0	0.80	0.80	1.00	1.00	1.00
2.5	0.67	1.0	.80	1.25	1.00	1.41
5	1.27	1.40	.83	1.80	1.04	1.96
7.5	1.86	1.85	.95	2.31	1.19	2.68
10	2.43	2.62	1.37	3.28	1.71	3.63
15	3.42	4.50	2.37	5.63	2.96	6.25
20	4.27	7.70	3.90	9.63	4.88	10.38
25	4.88	12.6	7.3	15.8	9.13	16.42
30	5.31	18.8	9.1	23.5	11.4	25.4
32.5	5.49	22.9	10.4	28.6	13.0	30.8
35	5.62	27.4	12.0	34.3	15.0	37.4
37.5	5.76	32.4	11.6	40.5	14.5	44.9

TABLE IV

MACH NUMBER AND TOTAL PRESSURE DISTRIBUTIONS
AT EDGE OF BOUNDARY LAYER FOR FLARE
OF REFERENCE 28

ϕ (degs)	$\frac{p_e}{p_{t_\infty}}$ ($\times 10^3$)	$\frac{p_{t_2}}{p_{t_\infty}}$ ($\times 10^3$)	M_e	$\frac{p_{t_1}}{p_{t_\infty}}$
0	0.80	34	5.78	0.98
2.5	.80	34	5.78	.98
5	.83	35.5	5.73	.99
7.5	.95	41	5.75	1.16
10	1.37	53	5.45	1.20
15	2.37	76	4.95	1.18
20	3.90	106	4.55	1.21
25	7.30	148	3.92	1.00
30	9.10	156	3.60	.80
32.5	10.4	164	3.45	.74
35	12.0	188	3.43	.83
37.5	11.6	194	3.55	.95

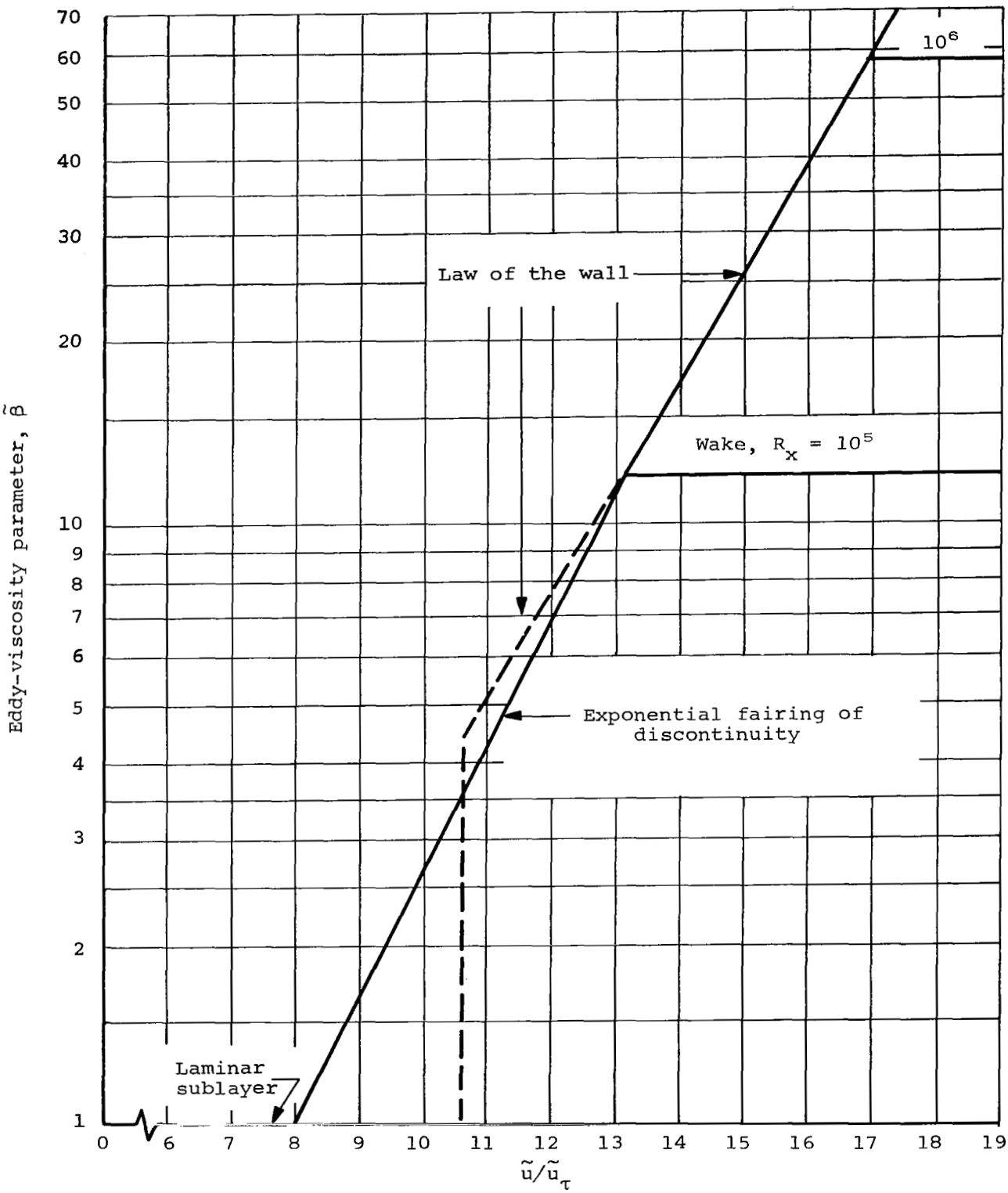

Figure 1.- Eddy-viscosity parameter distributions for turbulent incompressible boundary layers on flat plates.

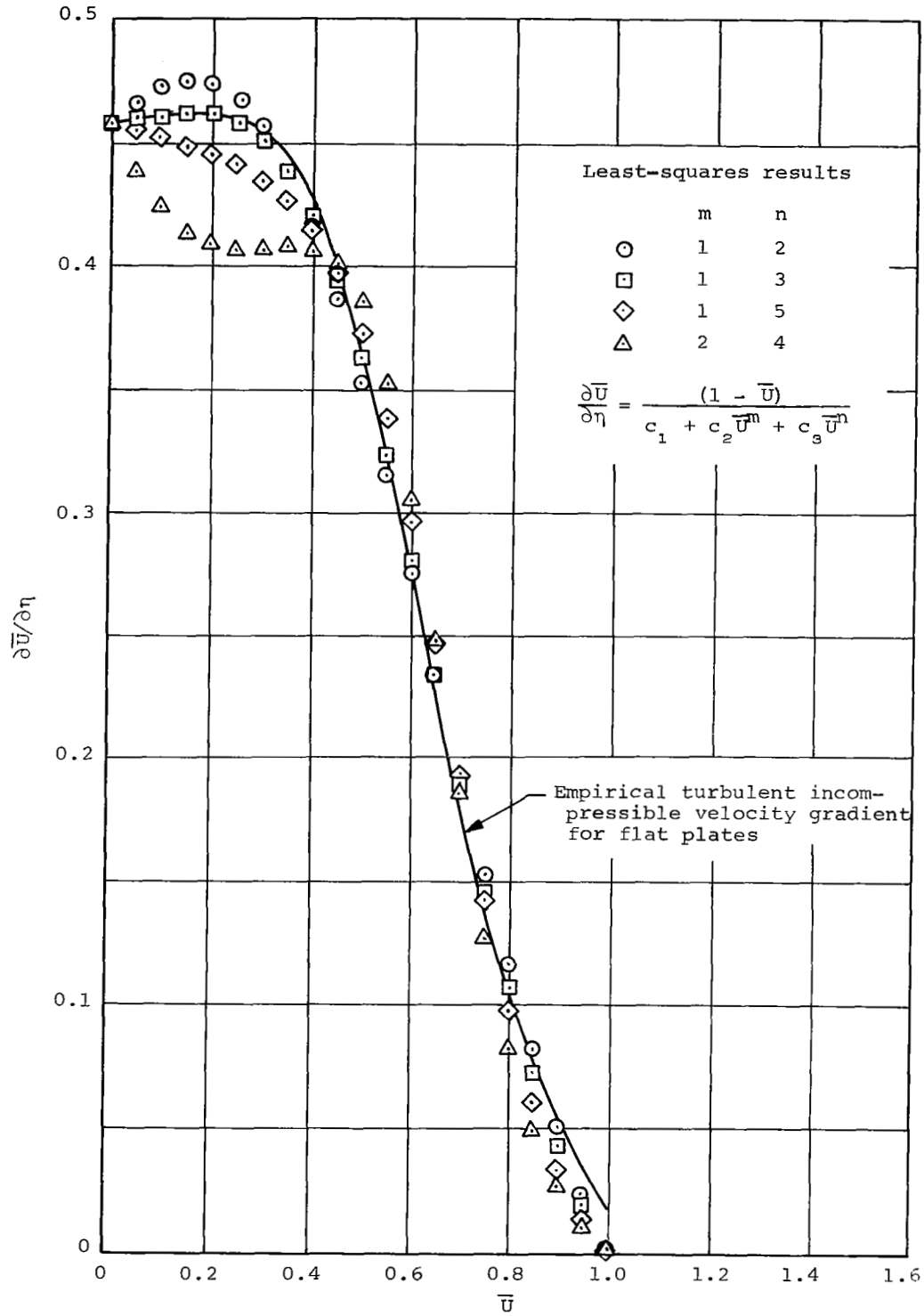

(a) $R_x = 10^4$

Figure 2.- Comparison of no-root velocity gradients with empirical incompressible turbulent gradients as fitted by the least-squares method.

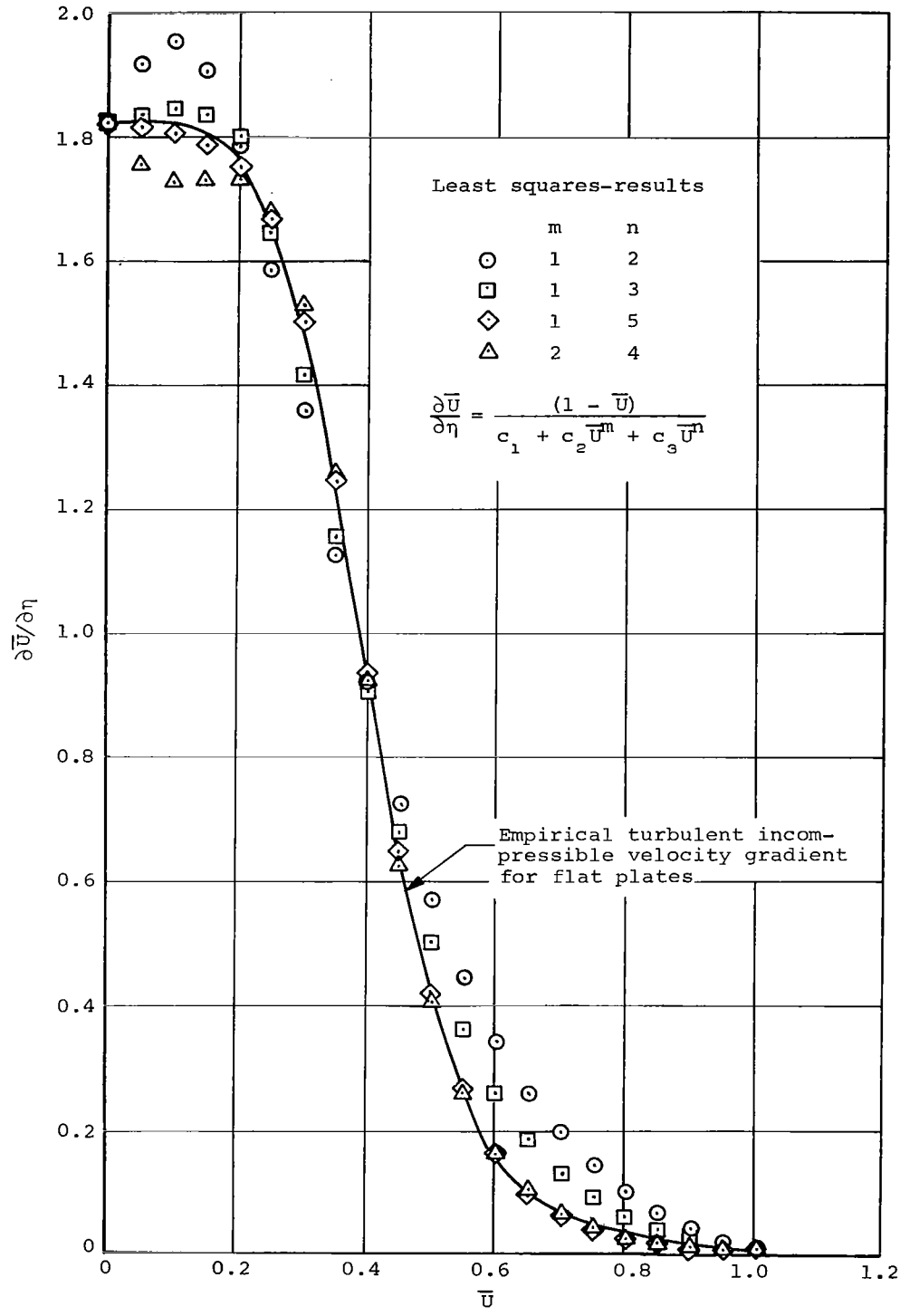

(b) $R_x = 10^6$.

Figure 2.- Continued.

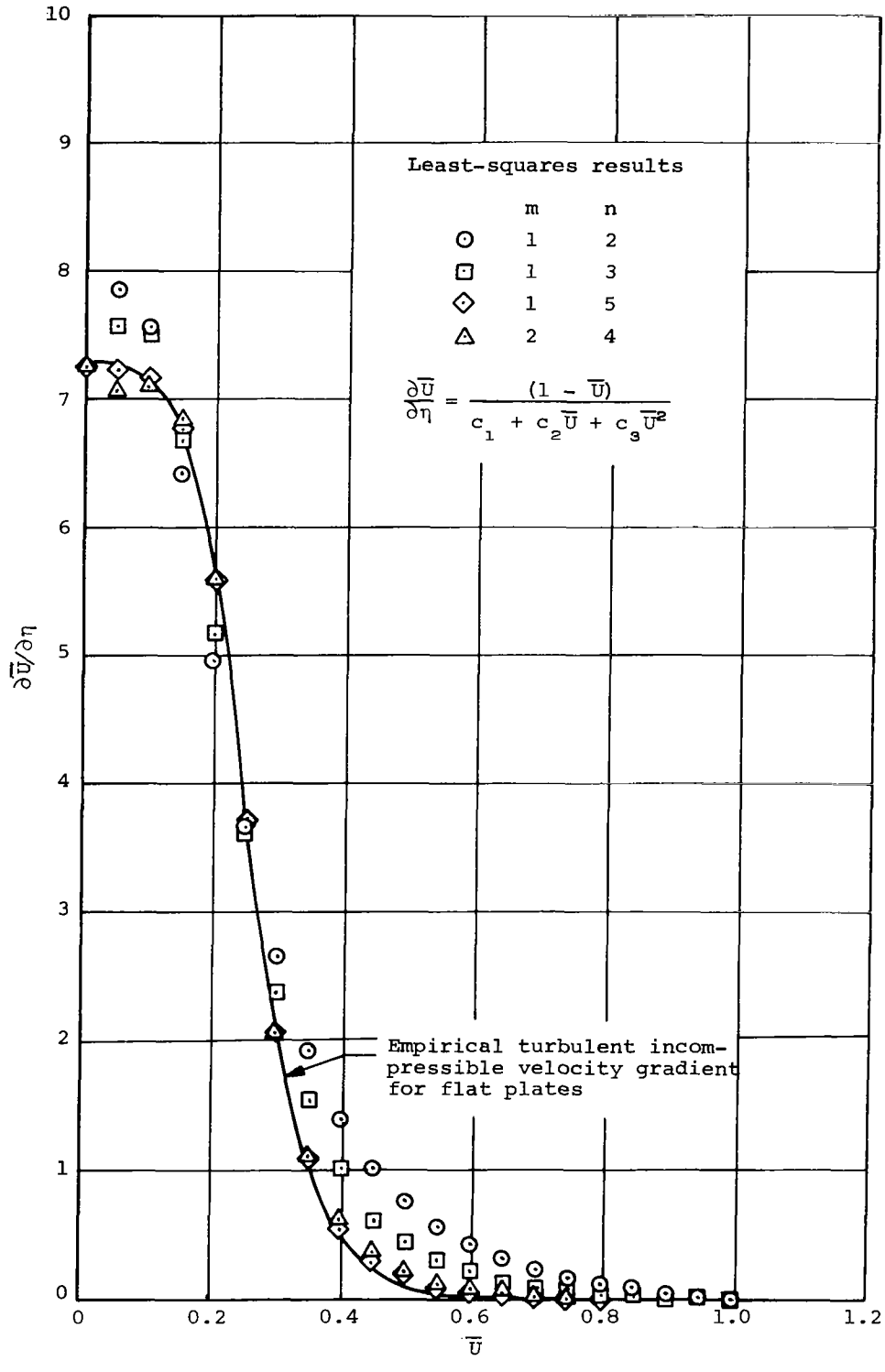

(c) $R_x = 10^8$.

Figure 2.- Concluded.

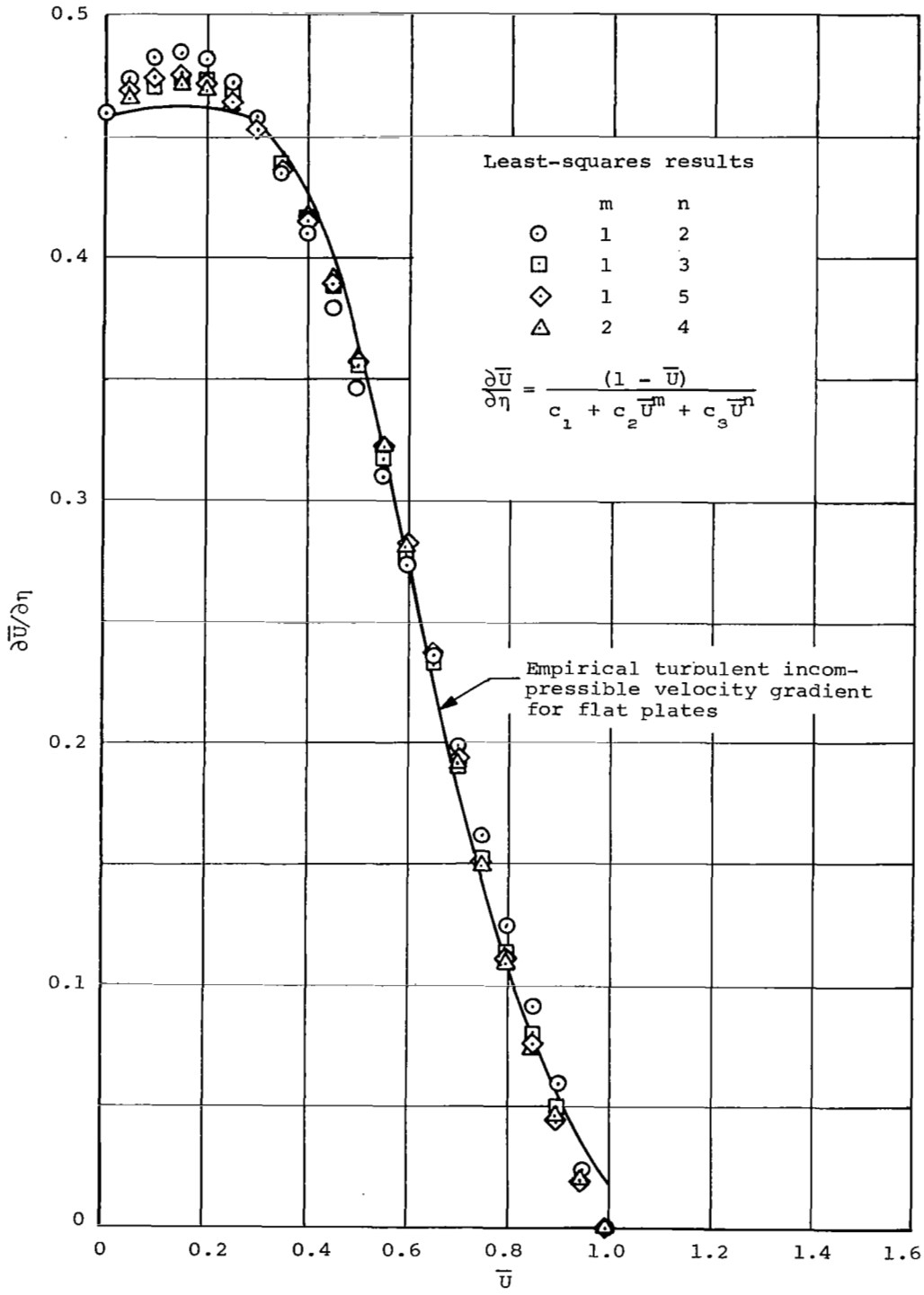

(a) $R_x = 10^4$.

Figure 3.- Comparison of root velocity gradients with empirical incompressible turbulent gradients as fitted by the least-squares method.

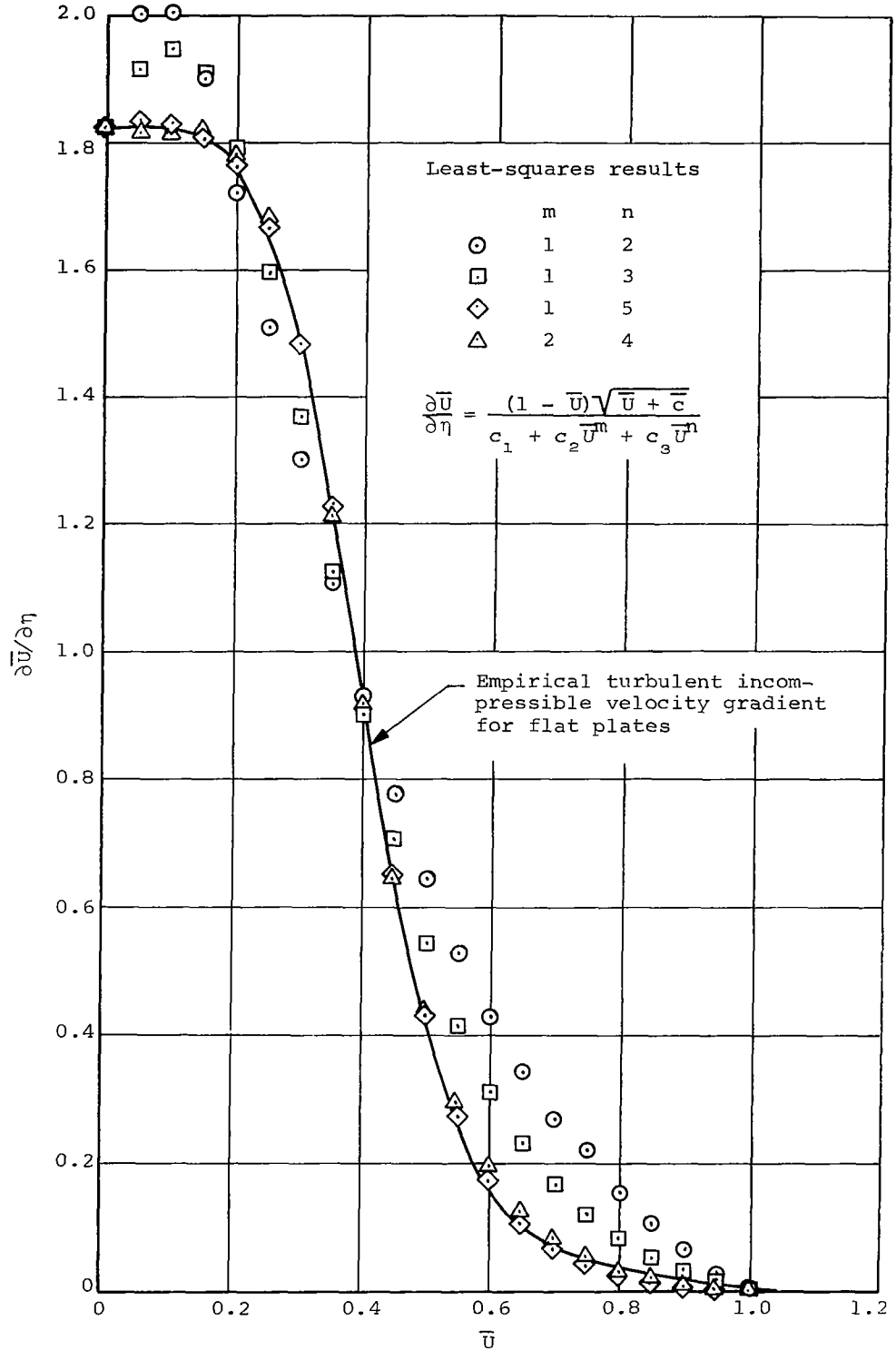

(b) $R_x = 10^6$.

Figure 3.- Continued.

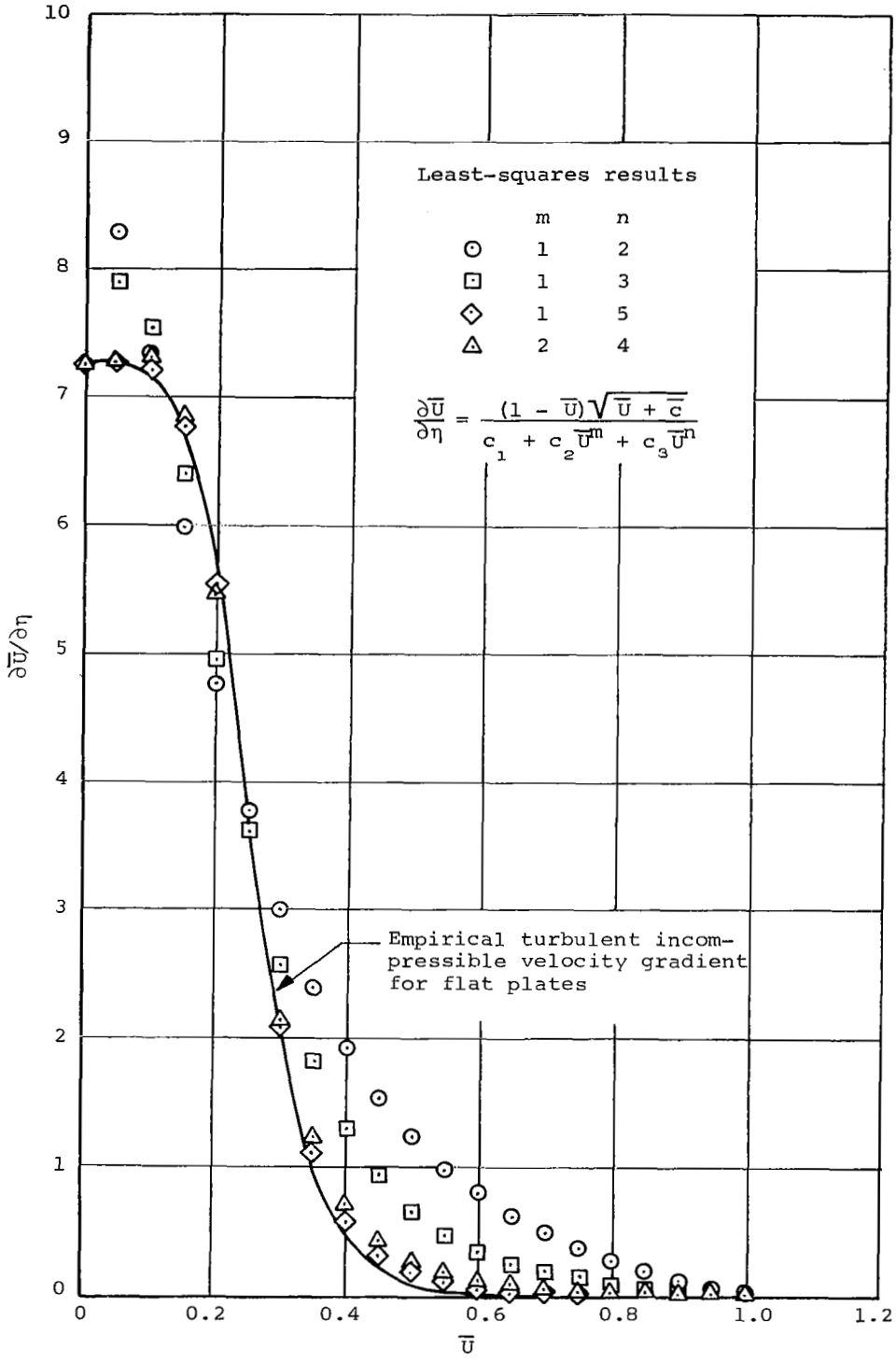

(c) $R_x = 10^8$.

Figure 3.- Concluded.

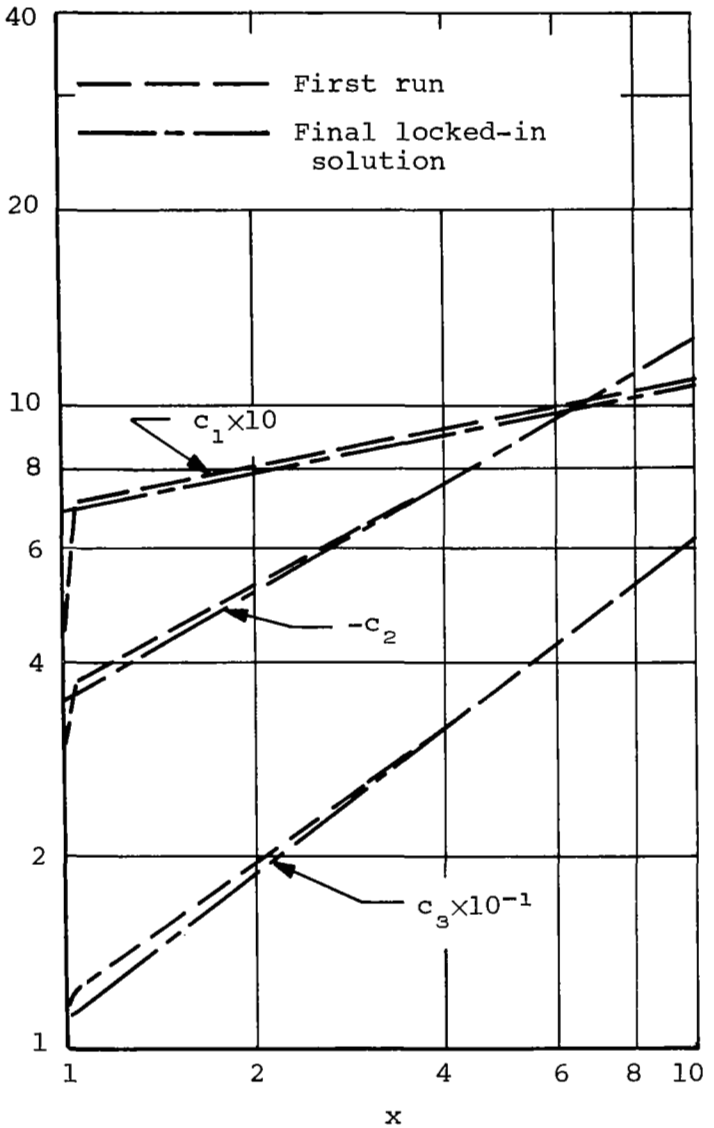

(a) Velocity-gradient coefficients.

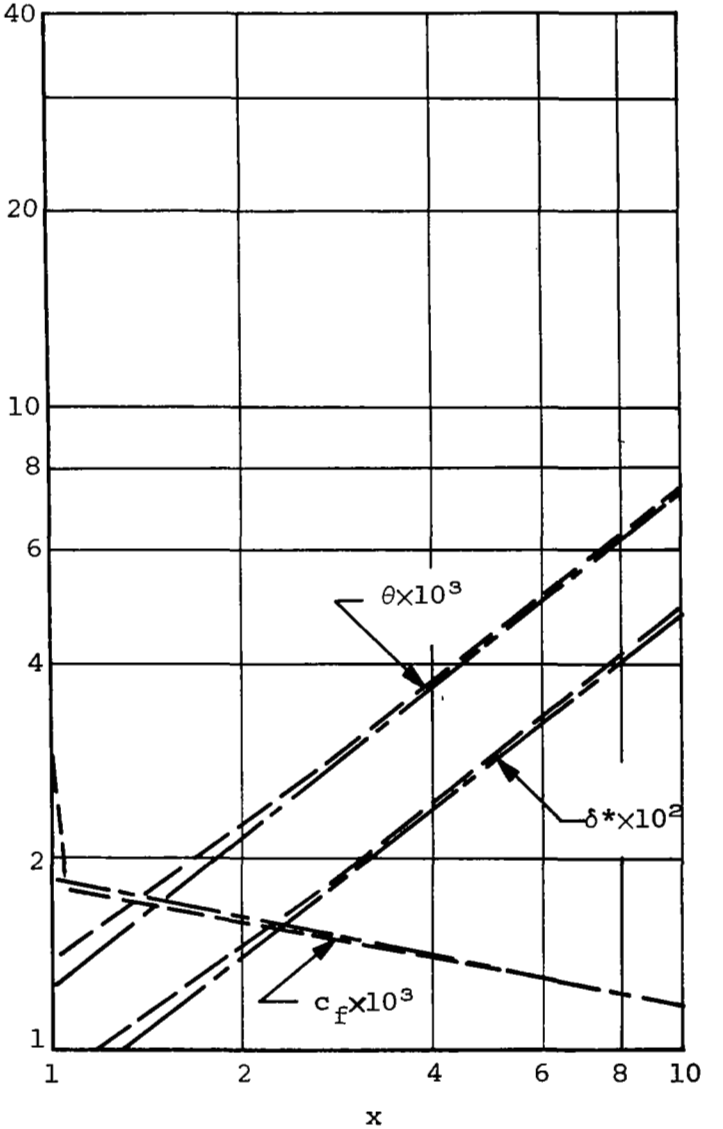

(b) Displacement thickness, momentum thickness, and skin-friction coefficient.

Figure 4.- Flat-plate calculated results illustrating method of developing locked-in solutions; M = 4, $R_{\ell_o} = 2.5 \times 10^6$.

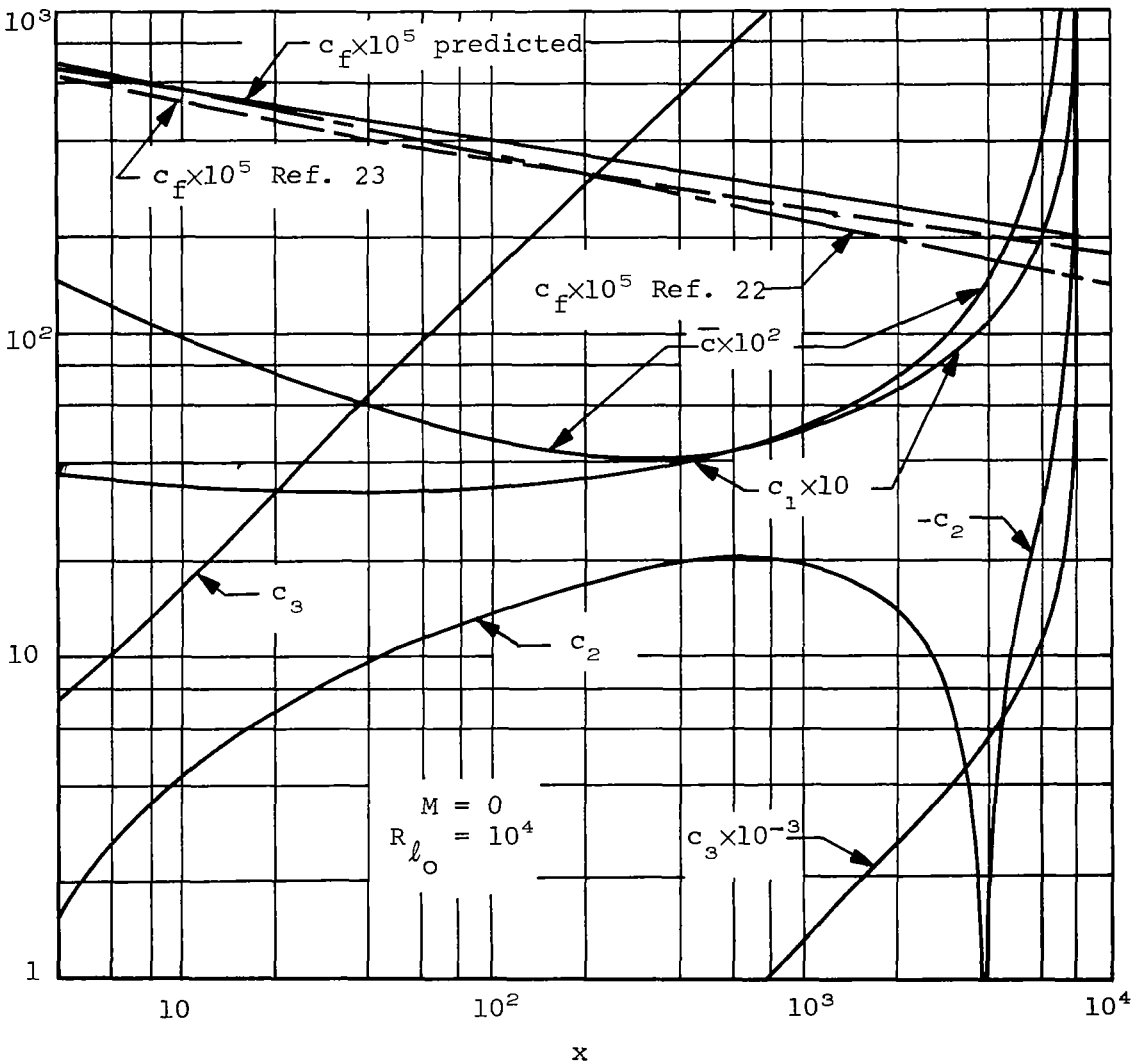

Figure 5.- Flat-plate results from computer program utilizing square-root formulation; M = 0, $R_{\ell_o} = 10^4$.

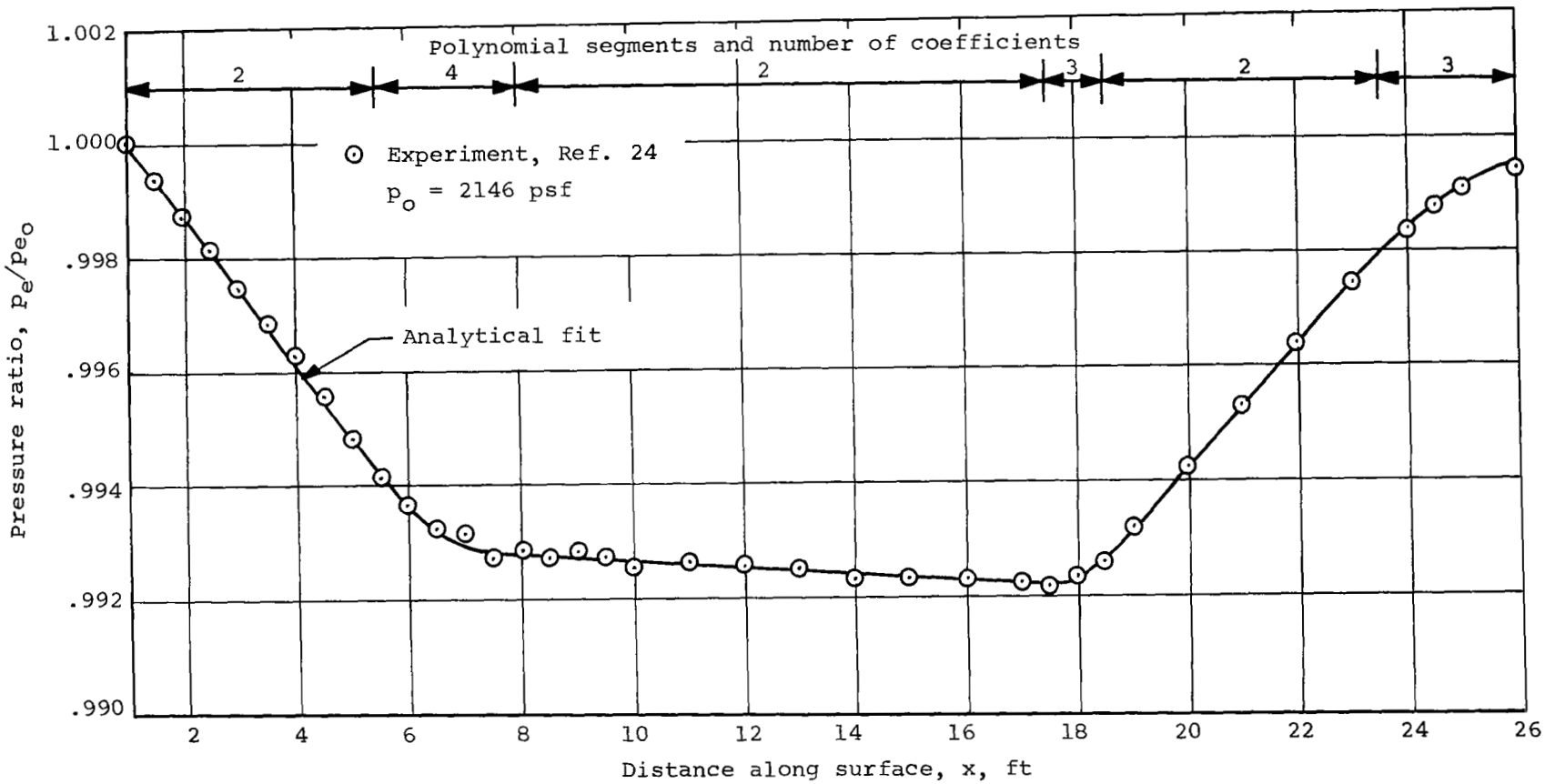

Figure 6.- Analytical fit to pressure distribution of Schubauer and Klebanoff.

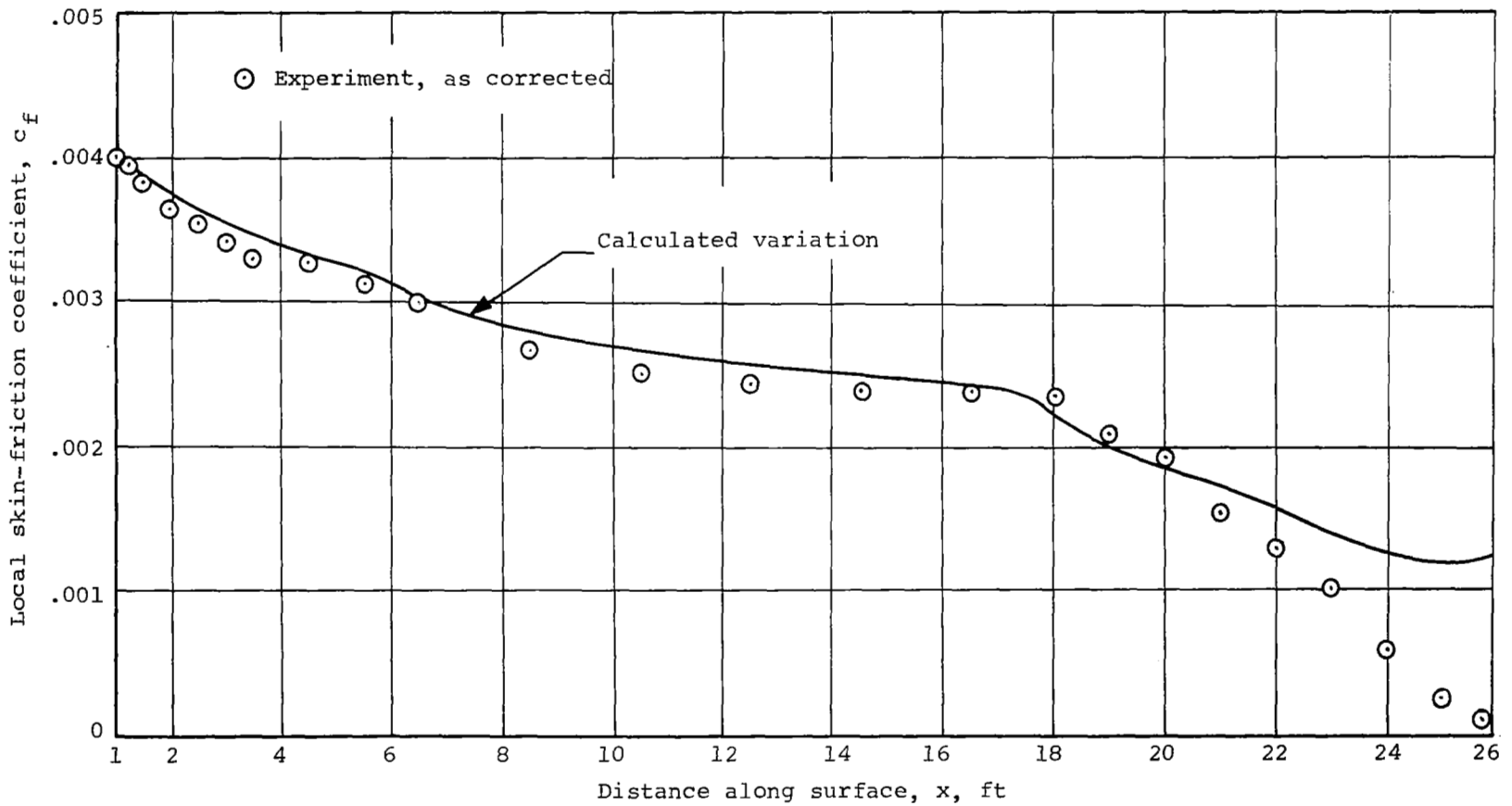

(a) Skin-friction coefficient.

Figure 7.- Comparison of theoretical predictions with experimental results of Schubauer and Klebanoff; reference 24.

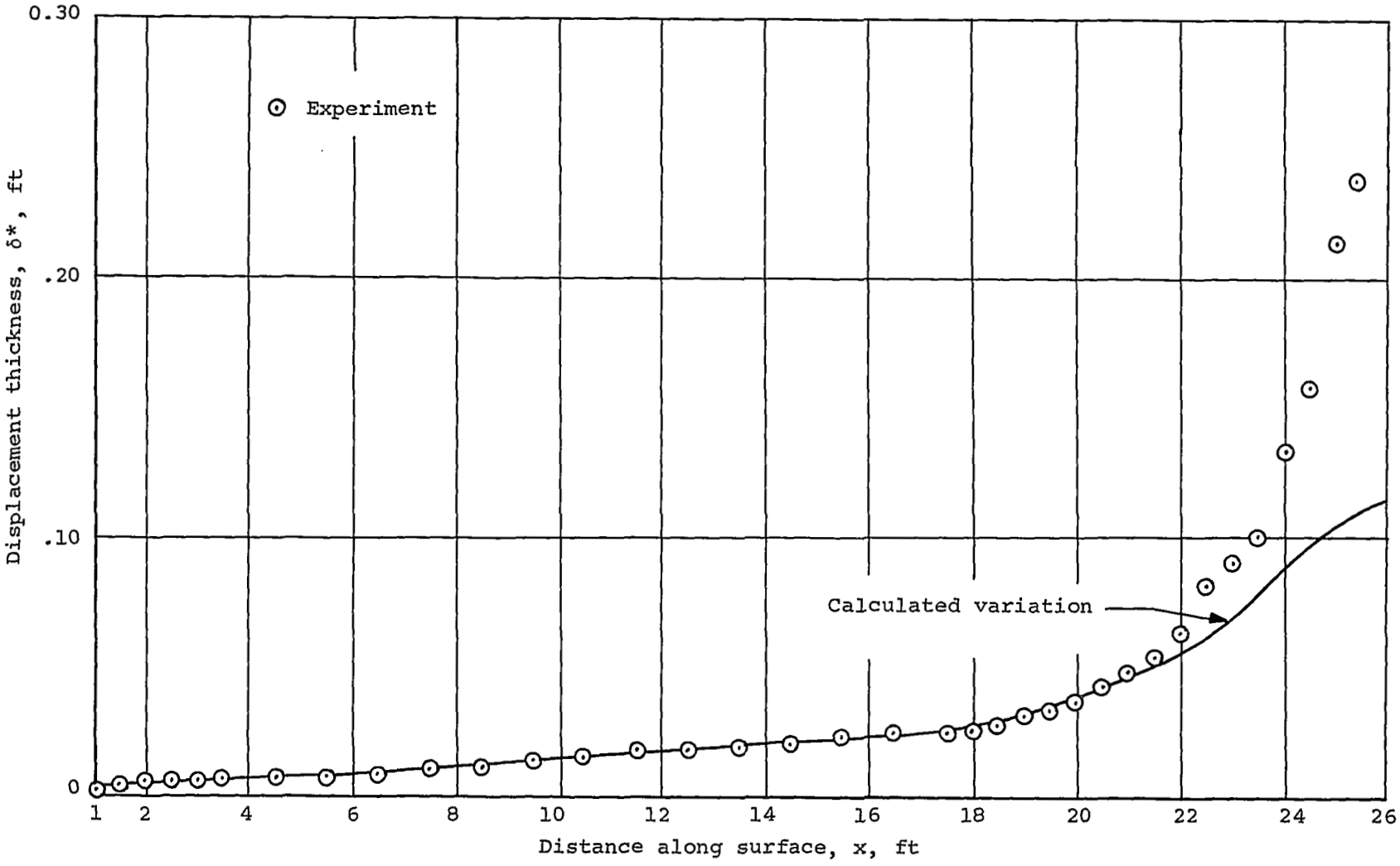

(b) Displacement thickness.

Figure 7.- Continued.

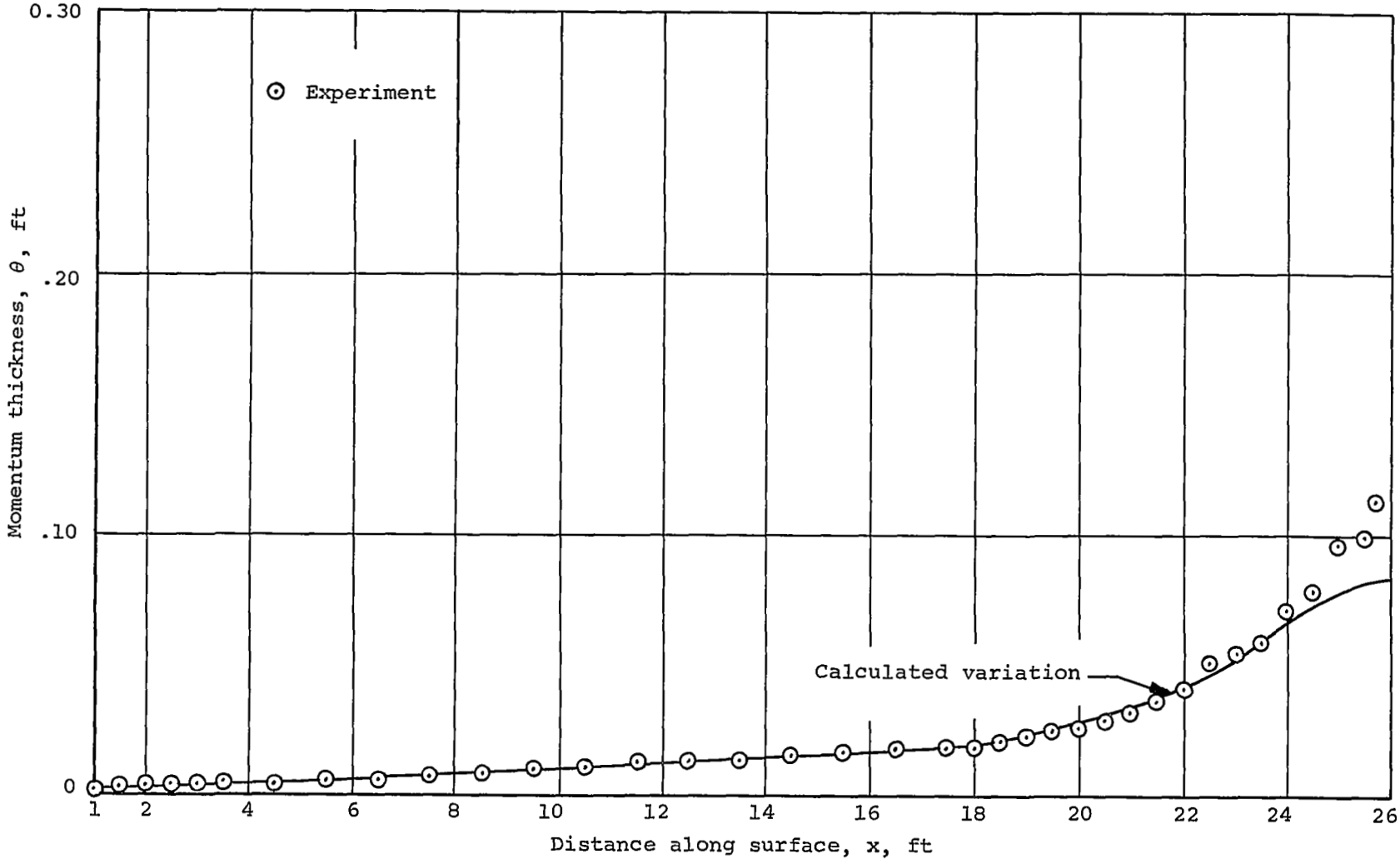

(c) Momentum thickness.

Figure 7.- Concluded.

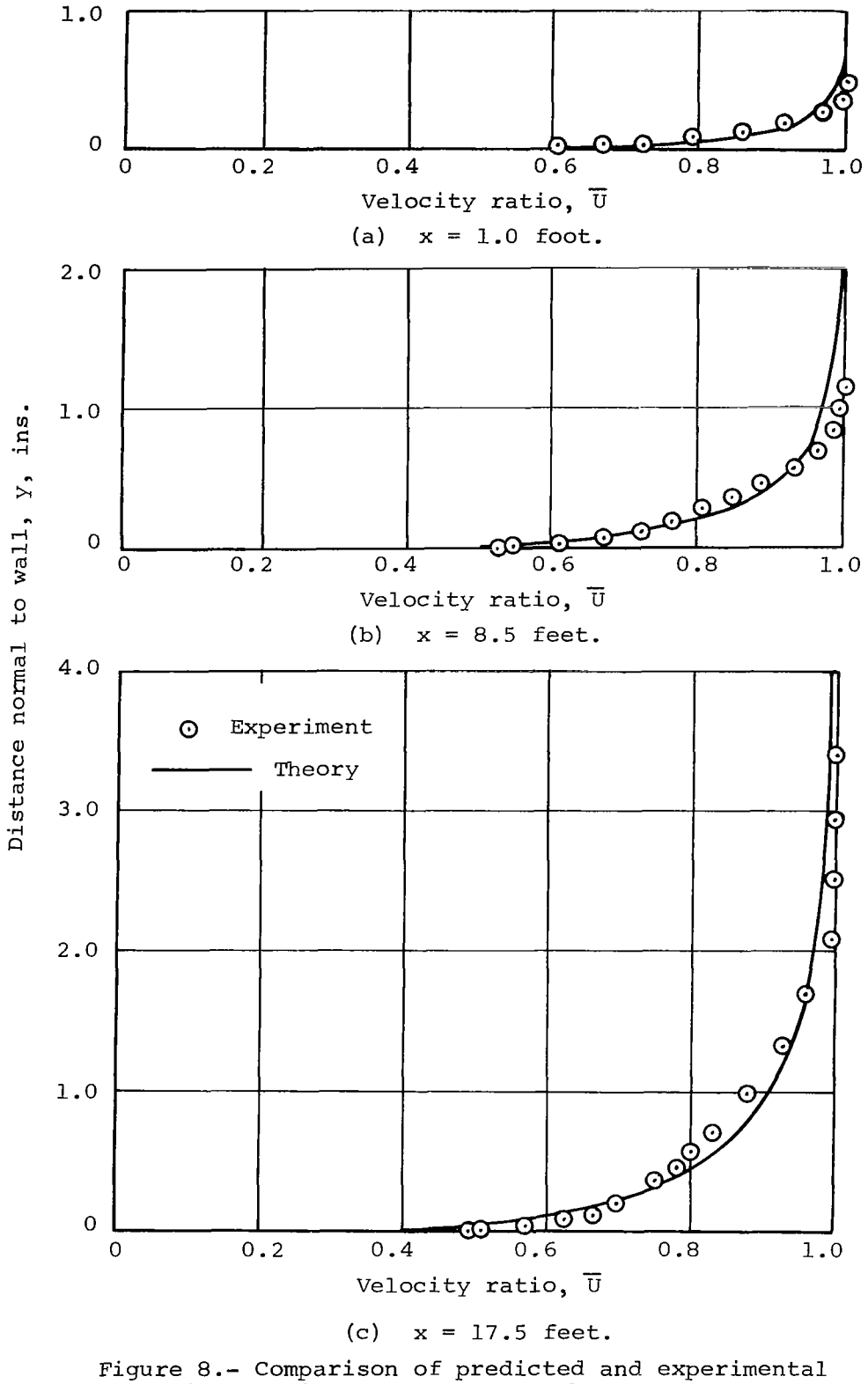

Figure 8.- Comparison of predicted and experimental velocity profiles for case of Schubauer and Klebanoff, reference 24.

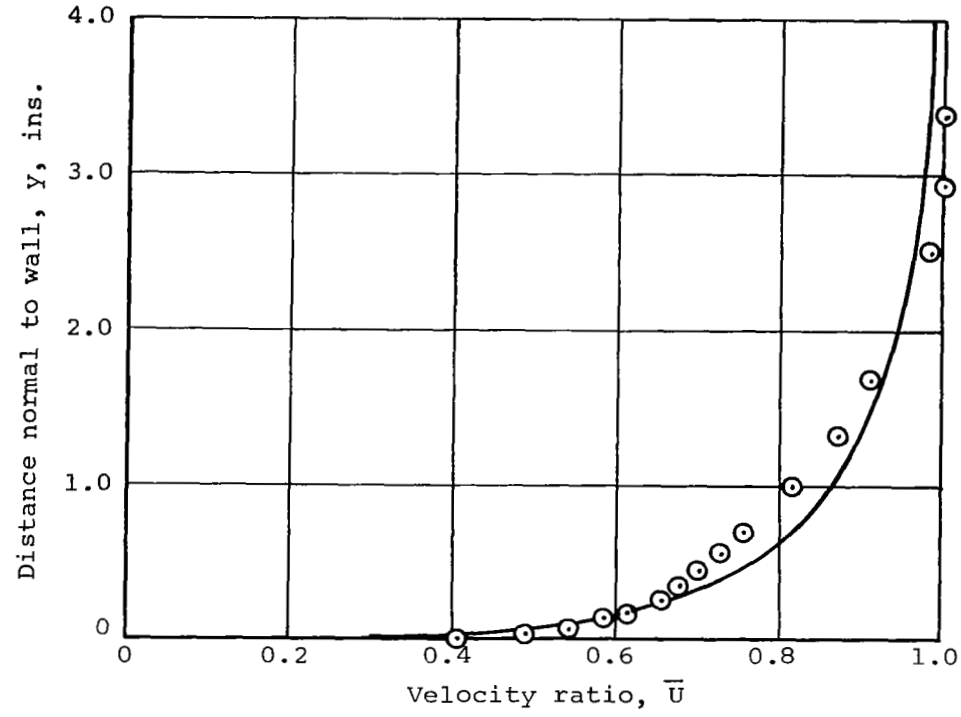

(d) x = 20.0 feet.

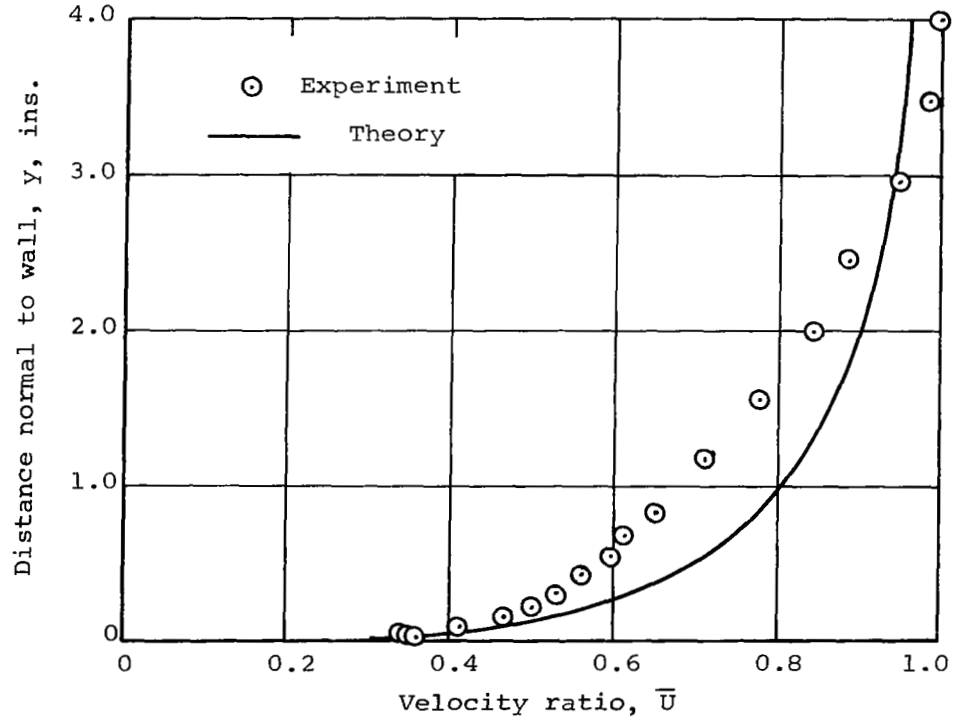

(e) x = 22.0 feet.

Figure 8.- Continued.

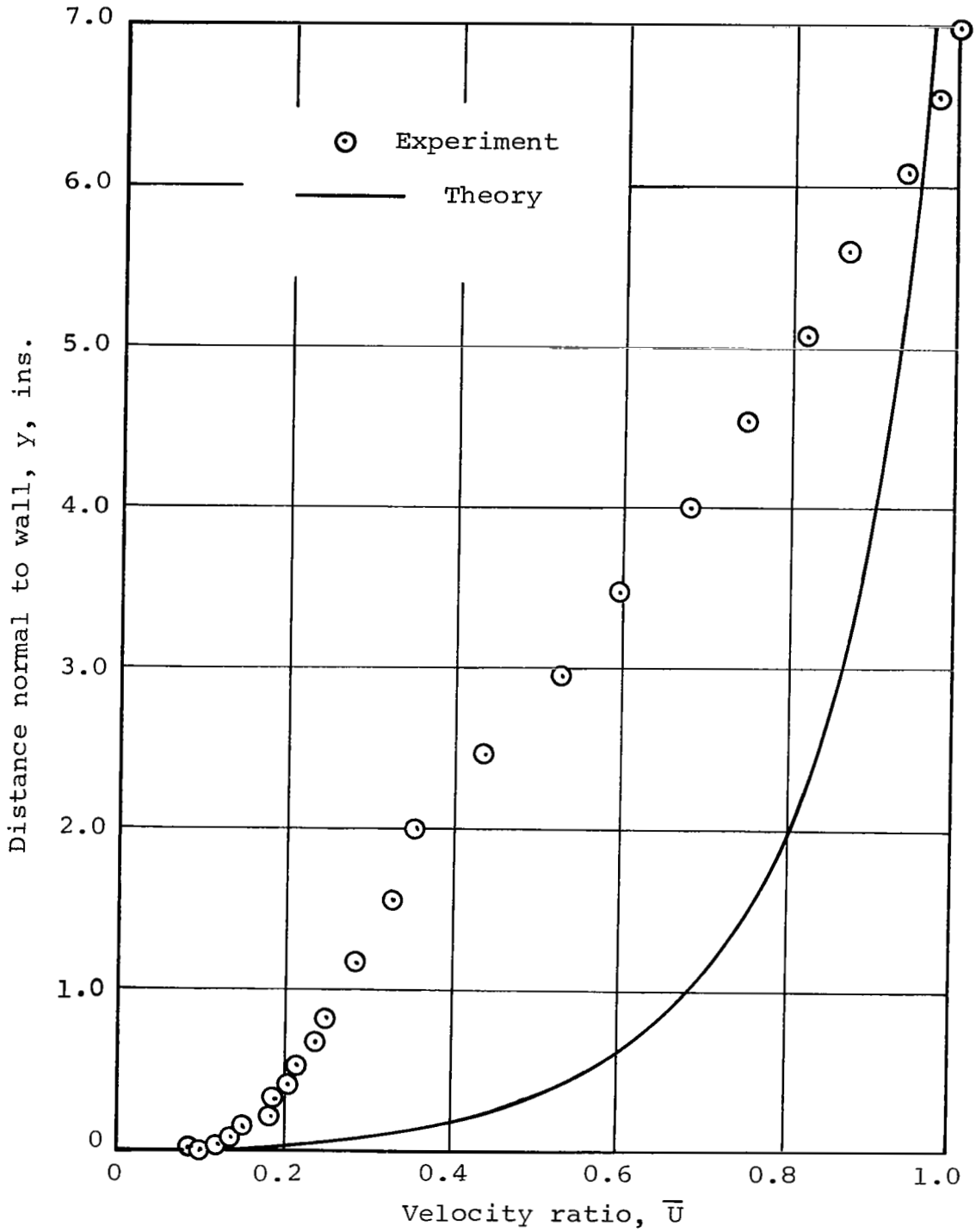

(f) x = 25.4 feet.

Figure 8.- Concluded.

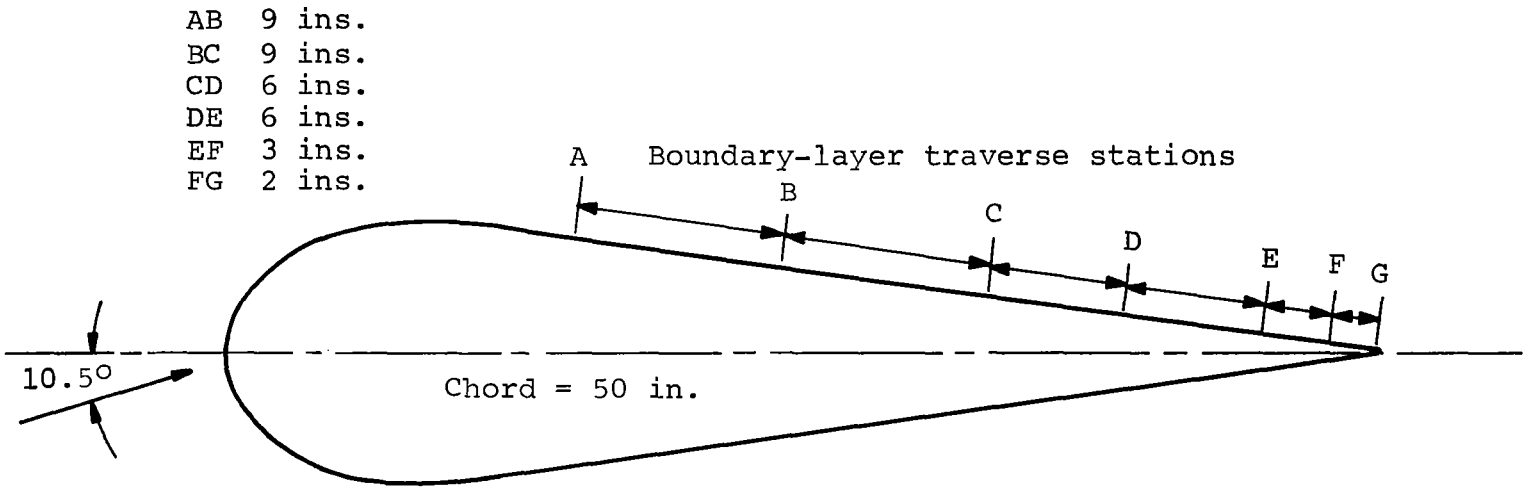

Figure 9 .- Airfoil configuration tested by Newman, reference 25.

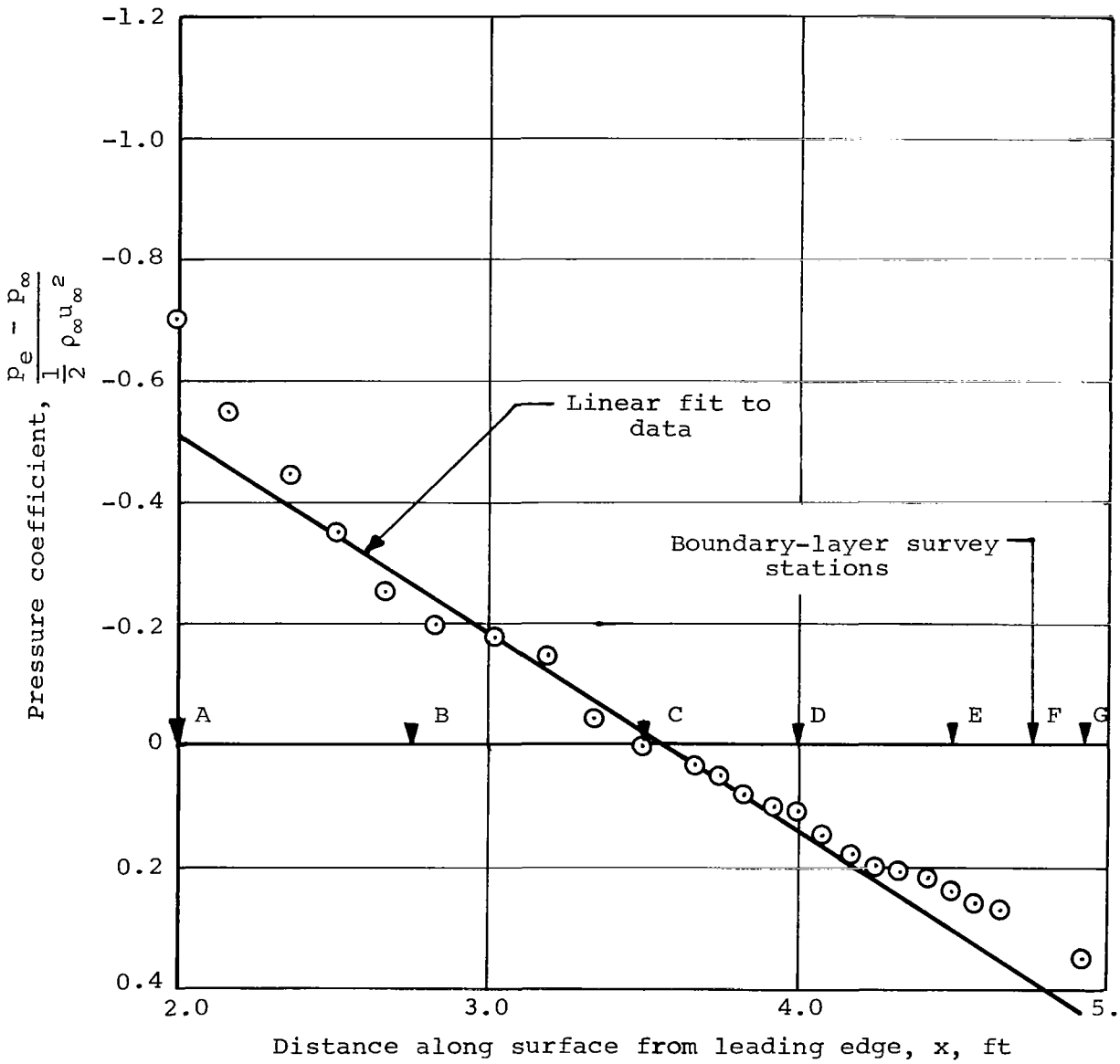

Figure 10.- Pressure Distribution for the data of Newman, reference 25.

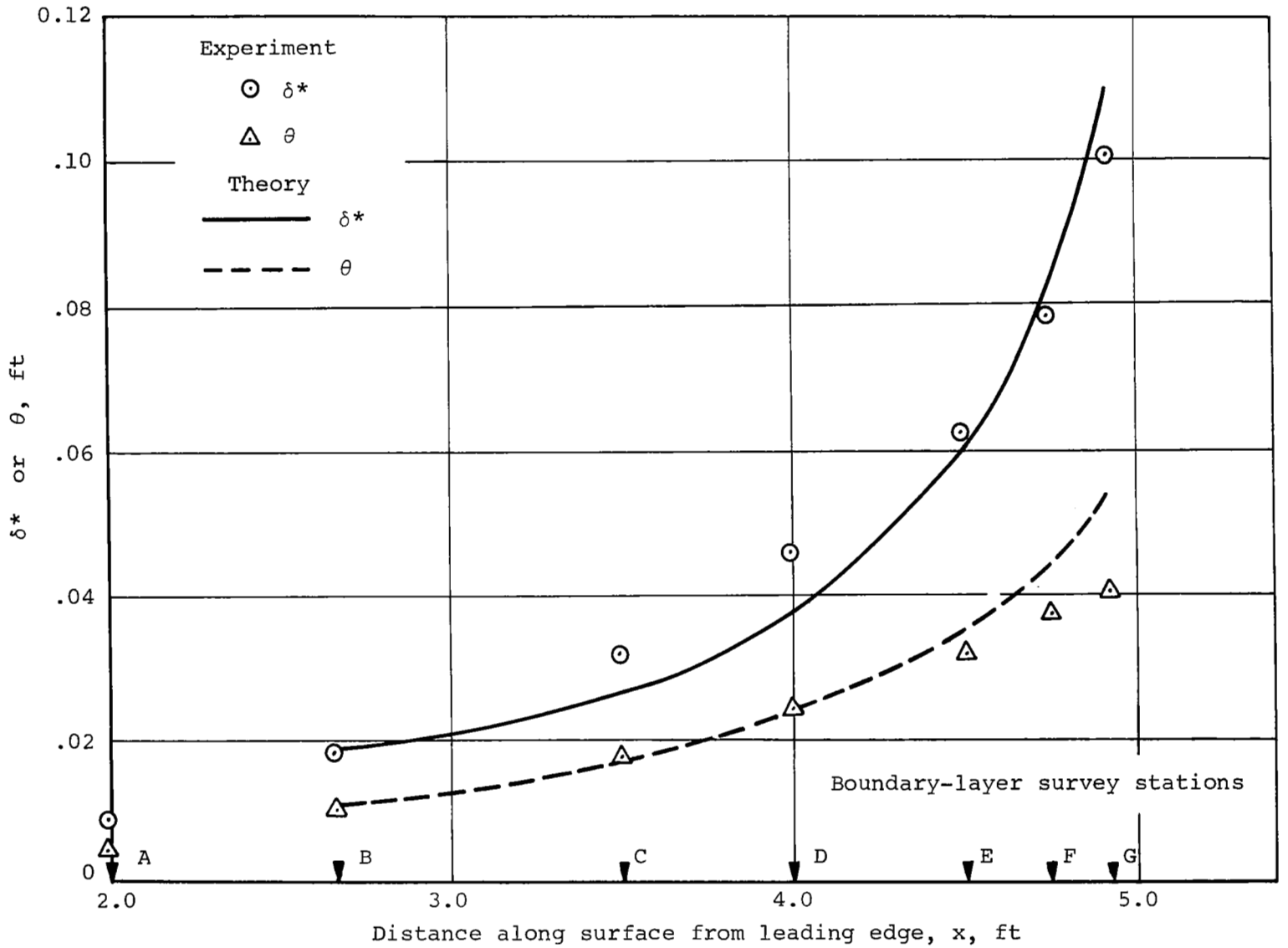

(a) Displacement and momentum thicknesses.

Figure 11.- Comparison of predicted and measured boundary-layer quantities for the case of Newman, reference 25.

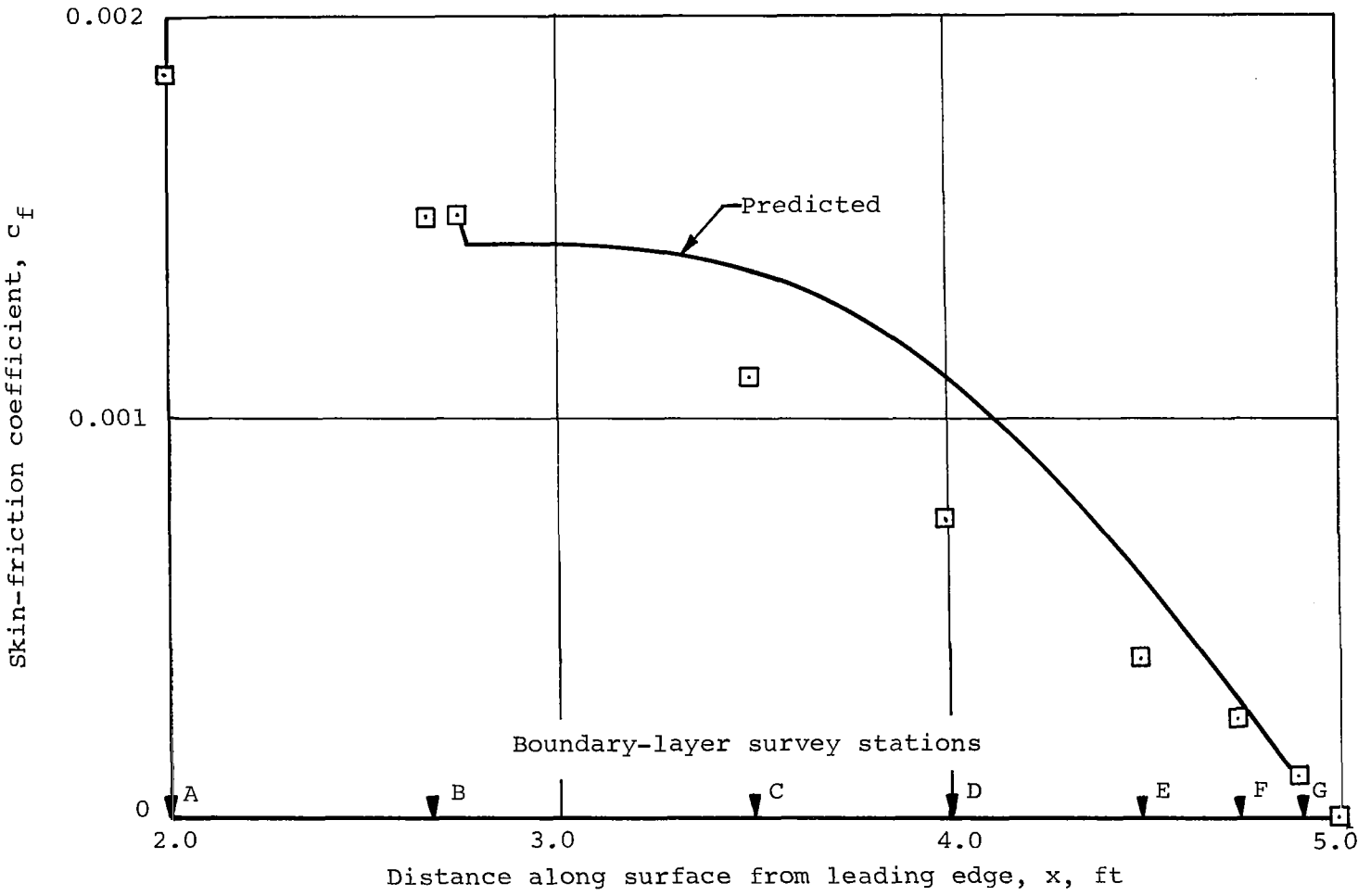

(b) Skin-friction coefficient.

Figure 11.- Concluded.

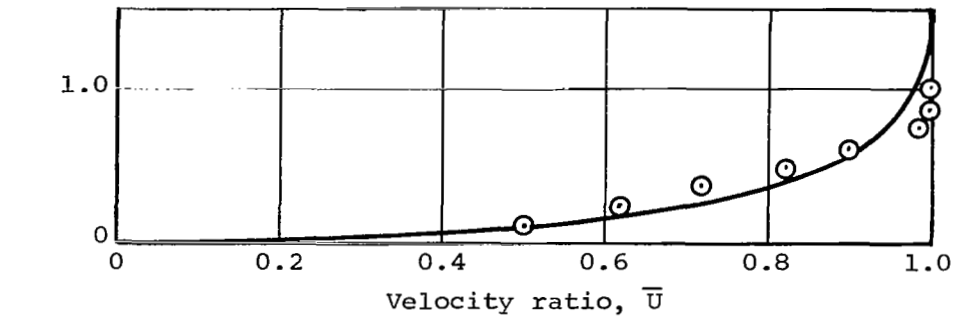

(a) Station B; x = 2.75 feet.

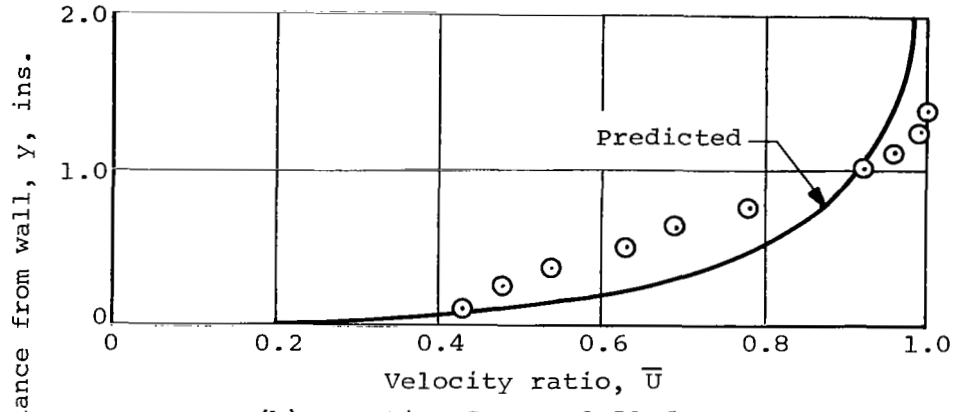

(b) Station C; x = 3.50 feet.

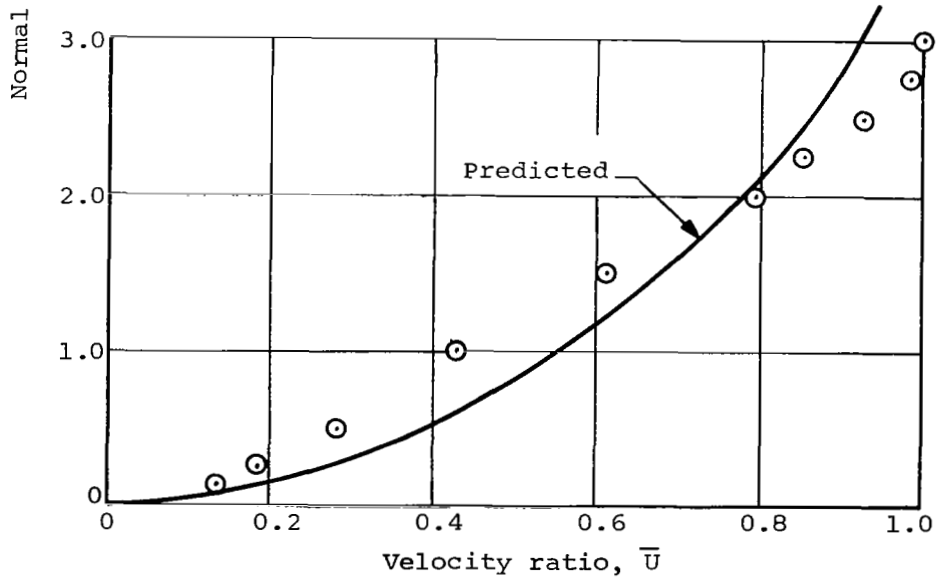

(c) Station G; x = 4.92 feet.

Figure 12.- Comparison of predicted velocity profiles with those from the data of Newman, reference 25.

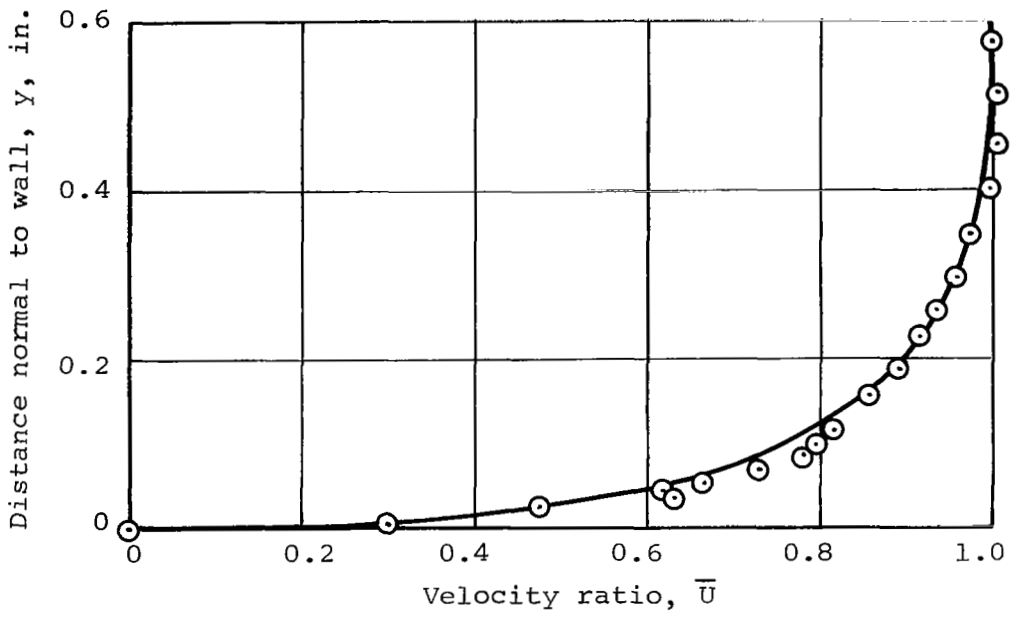

(a) Velocity profile, x = 2.17 feet.

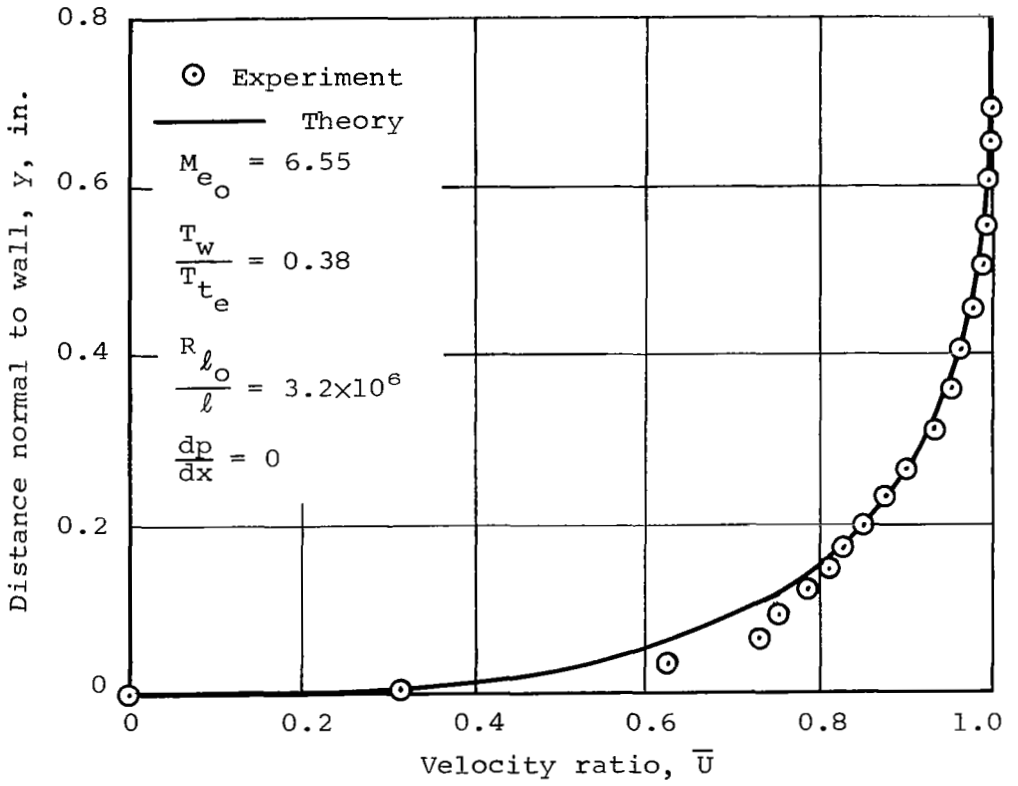

(b) Velocity profile; x = 2.95 feet.

Figure 13.- Comparison between theory and experiment for hypersonic turbulent boundary layer on a flat plate; no incident shock.

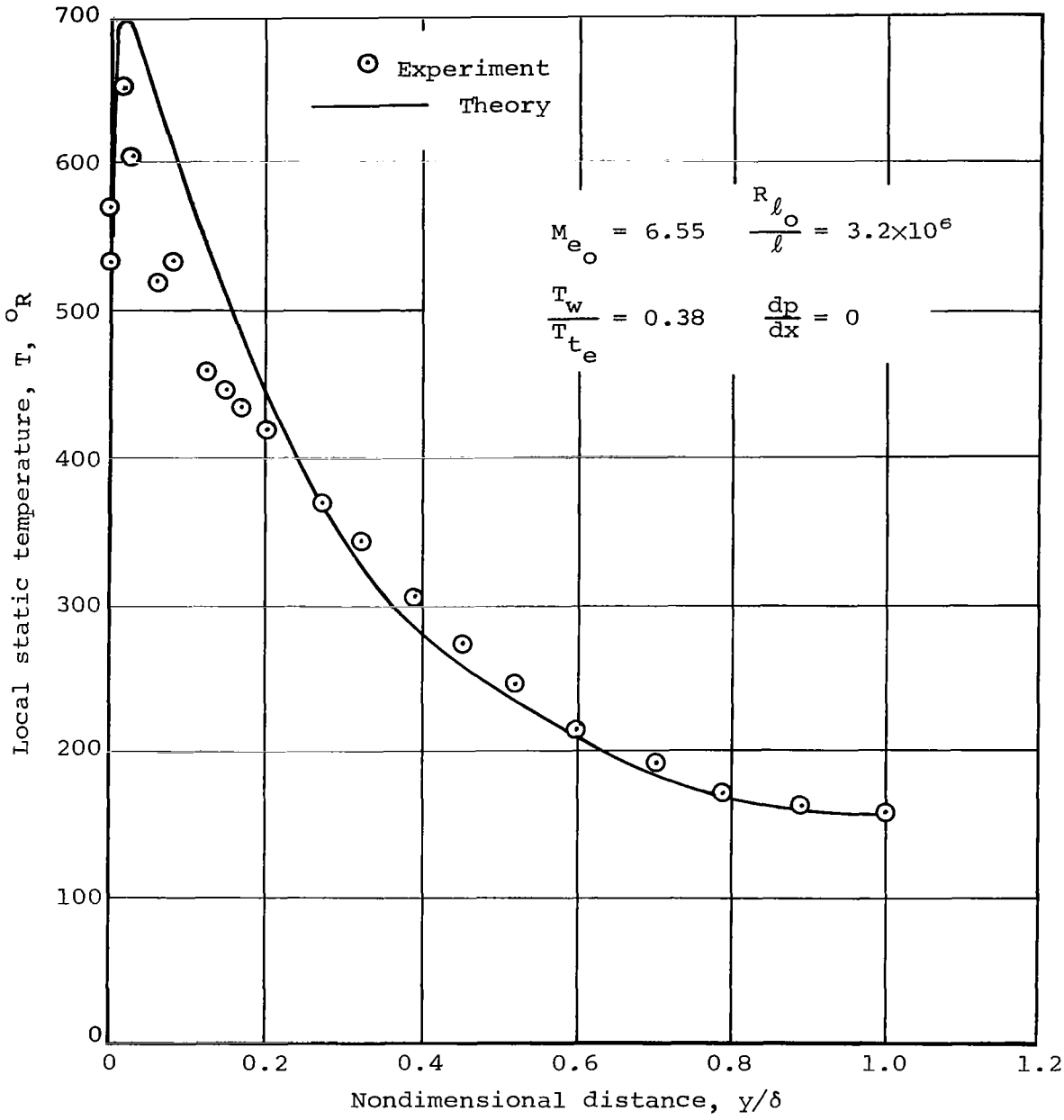

(c) Temperature profile; x = 2.17 feet.

Figure 13.- Concluded.

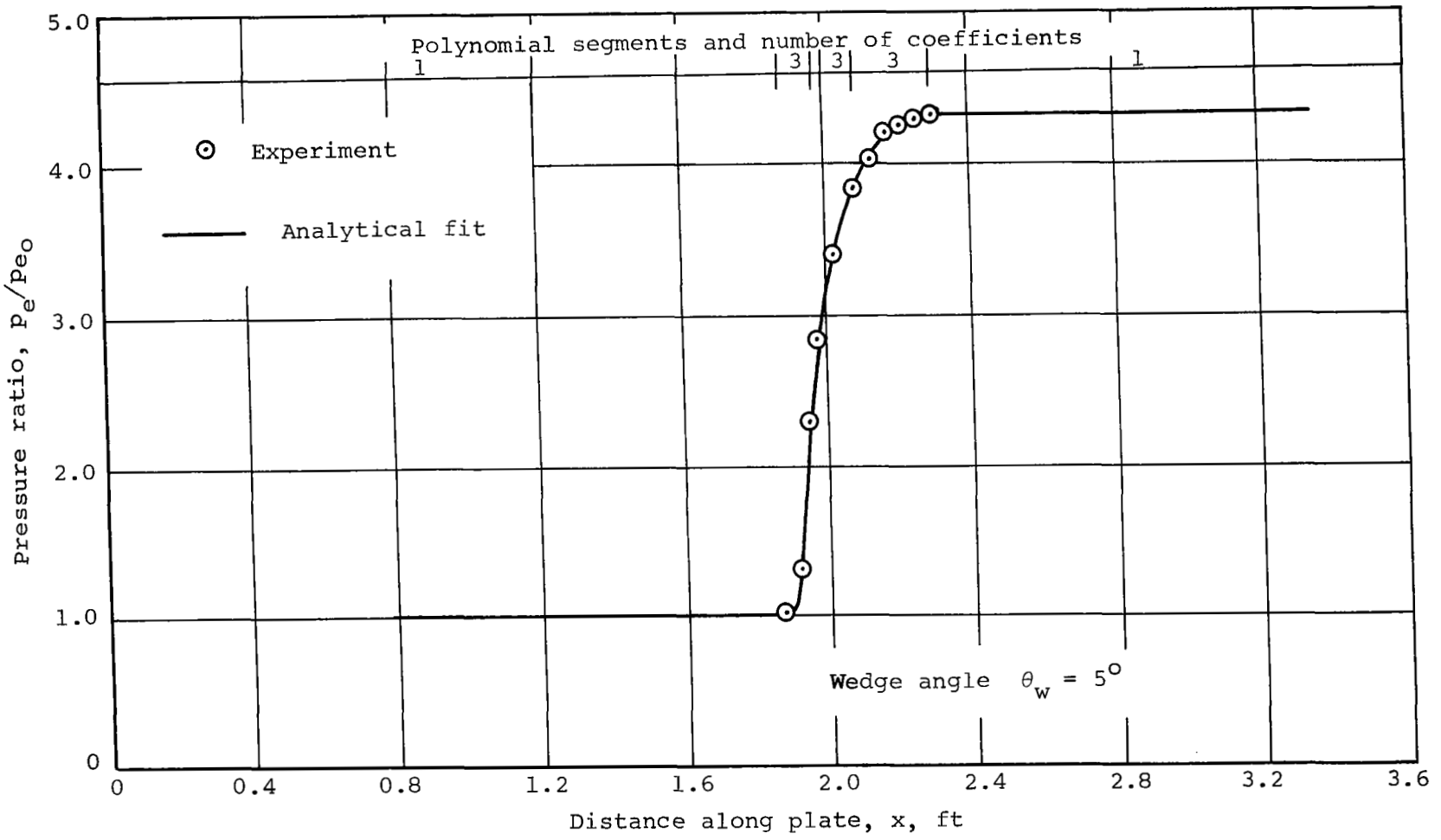

Figure 14.- Experimental and fitted pressure distributions acting on hypersonic boundary layer on flat plate due to wedge-induced oblique shock.

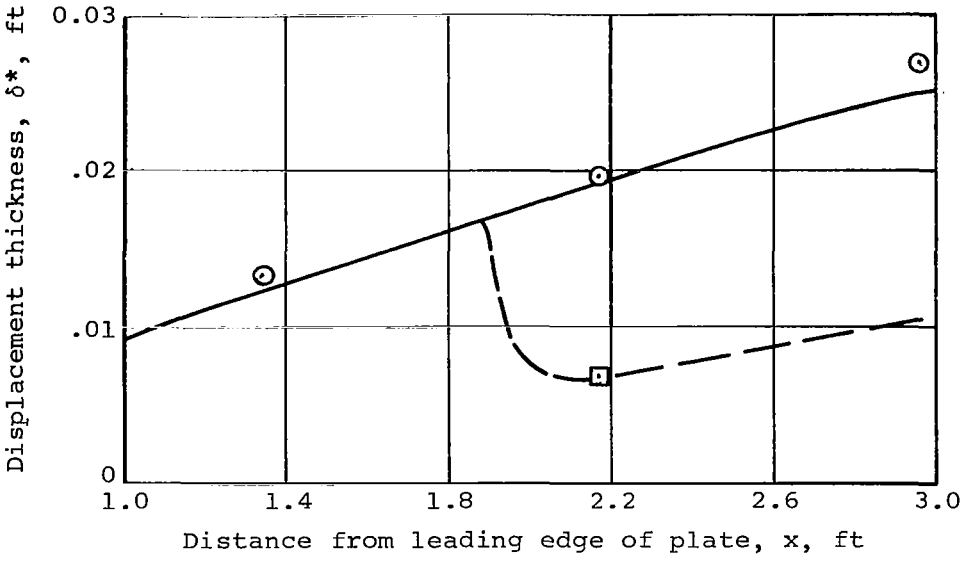

(a) Displacement thickness.

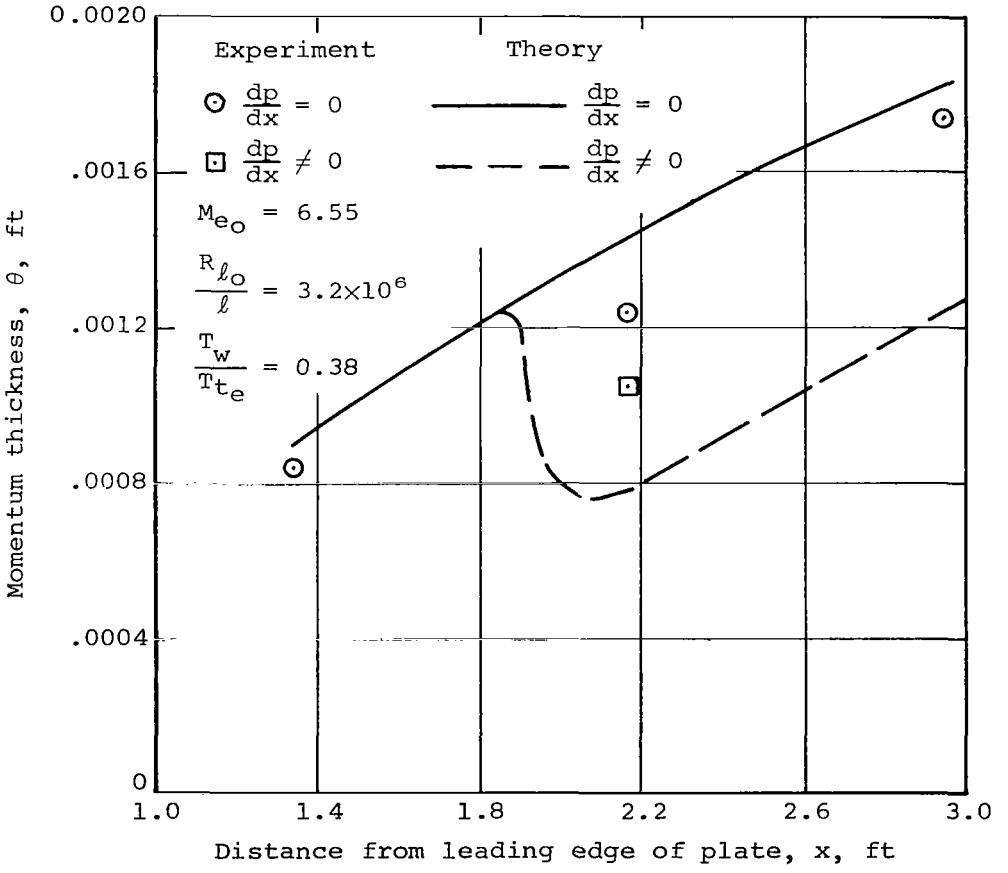

(b) Momentum thickness.

Figure 15.- Comparison of predicted and measured quantities for hypersonic turbulent boundary layer with and without incident oblique shock.

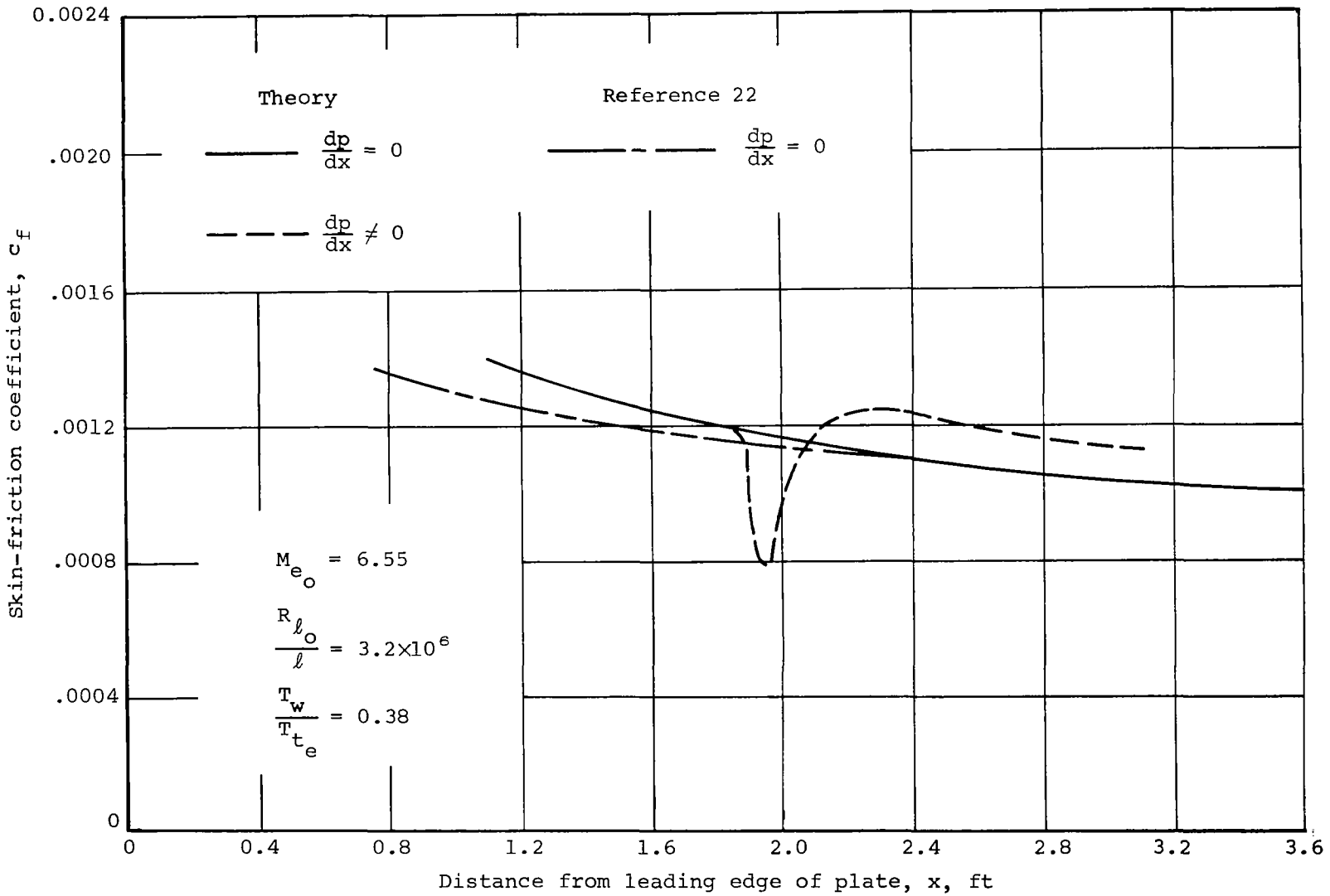

Figure 16.- Comparison of calculated skin-friction distributions for hypersonic turbulent boundary layer on flat plate with and without incident oblique shock.

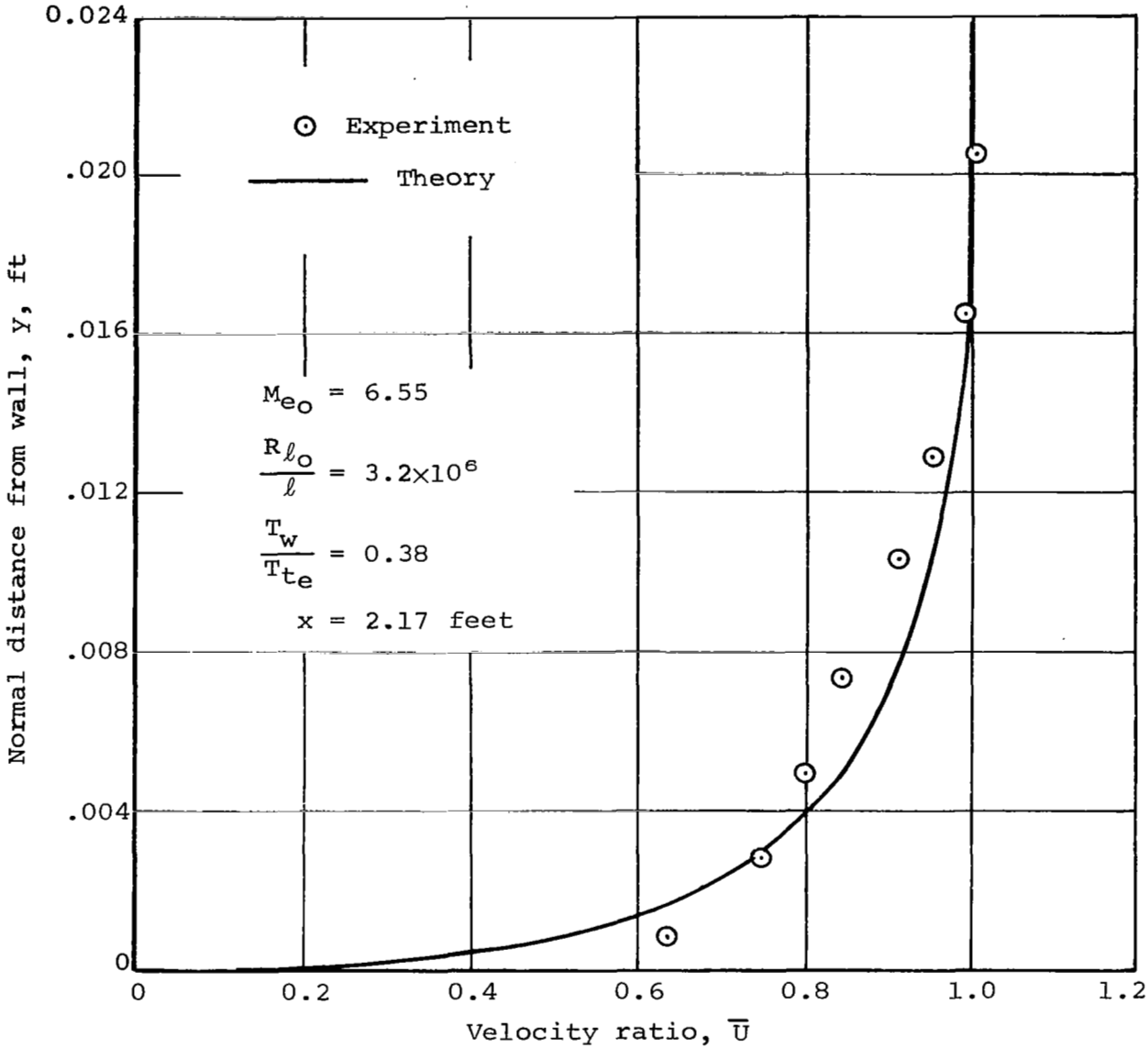

Figure 17.- Comparison between theoretical and experimental velocity profiles for hypersonic turbulent boundary layer just downstream of interaction.

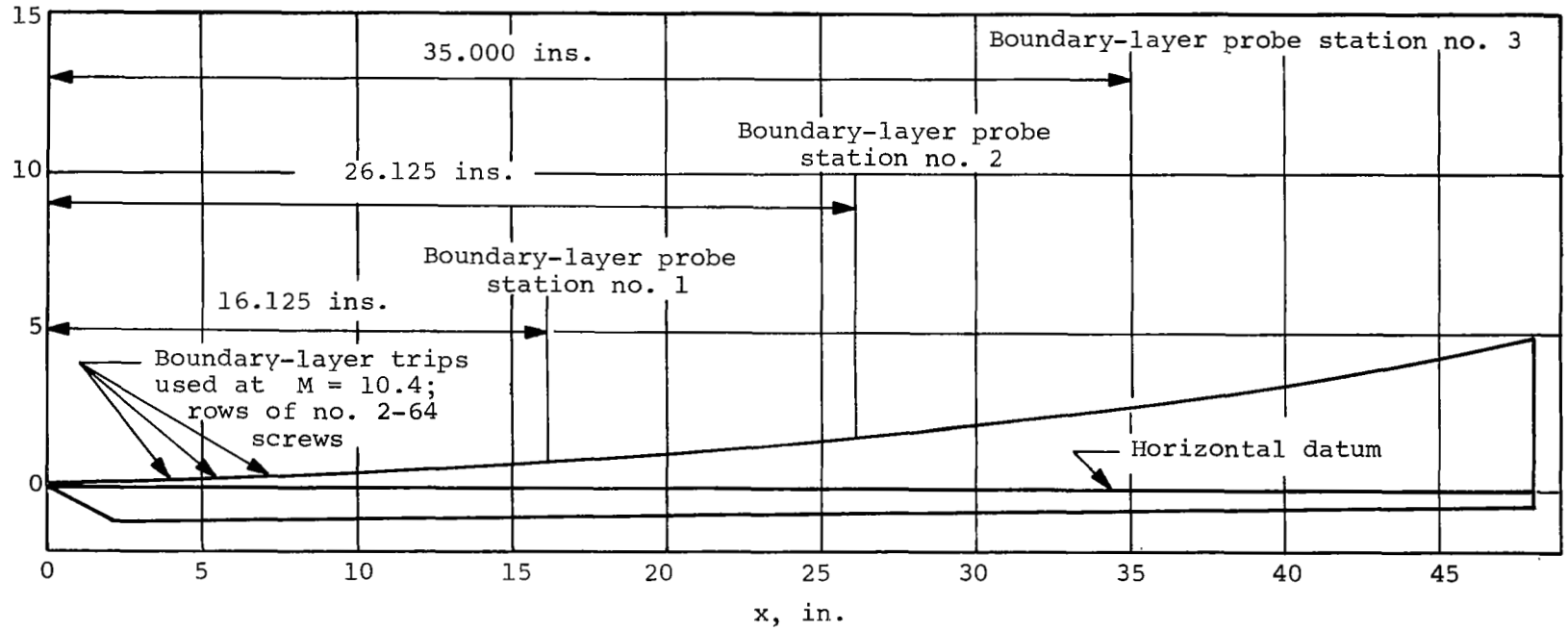

Figure 18.- Compression surface configuration tested at M_∞ = 7.4 and 10.4; reference 26.

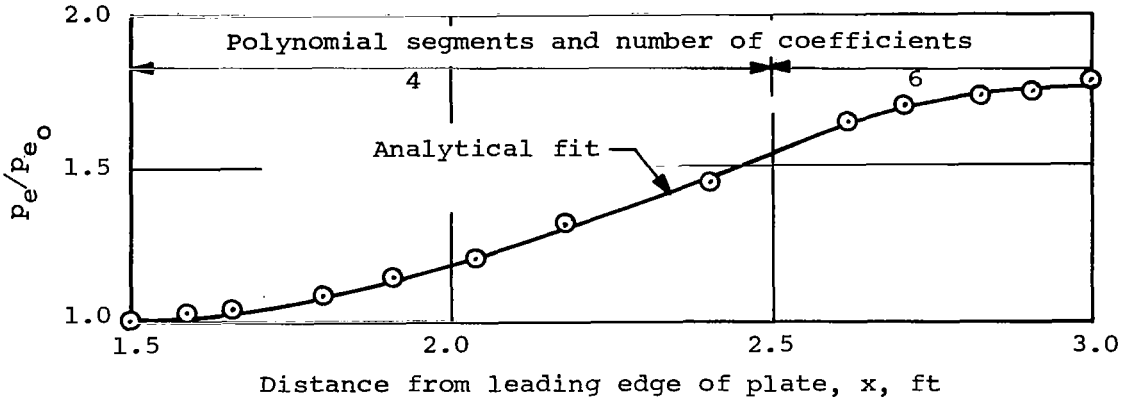

(a) Pressure distribution.

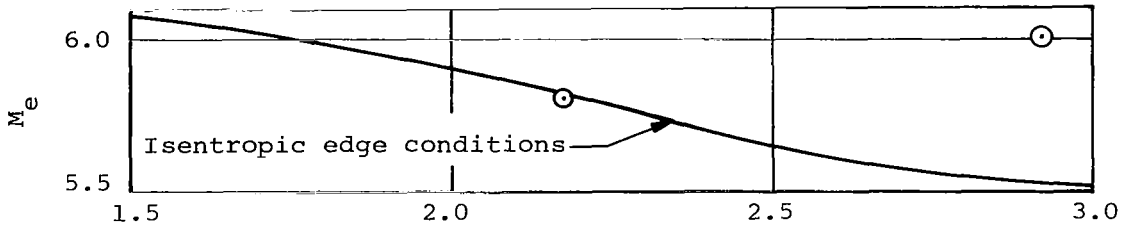

(b) Edge Mach number.

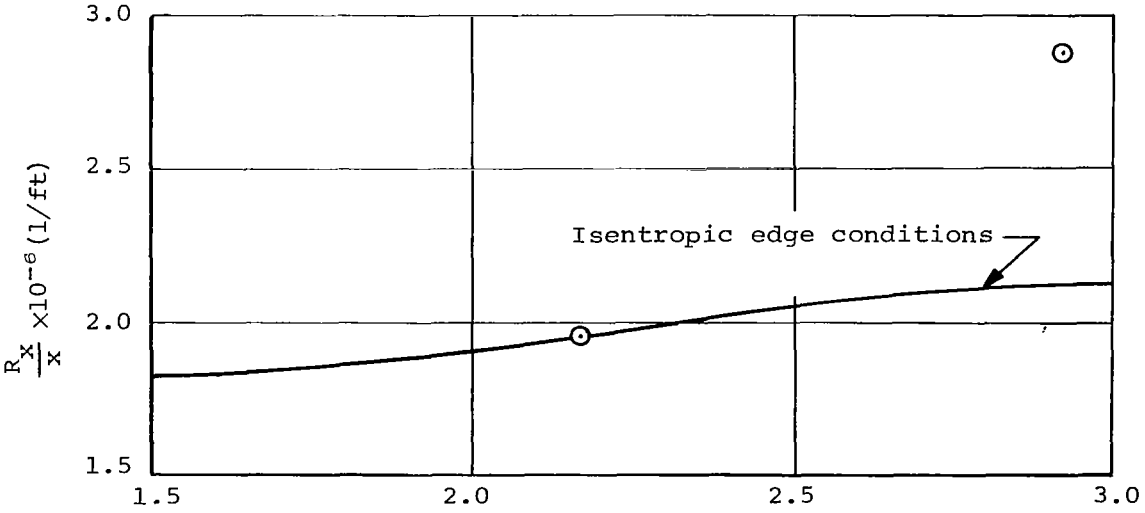

(c) Edge Reynolds number per foot.

Figure 19.- Comparison of boundary-layer edge conditions with experimental conditions for $M_\infty = 7.4$.

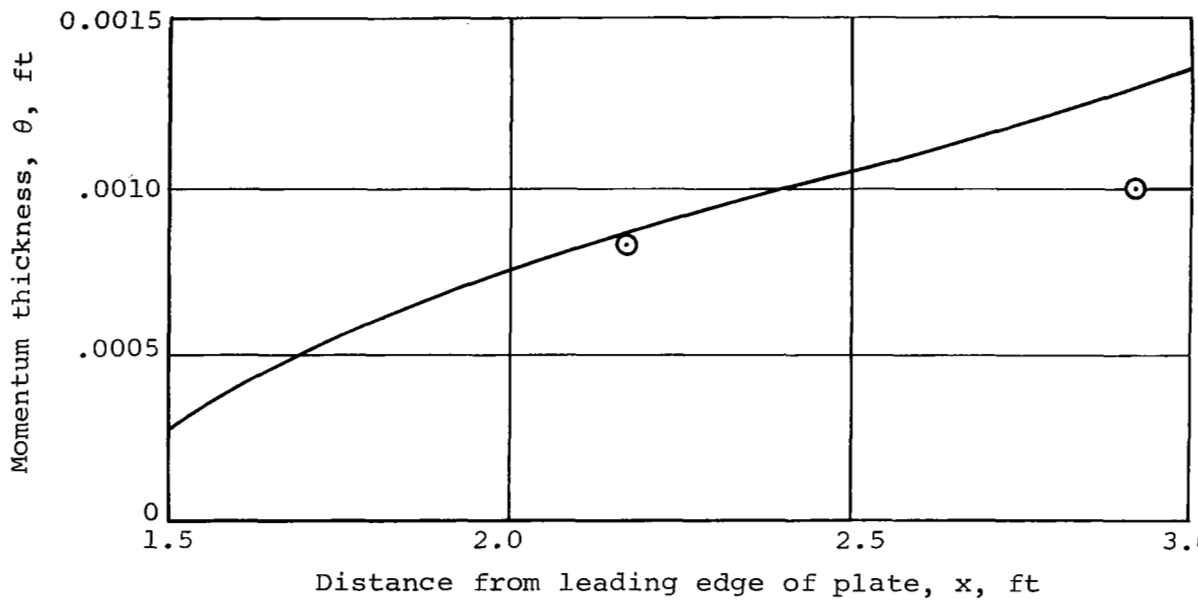

(a) Momentum thickness.

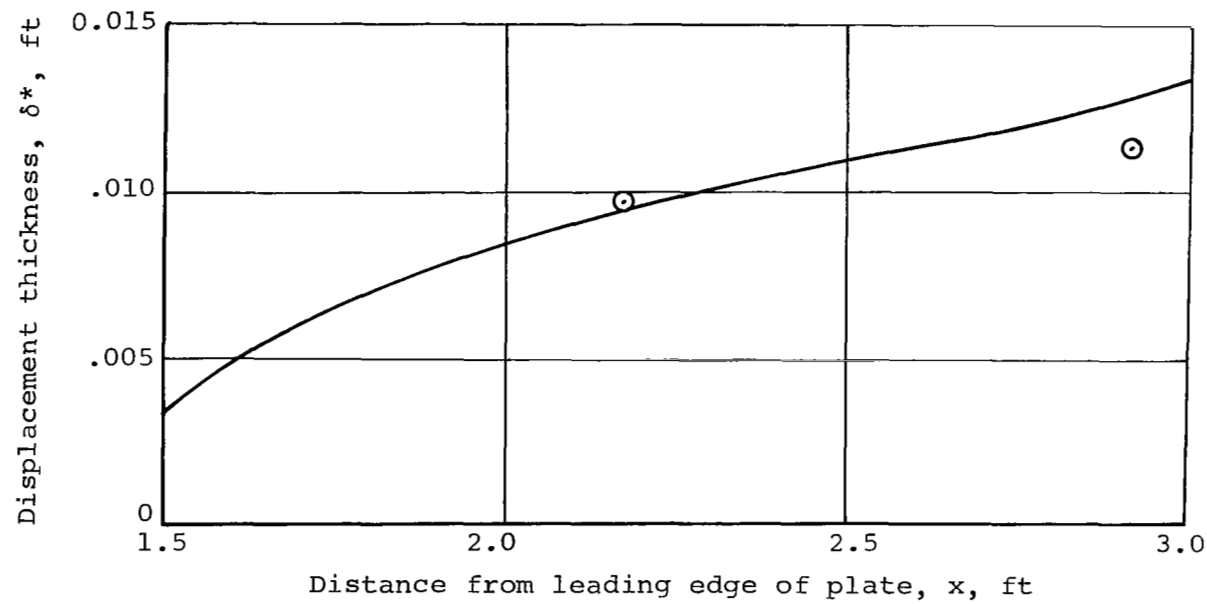

(b) Displacement thickness.

Figure 20.- Comparison of predicted and measured displacement and momentum thicknesses for compression surface tested at $M_\infty = 7.4$.

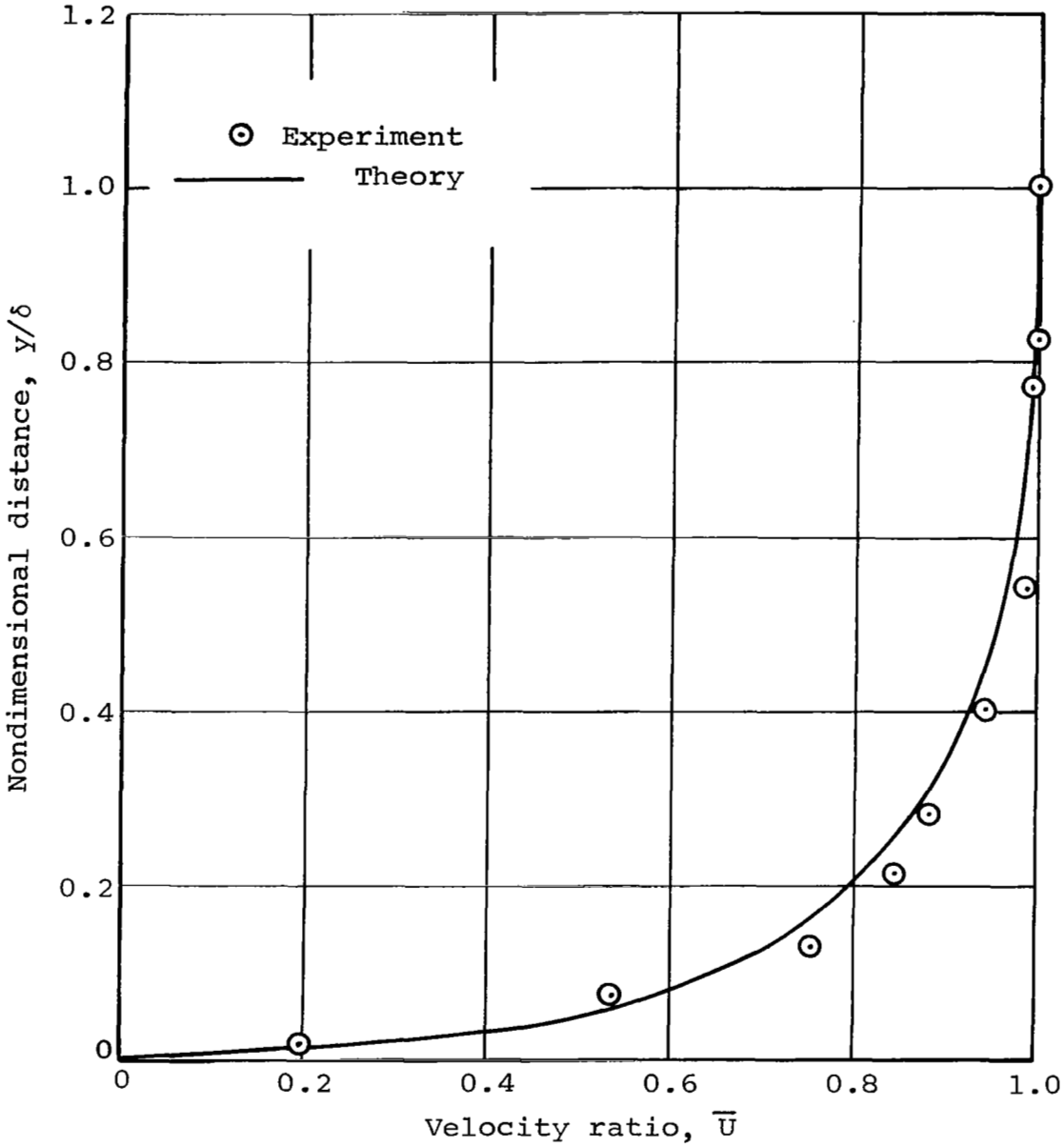

Figure 21.- Comparison between predicted and measured velocity profiles at x = 2.17 feet for compression surface tested at M_∞ = 7.4.

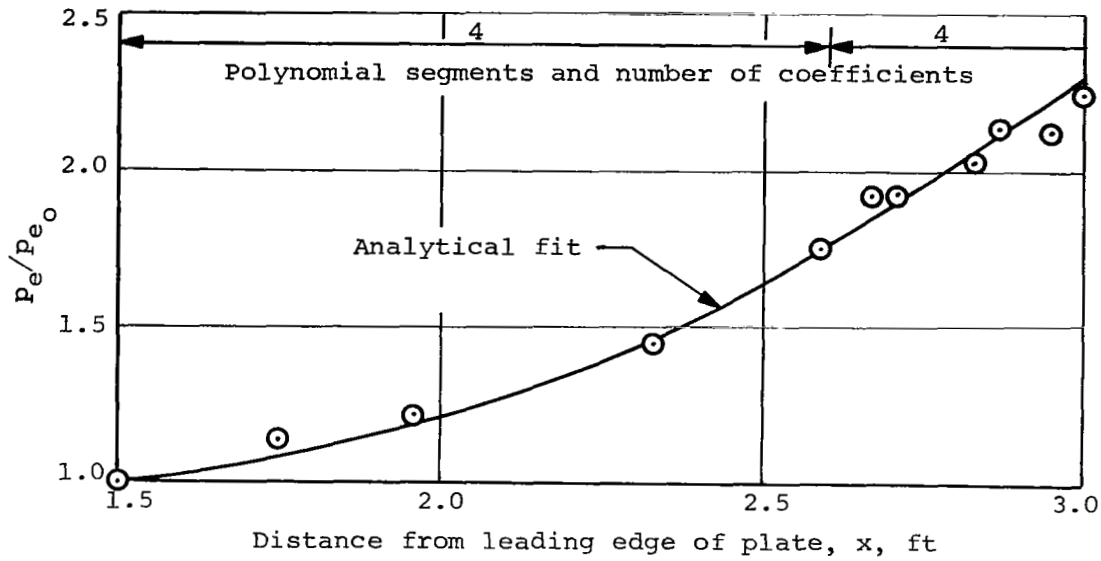

(a) Pressure distribution.

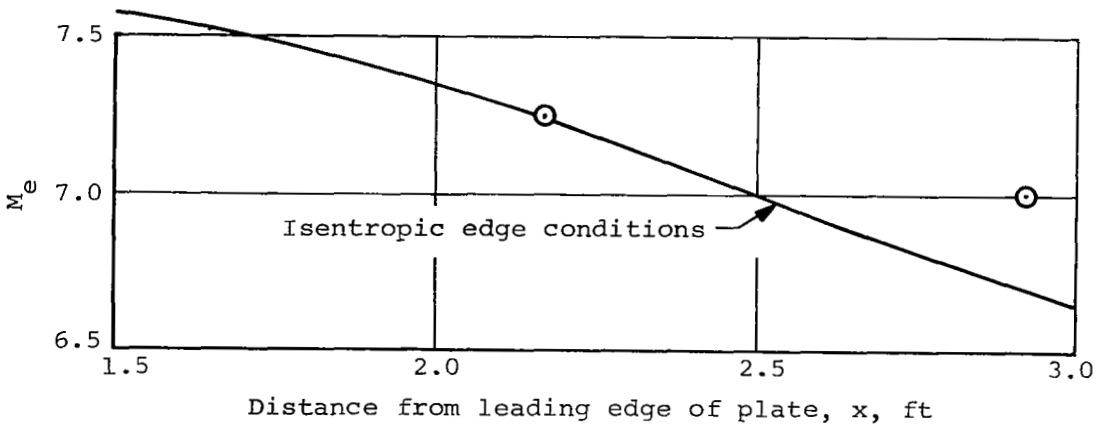

(b) Edge Mach number.

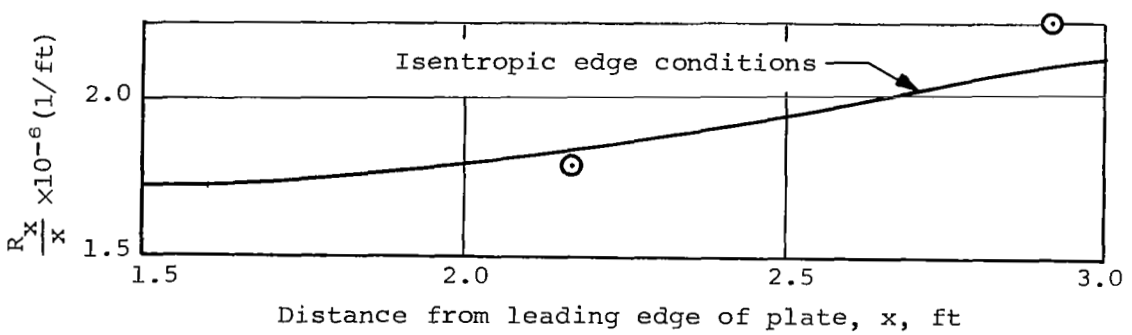

(c) Edge Reynolds number per foot.

Figure 22.- Comparison of boundary-layer edge conditions with experimental conditions for $M_\infty = 10.4$.

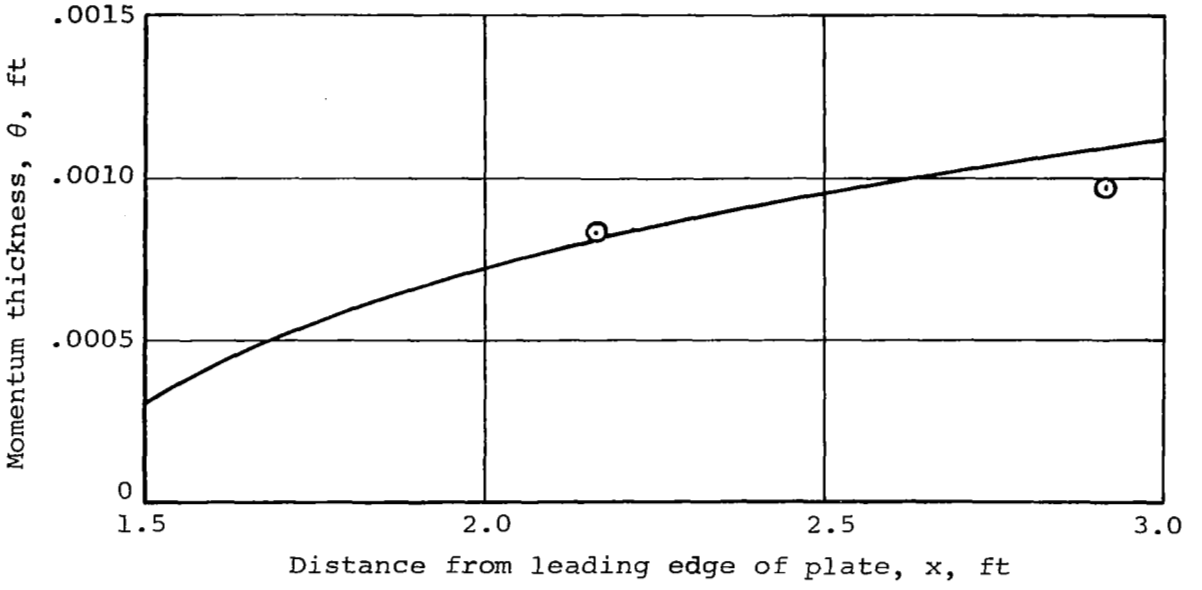

(a) Momentum thickness.

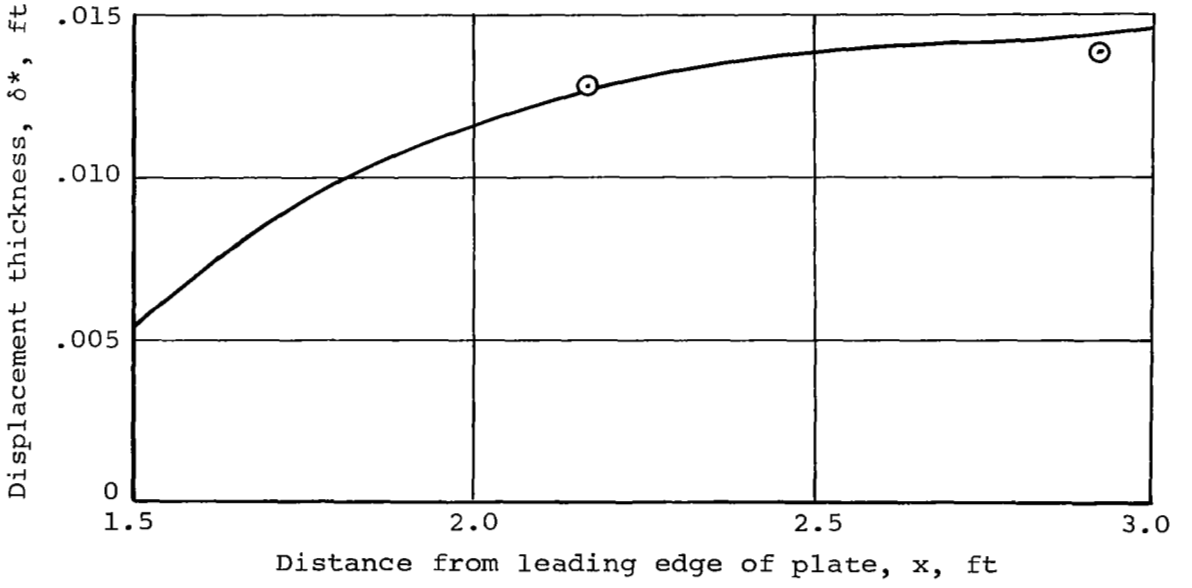

(b) Displacement thickness.

Figure 23.- Comparison of predicted and measured displacement and momentum thicknesses for compression surface tested at $M_\infty = 10.4$.

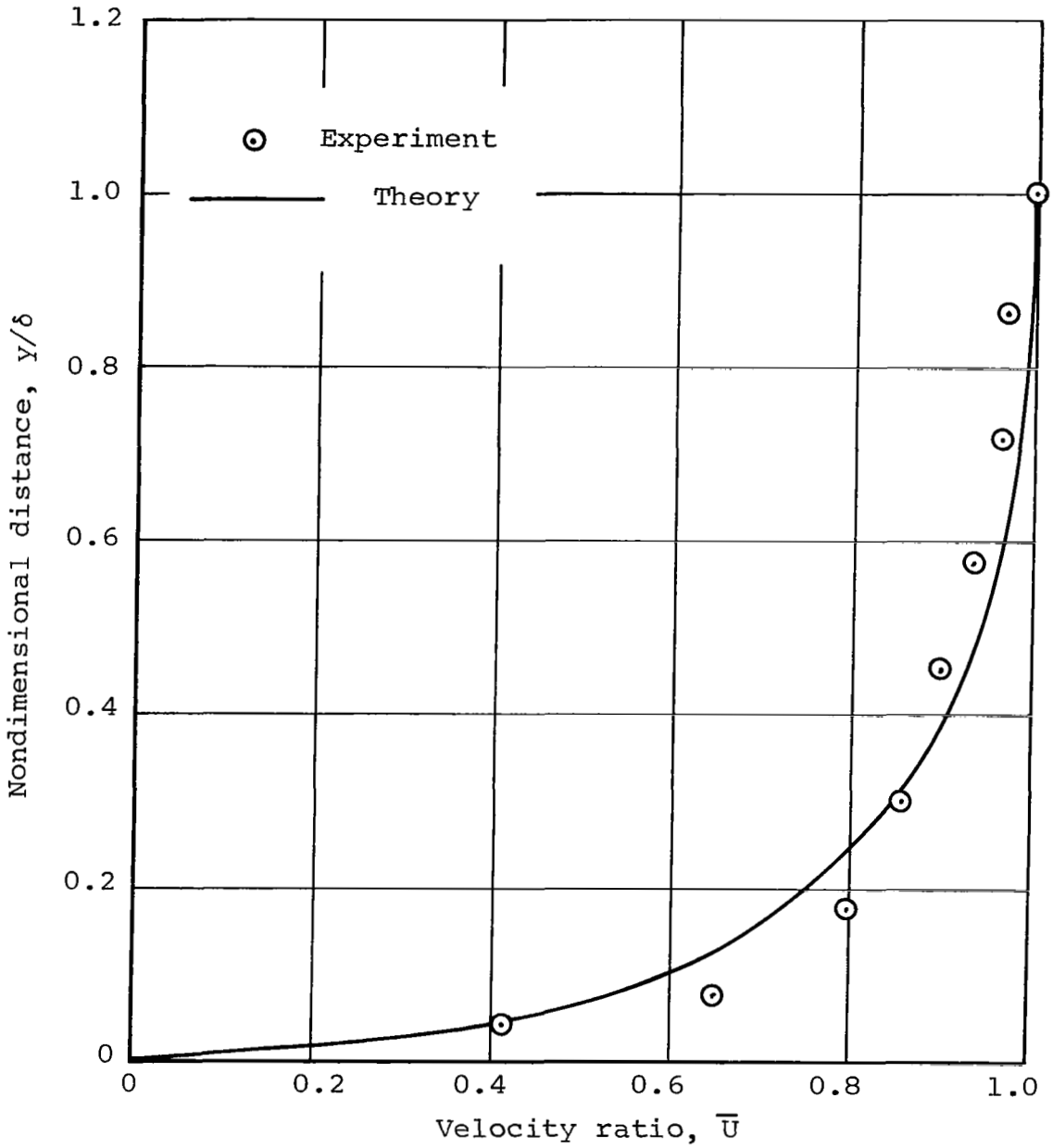

Figure 24.- Comparison between predicted and measured velocity profiles at x = 2.17 feet for compression surface tested at M_∞ = 10.4.

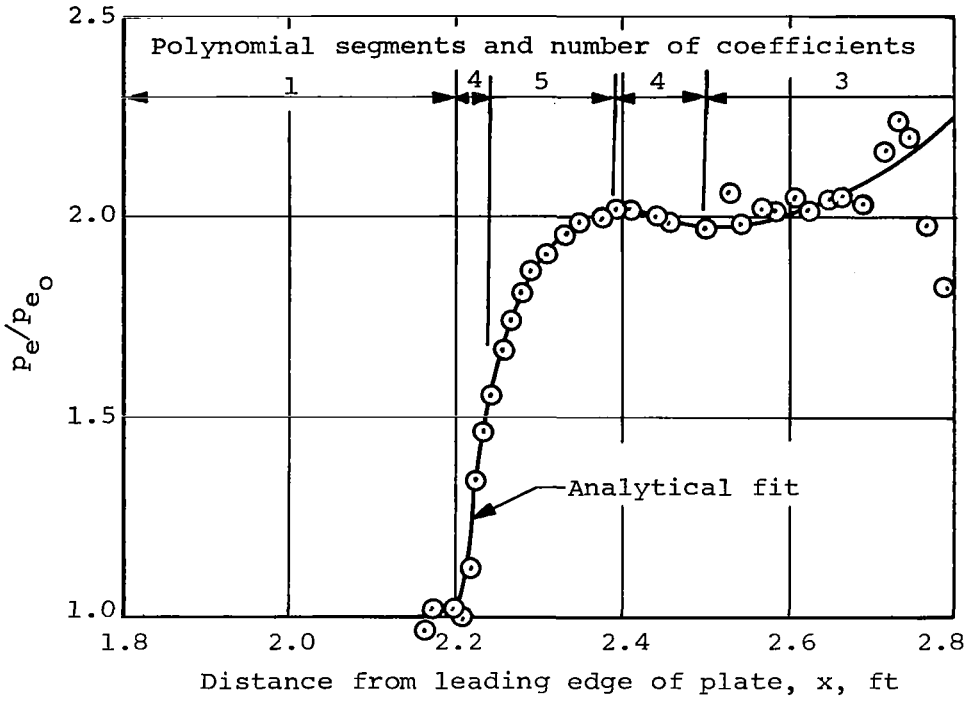

(a) Pressure distribution.

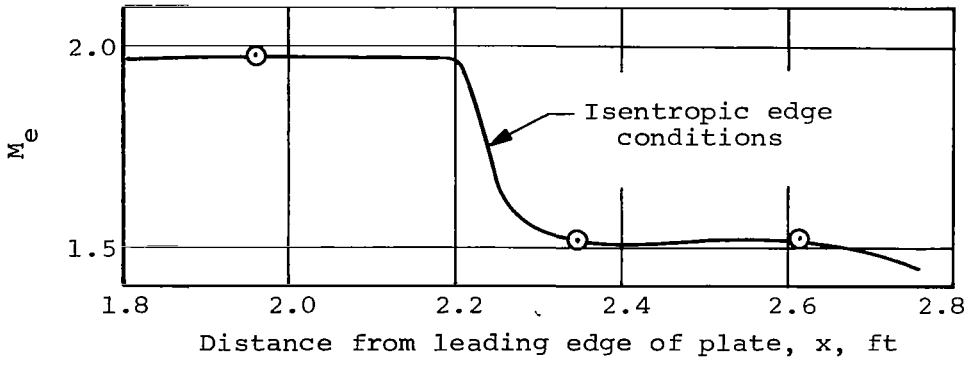

(b) Edge Mach number distribution.

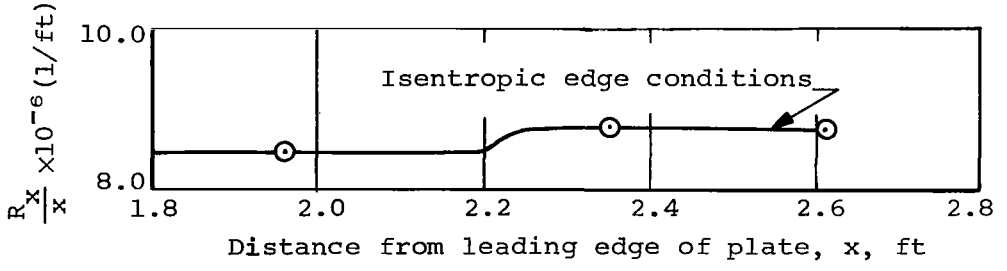

(c) Edge Reynolds number per foot.

Figure 25.- Comparison of boundary-layer edge conditions used in computer program with data of Pinckney, reference 27.

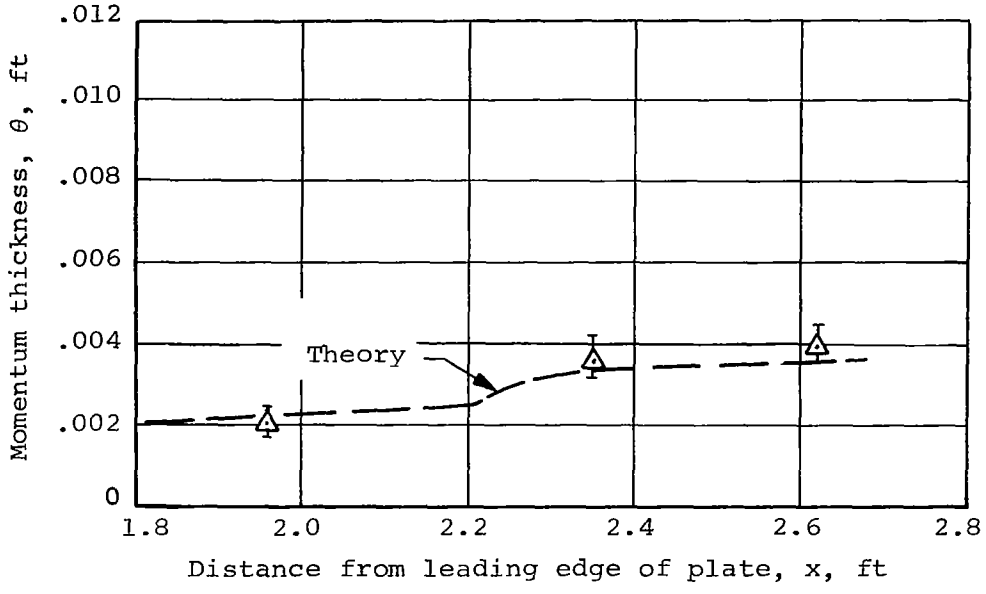

(a) Momentum thickness.

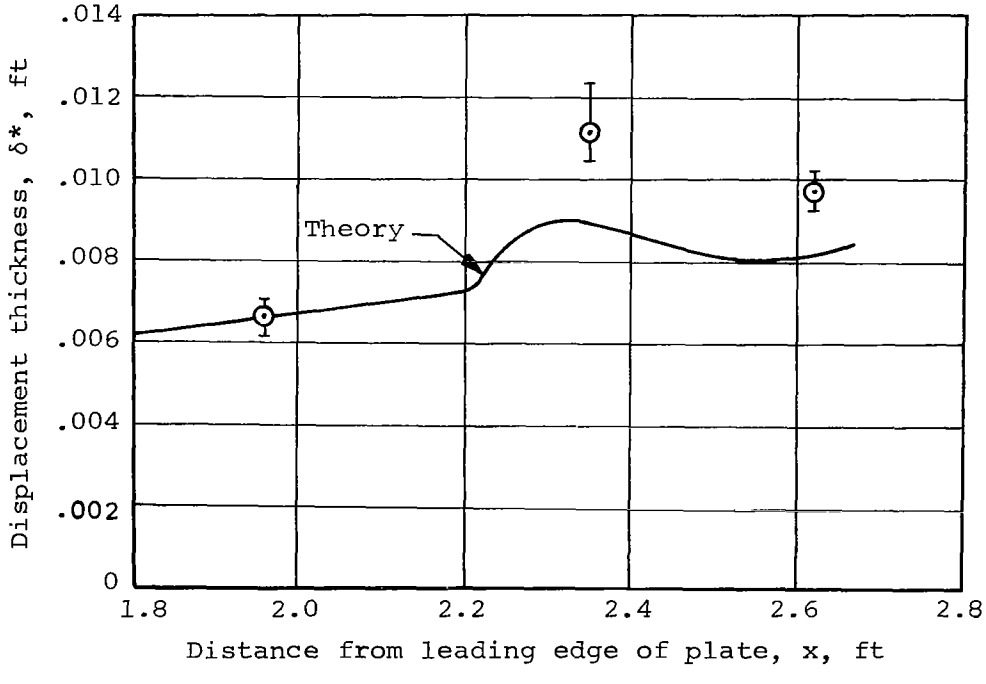

(b) Displacement thickness.

Figure 26.- Comparison of predicted displacement and momentum thicknesses with those from data of Pinckney, reference 27.

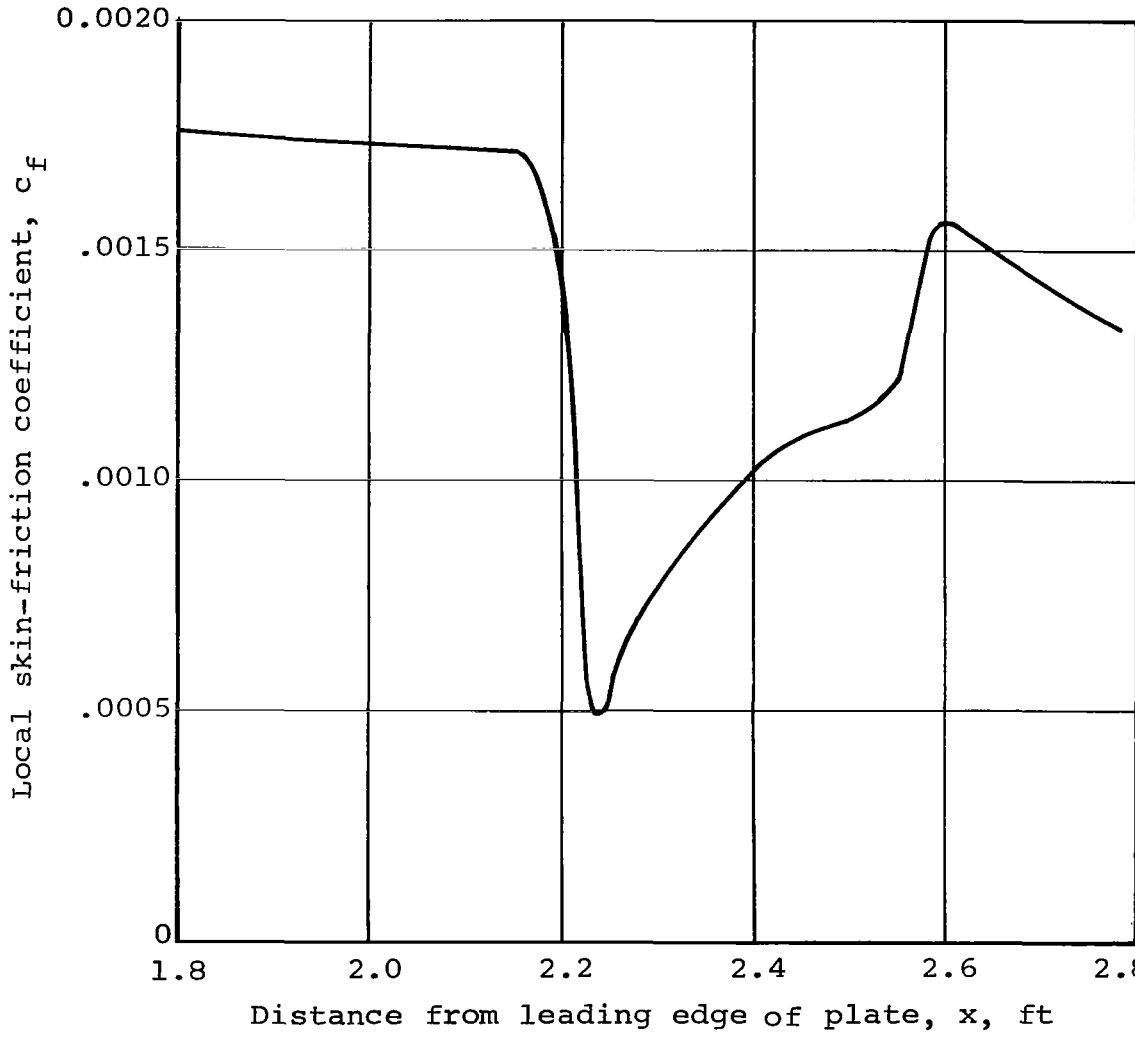

Figure 27.- Predicted skin-friction coefficient variation for the case of Pinckney, reference 27.

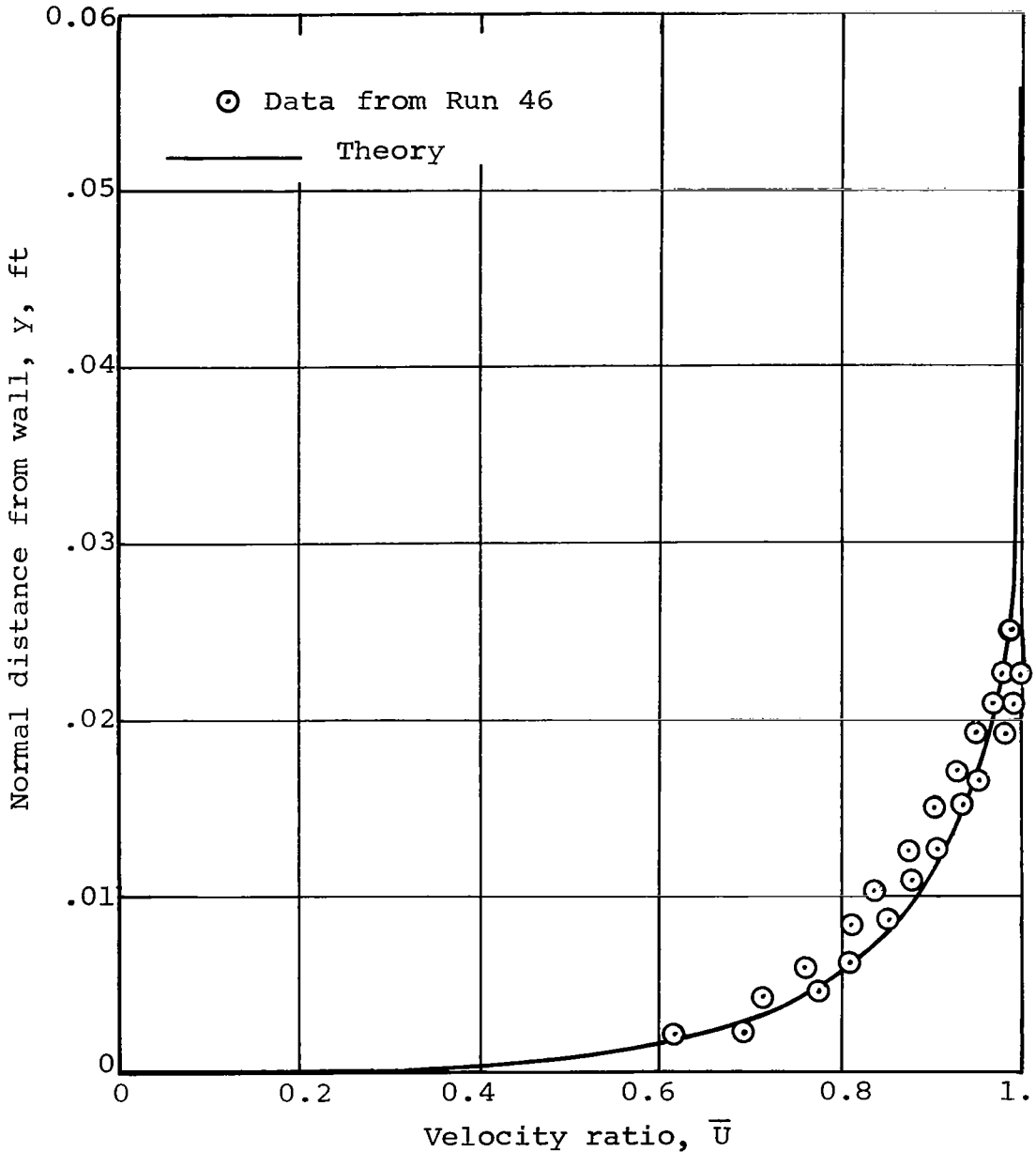

(a) x = 1.958 feet.

Figure 28.- Comparison of predicted velocity profiles with those from the data of Pinckney, reference 27.

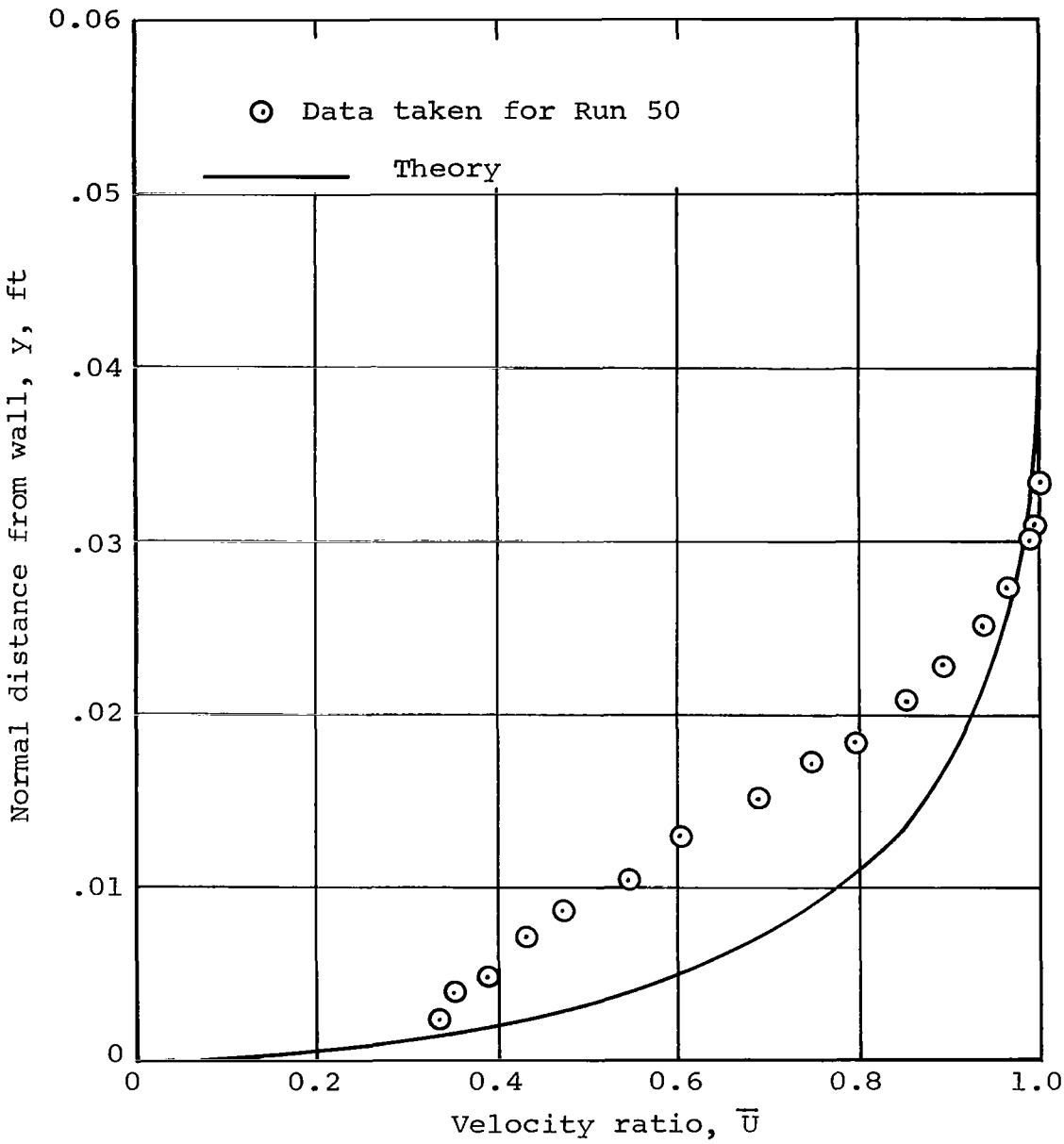

(b) x = 2.350 feet.

Figure 28.- Continued.

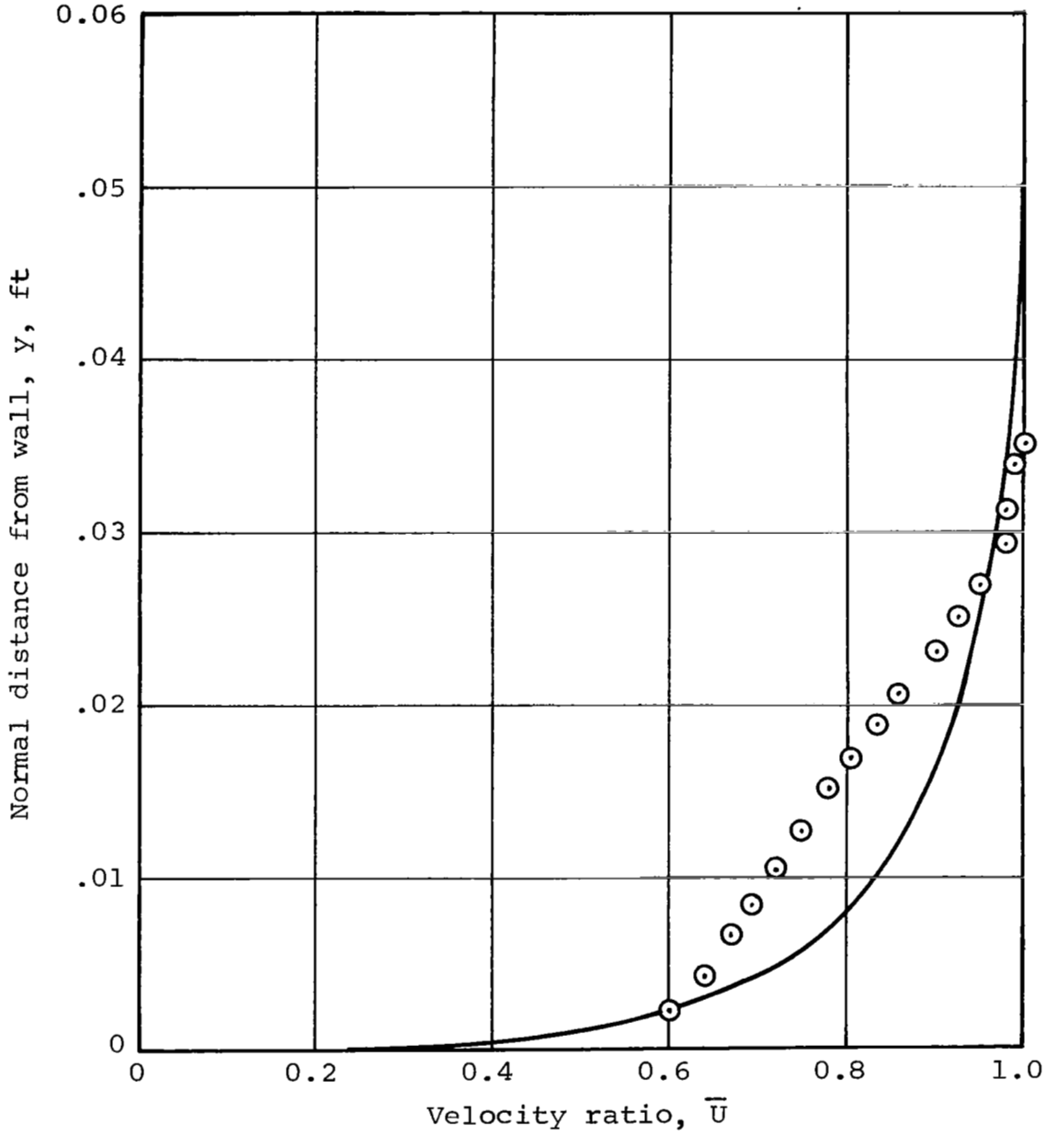

(c) x = 2.625 feet.

Figure 28.- Concluded.

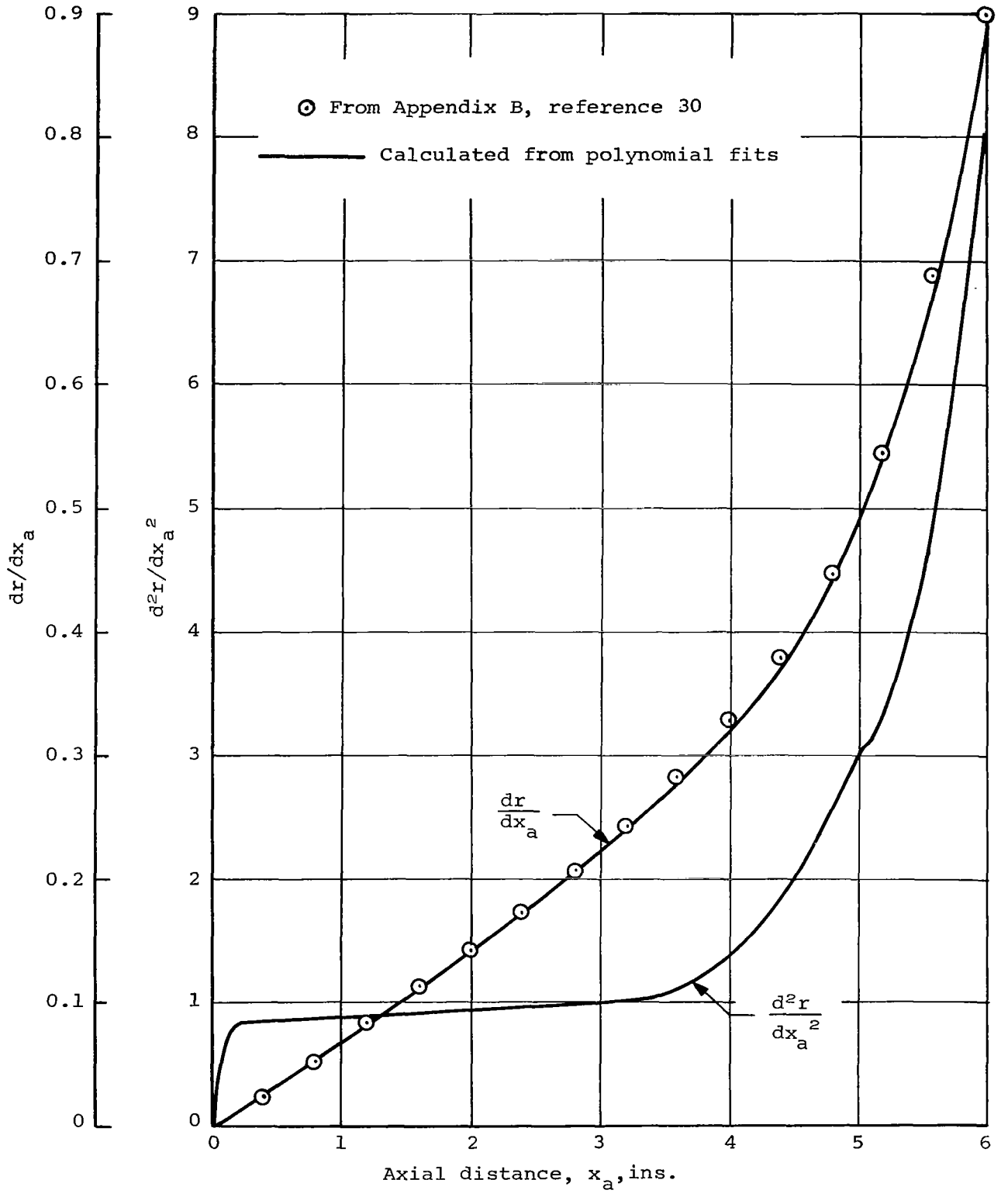

Figure 29.- Slope and second derivative of compression surface from reference 30.

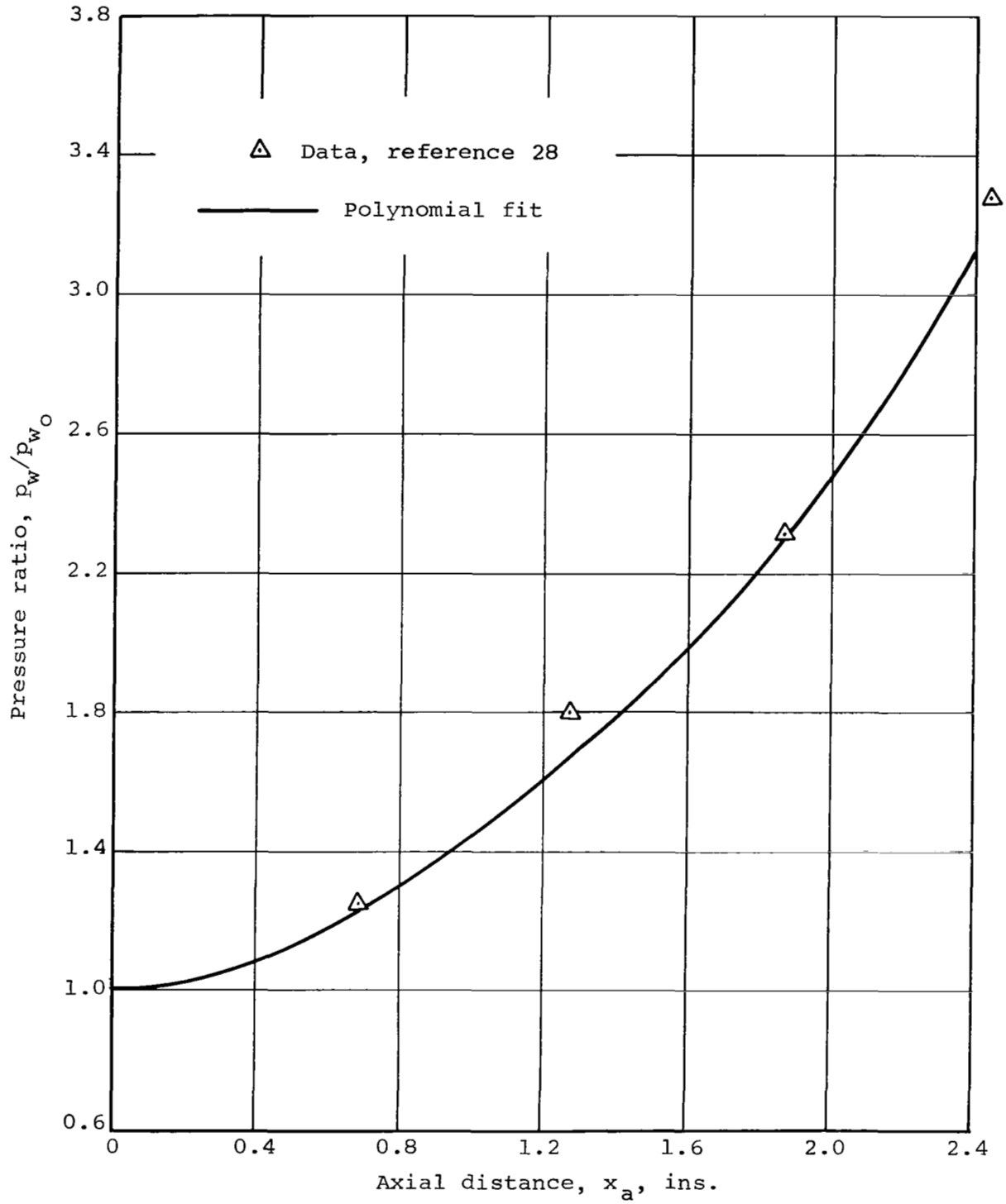

(a) Low pressure range.

Figure 30.- Polynomial fit to static pressure distribution acting on flare surface.

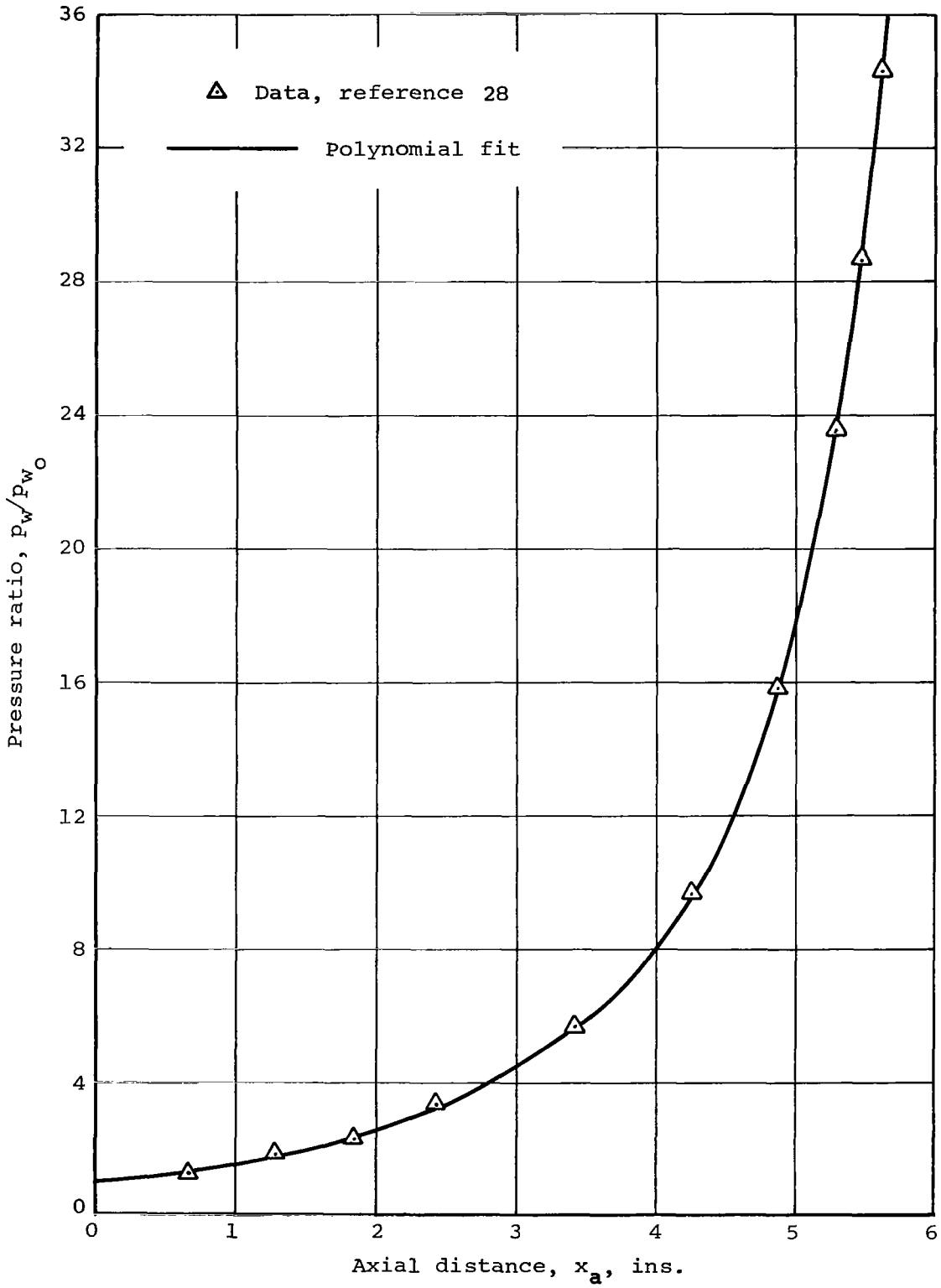

(b) High pressure range.

Figure 30.- Concluded.

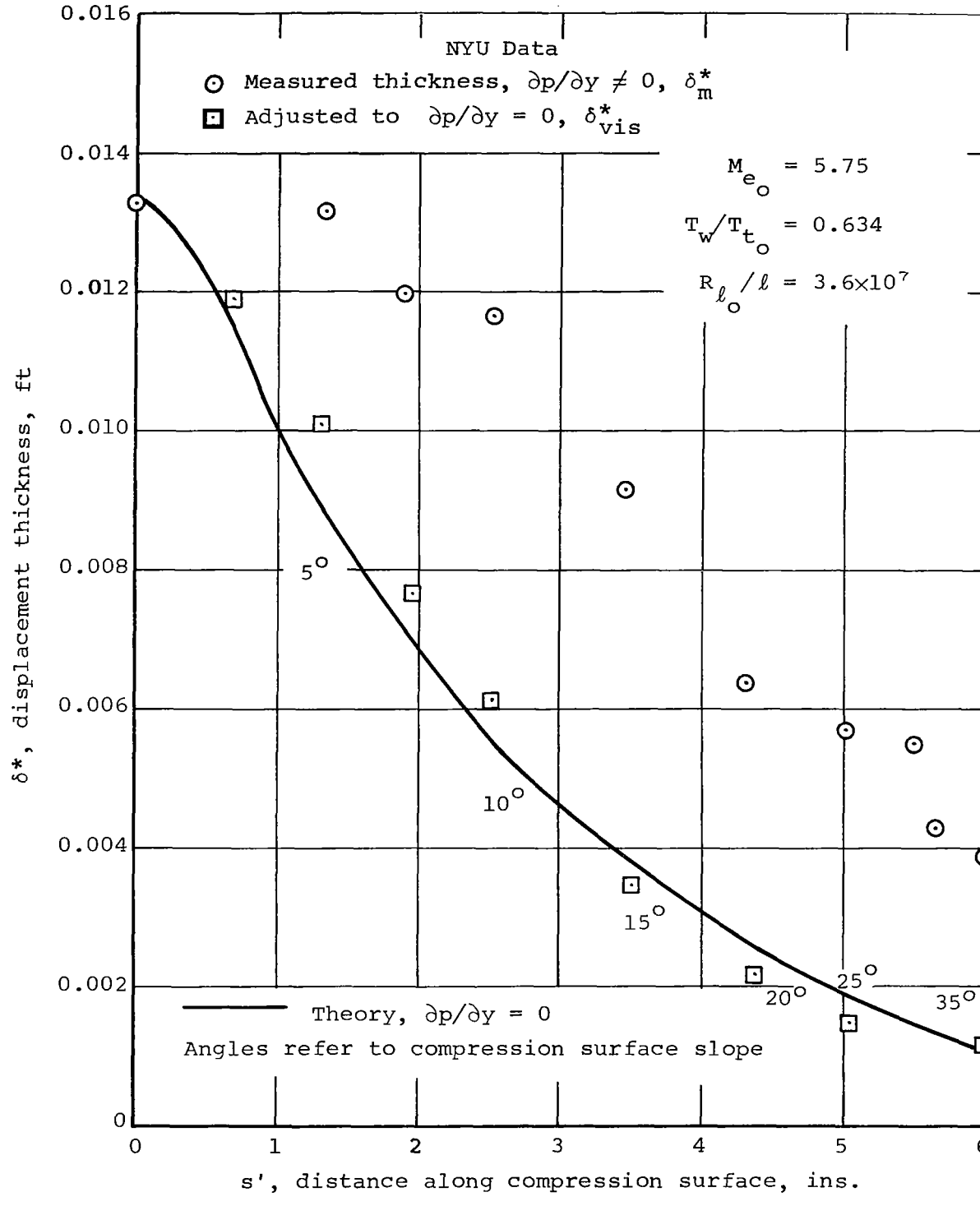

(a) Displacement thickness.

Figure 31.- Comparison between theory and NYU data for turbulent boundary layer on axisymmetric compression surface.

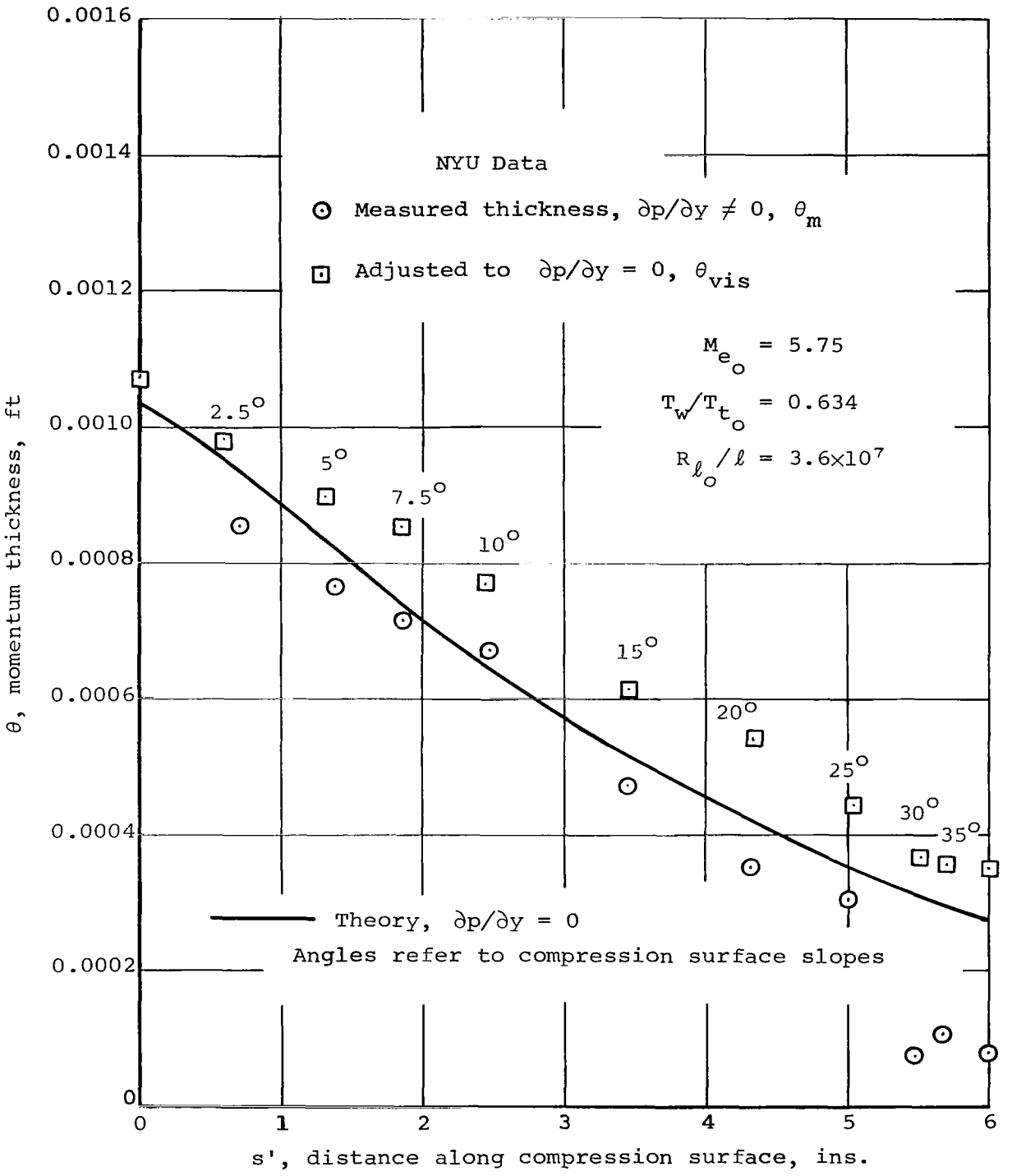

(b) Momentum thickness.

Figure 31.- Concluded.

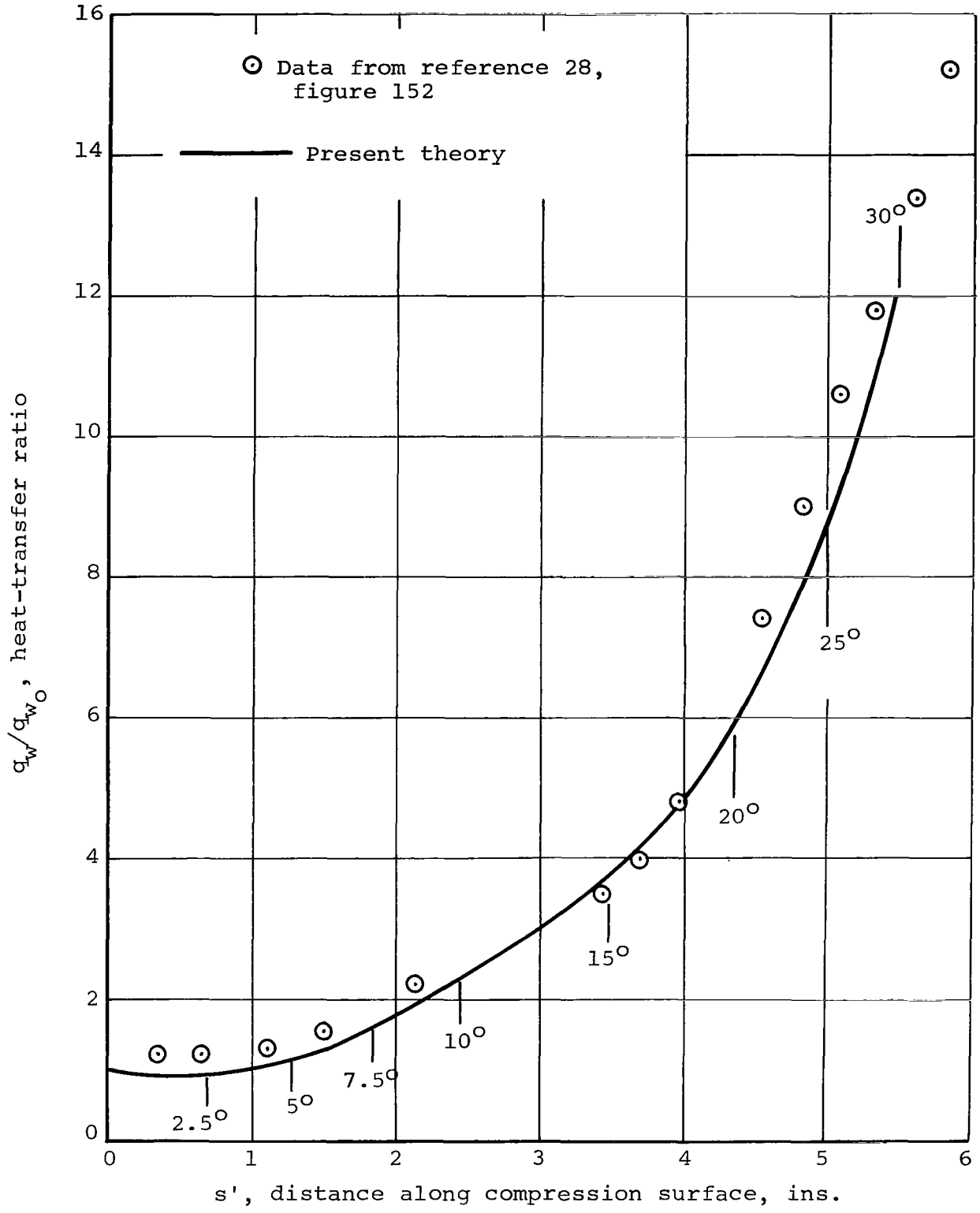

Figure 32.- Comparison of experimental and theoretical ratios of heat-transfer rate for configuration of reference 28.

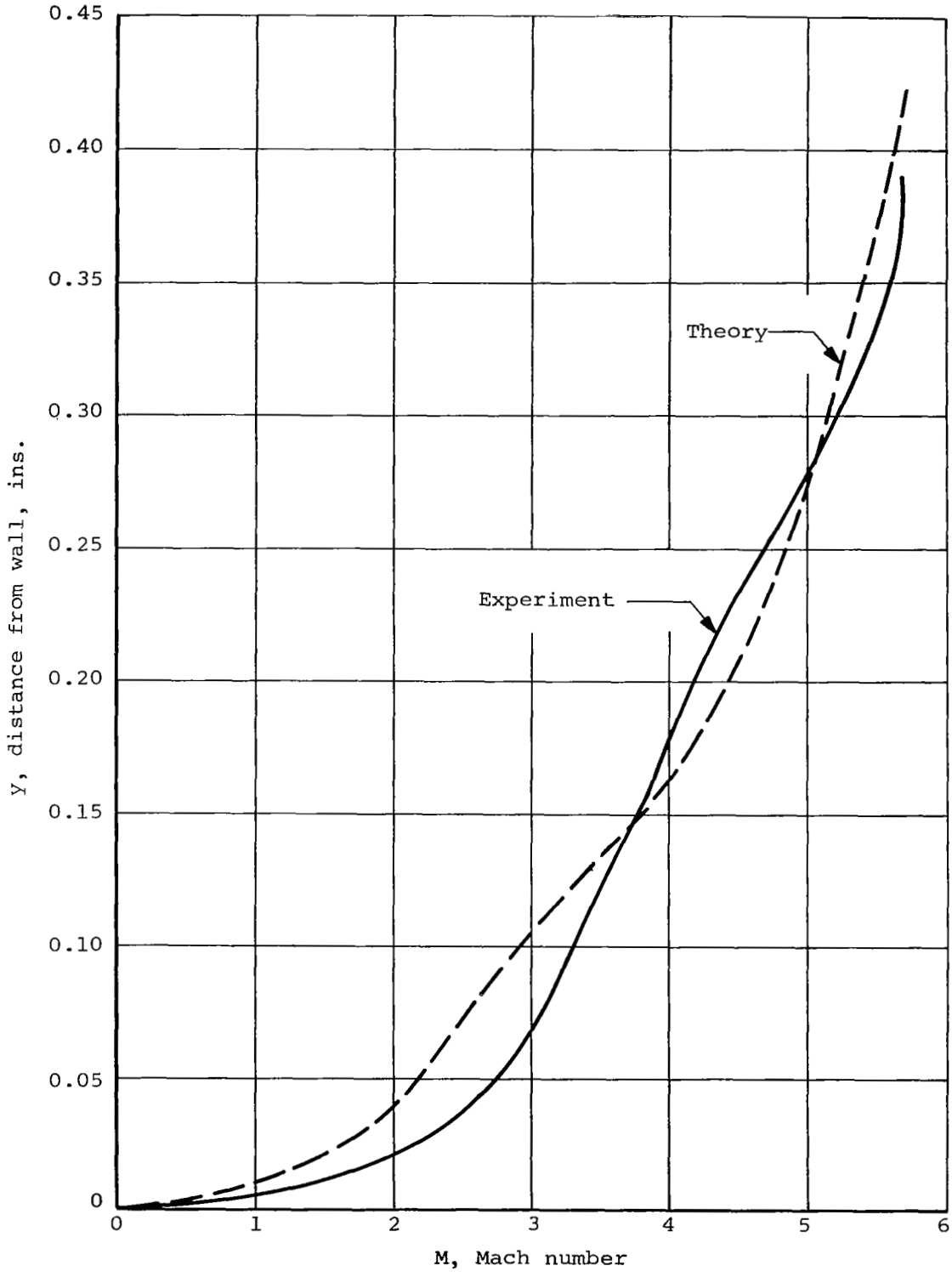

(a) $\phi = 0^{\circ}$.

Figure 33.- Mach number profiles; comparison between theory and experiment for configuration of reference 28.

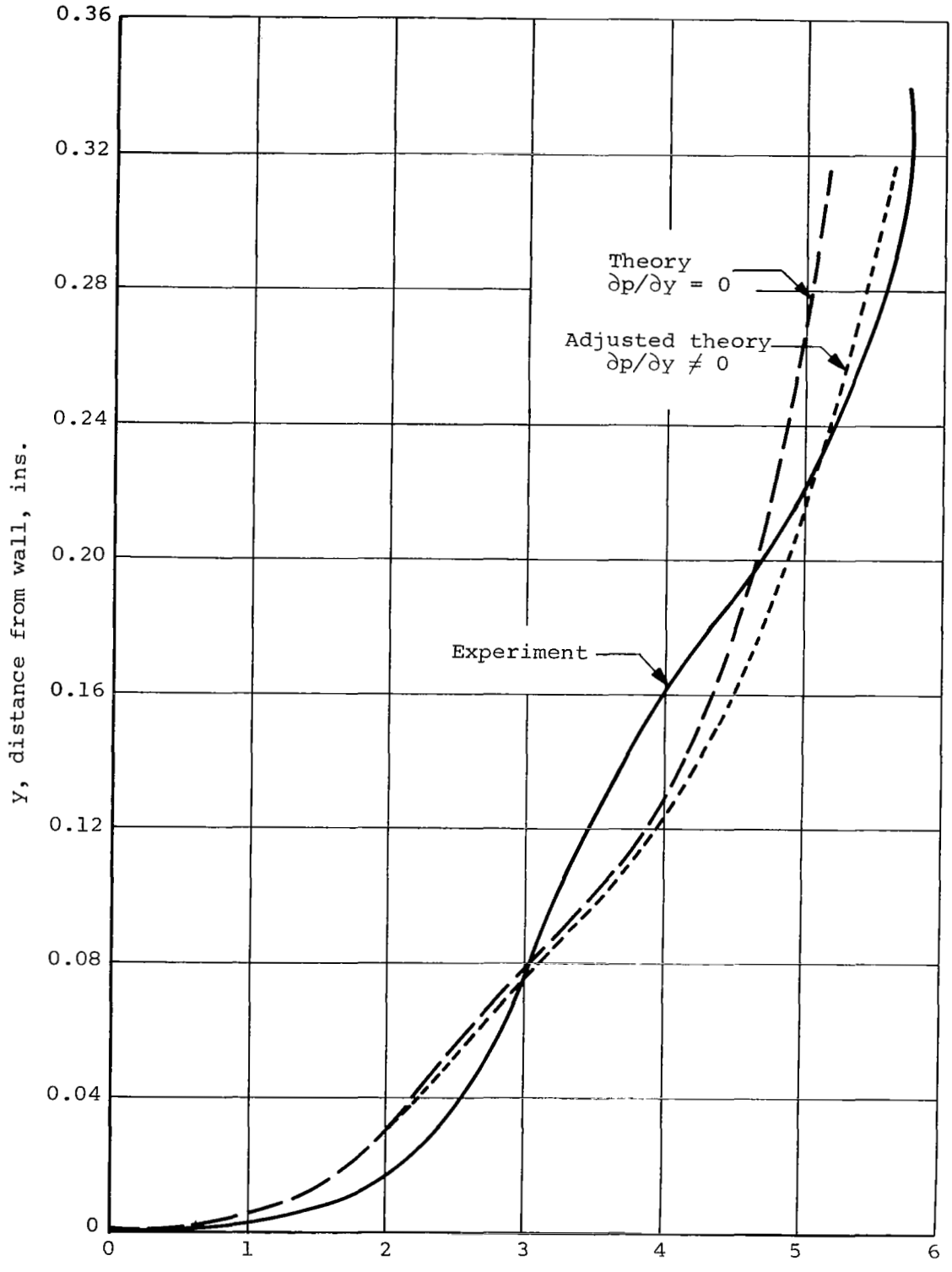

(b) $\phi = 5^{o}$.

Figure 33.- Continued.

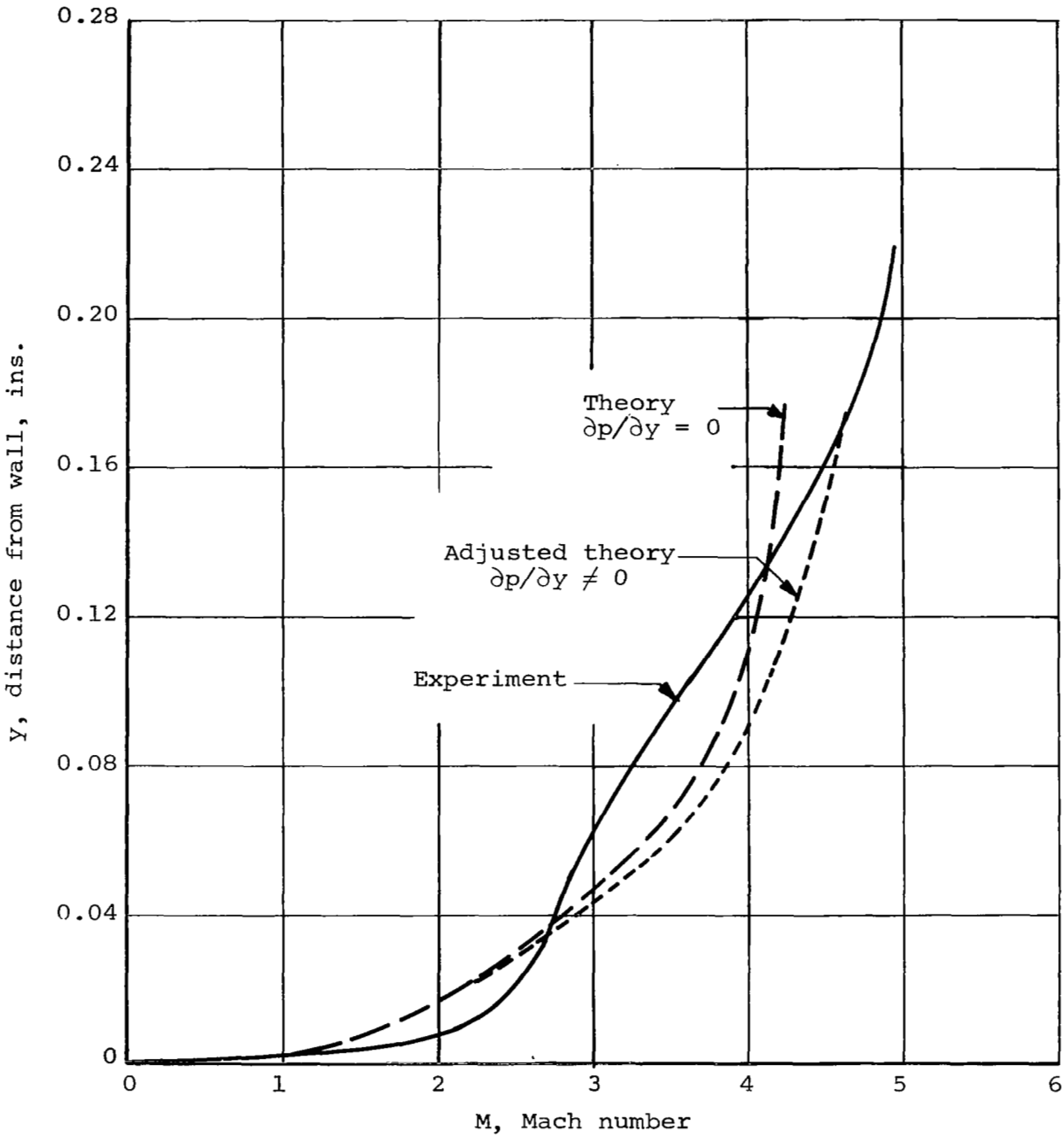

(c) $\phi = 15^{o}$.

Figure 33.- Continued.

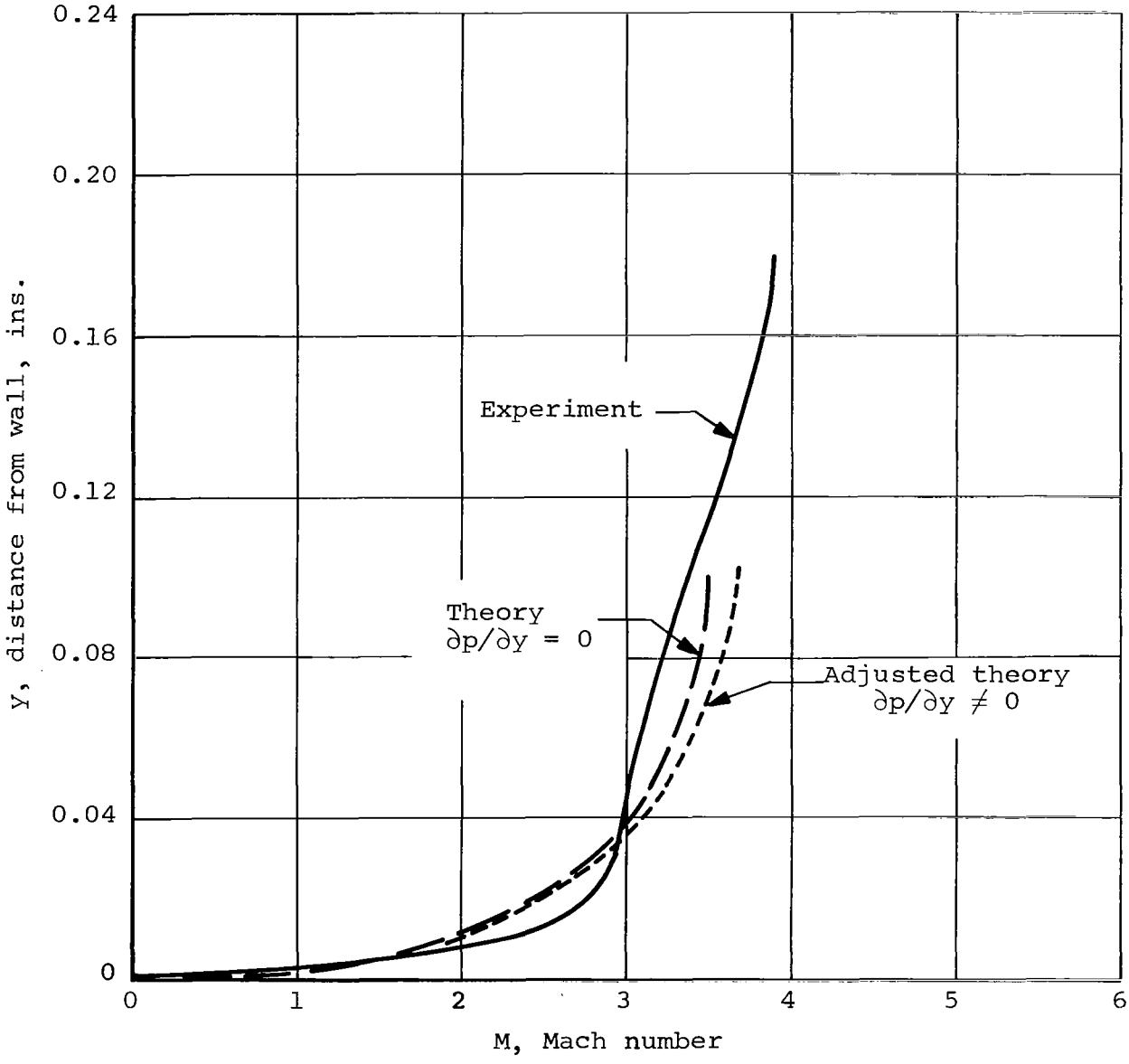

(d) $\phi = 25^{\circ}$.

Figure 33.- Concluded.

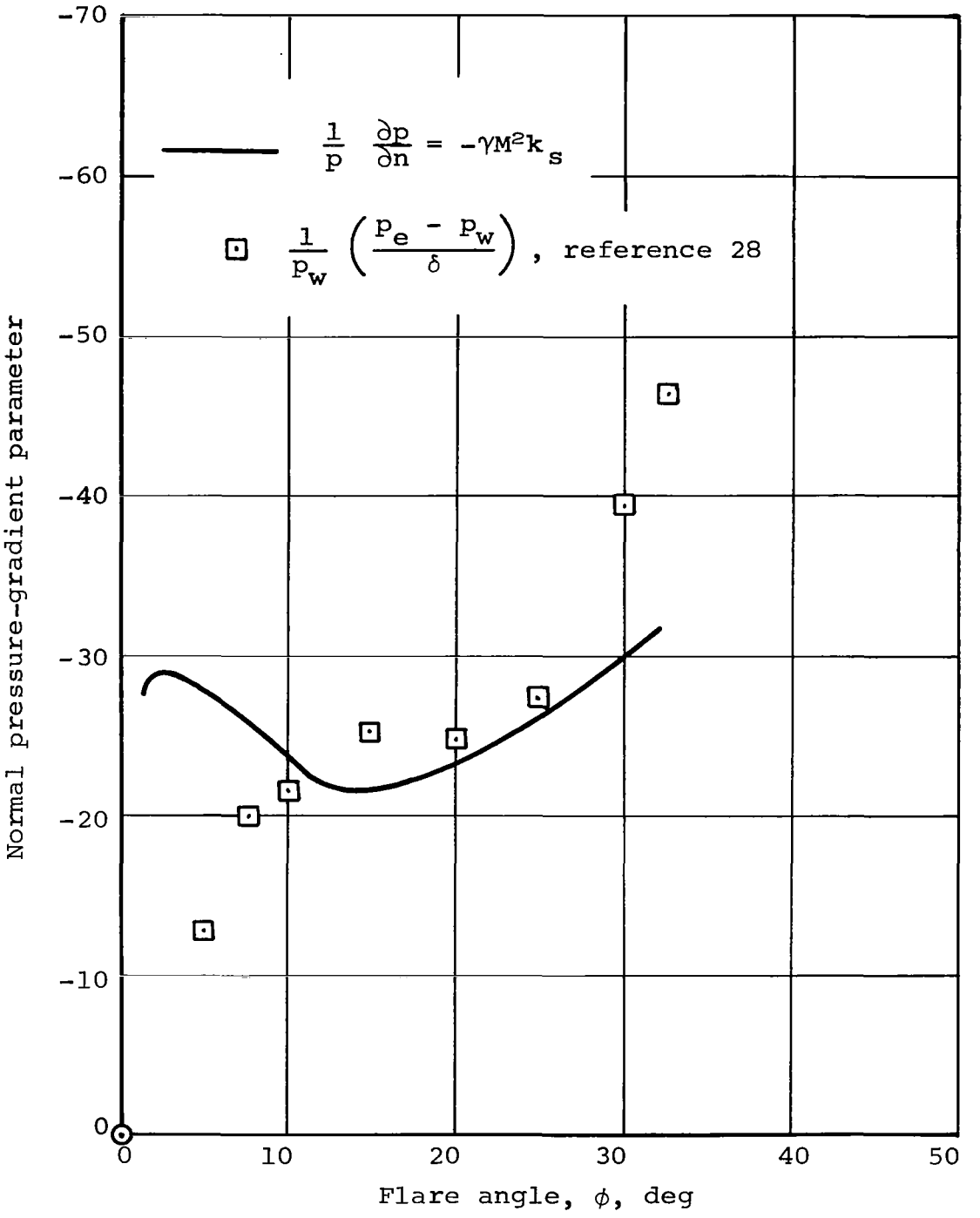

Figure 34.- Comparison of predicted and experimental normal pressure-gradient parameters for configuration of reference 28.

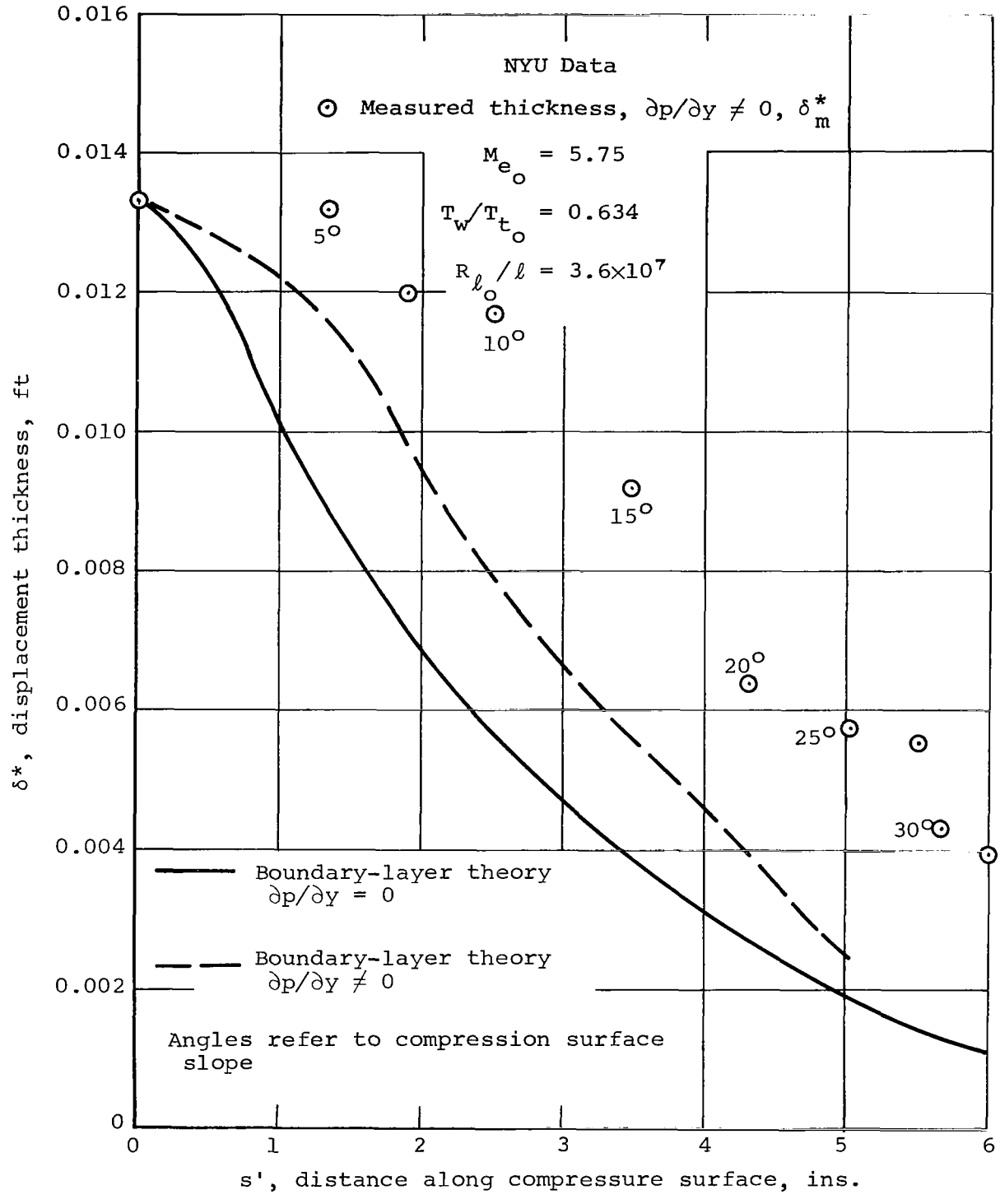

(a) Displacement thickness.

Figure 35.- Comparison between experiment and theory including effect of normal pressure gradient in theory; configuration of reference 28.

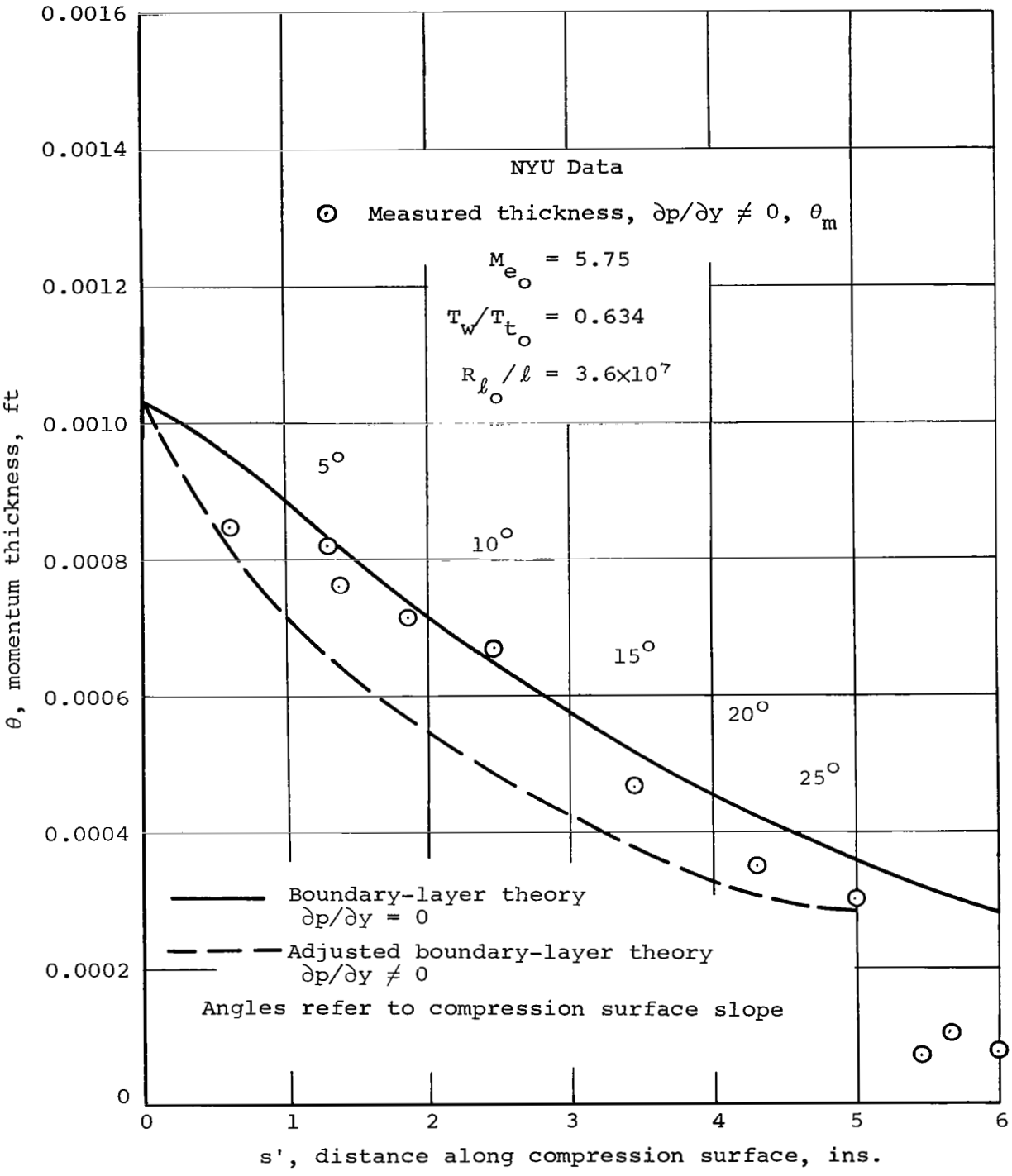

(b) Momentum thickness.

Figure 35.- Concluded.

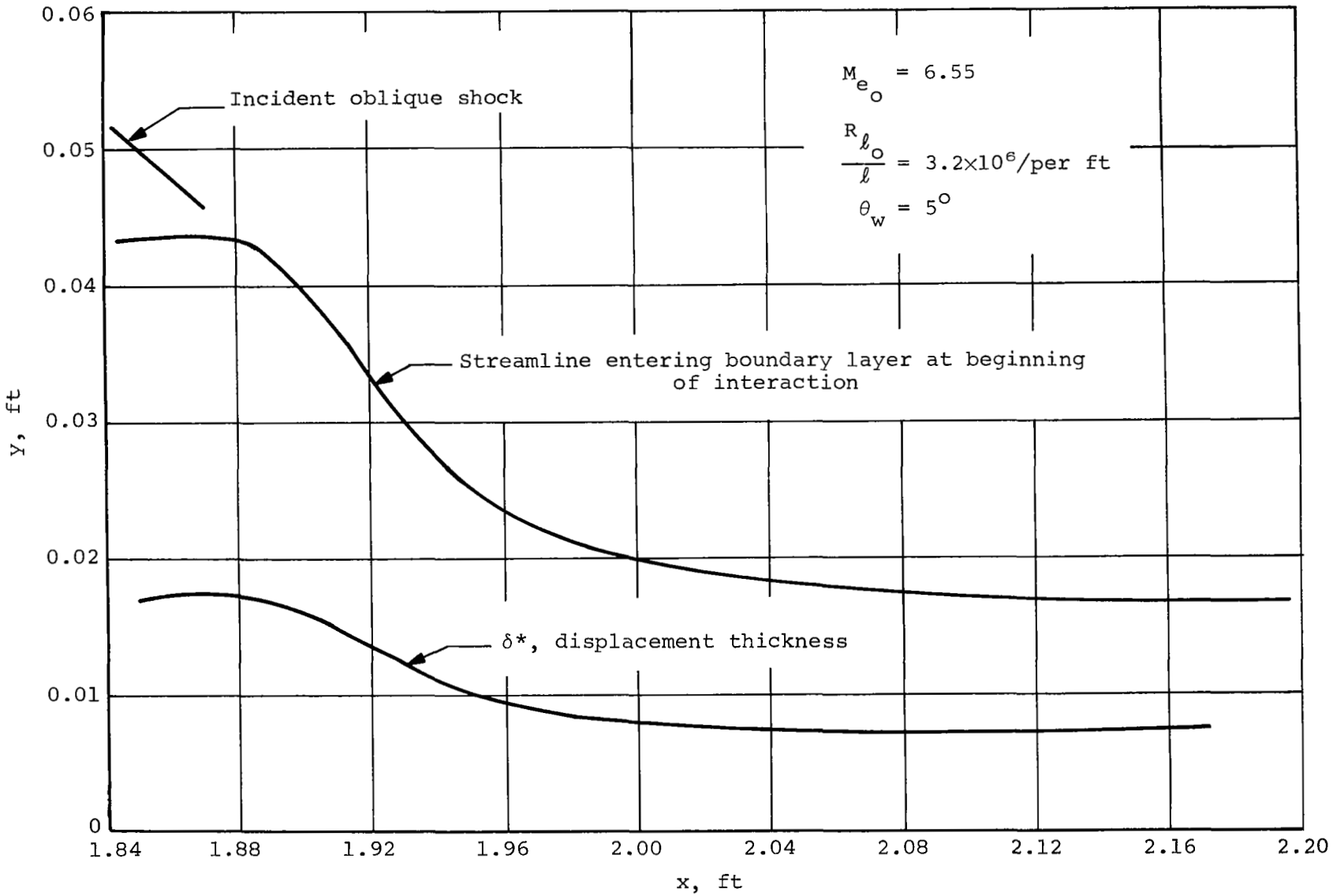

Figure 36.- Calculated streamline and δ^* line associated with interaction between oblique shock and flat-plate turbulent boundary layer.

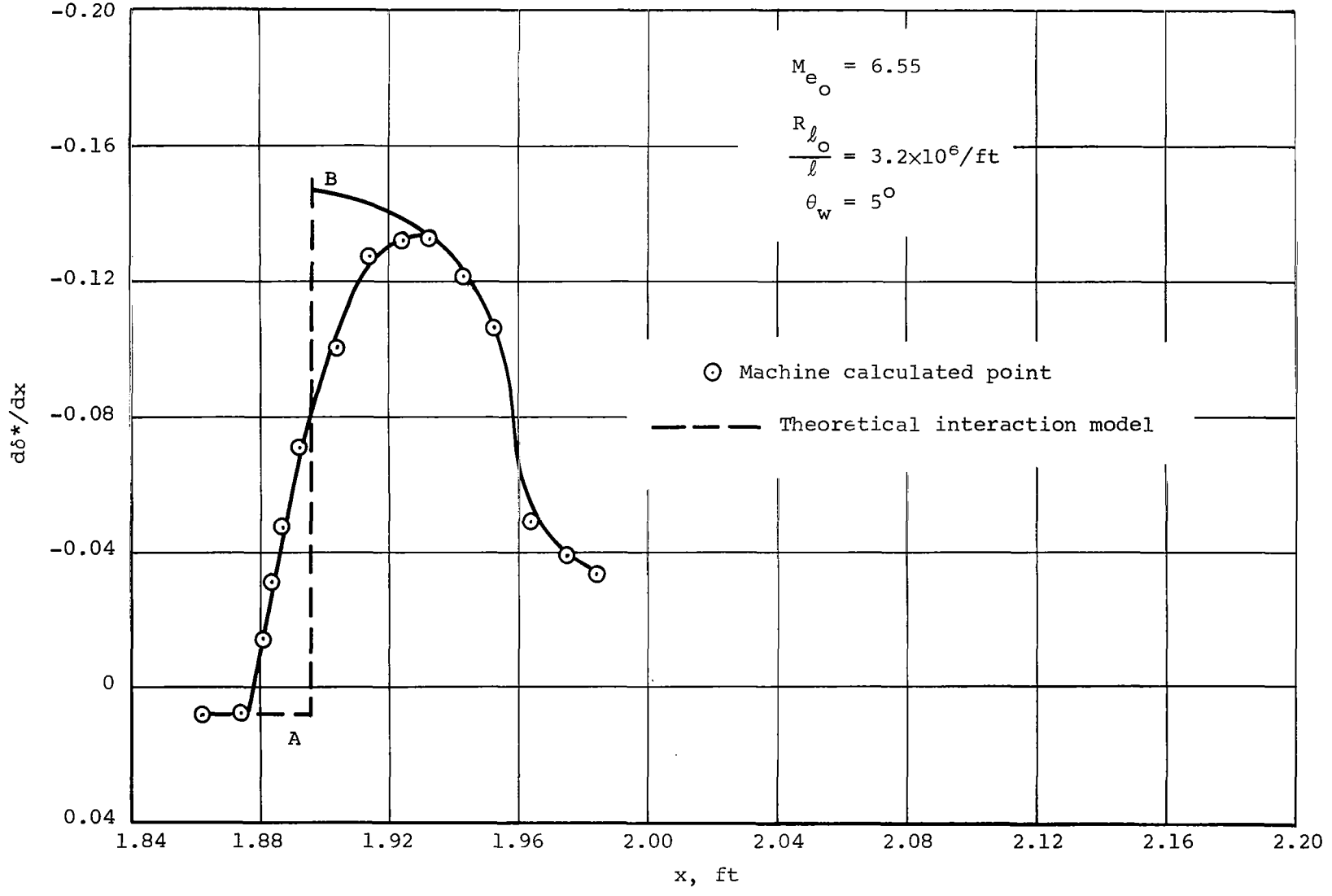

Figure 37.- Calculated slopes of the δ^* line associated with interaction between oblique shock and flat-plate turbulent boundary layer.

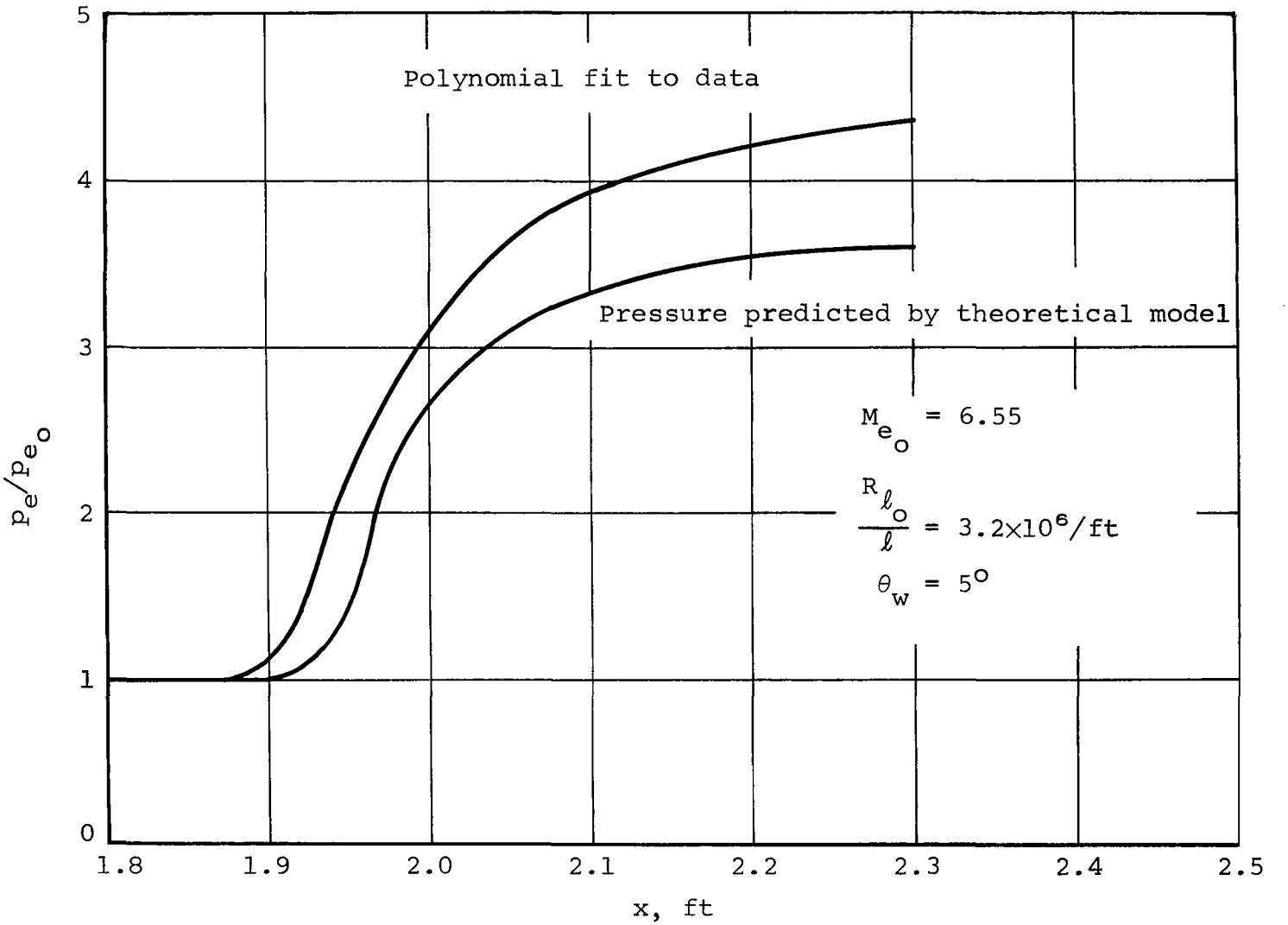

Figure 38.- Comparison of fitted experimental pressure distribution and that calculated by theoretical interaction model.